

# **Mechanismen der synaptischen Übertragung an der zerebellären Moosfaser-Körnerzell-Synapse**

Von der Medizinischen Fakultät  
der Universität Leipzig  
genehmigte

HABILITATIONSSCHRIFT

zur Erlangung des akademischen Grades

Doctor medicinae habilitatus

(Dr. med. habil.)

vorgelegt

von Dr. med. Igor Delvendahl

geboren am 06.12.1984 in Freiburg im Breisgau

Tag der Verleihung: 24.01.2017

## **Bibliographische Beschreibung**

Delvendahl, Igor: *Mechanismen der synaptischen Übertragung an der zerebellären Moosfaser-Körnerzell-Synapse*

Universität Leipzig, kumulative Habilitationsschrift

78 Seiten, inklusive 4 Originalarbeiten, 5 Abbildungen und Literaturstellen

Die Funktion unseres Zentralnervensystems beruht auf der zeitlich präzisen Übertragung elektrischer Signale zwischen Neuronen. Diese synaptische Übertragung findet in weniger als einer tausendstel Sekunde statt. Eine schnelle und hochfrequente Signalübertragung erweitert die Kodierungskapazität und beschleunigt die Verarbeitung von Informationen. Obwohl viele der an synaptischer Übertragung beteiligten Prozesse und Proteine bekannt sind, ist das Verständnis der Mechanismen, die für eine schnelle und hochfrequente Signalübertragung verantwortlich sind, bisher unvollständig.

Um die Mechanismen hochfrequenter synaptischer Übertragung zu untersuchen, wurden in dieser Arbeit prä- und postsynaptische Patch-Clamp Ableitungen an der zerebellären Moosfaser-Körnerzell-Synapse in akuten Hirnschnitten der Maus eingesetzt. Es zeigte sich, dass diese Synapse präsynaptische Aktionspotenziale mit einer Frequenz über einem Kilohertz feuern kann und dass Informationen in diesem Frequenzbereich an die postsynaptische Zelle übertragen werden können. Hierbei vermitteln besonders schnelle Natrium- und Kalium-Kanäle eine extrem kurze Dauer der Aktionspotenziale, die dennoch metabolisch relativ effizient sind. Schnelle Kalzium-Kanäle und eine schwache präsynaptische Kalzium-Pufferung ermöglichen eine synchrone Vesikelfreisetzung mit hohen Frequenzen. Zusätzlich greift die Präsynapse auf einen großen Vorrat an freisetzbaren Vesikeln zurück, dessen Auffüllung besonders schnell stattfindet.

Aufgrund der hochfrequenten synaptischen Übertragung ist die Moosfaser-Körnerzell-Synapse ideal, um zu untersuchen, wie schnell die auf eine Vesikelfreisetzung folgende Endozytose vonstatten geht. Mit optimierten, hochauflösenden Kapazitätsmessungen konnte an der Moosfaser-Körnerzell-Synapse eine sehr schnelle Endozytose nach einzelnen Aktionspotenzialen gezeigt werden. Die hohe Geschwindigkeit der Endozytose unterstützt somit eine hochfrequente synaptische Übertragung. Diese schnelle Endozytose wird durch die Moleküle Dynamin und Actin vermittelt und ist unabhängig von einer Wirkung von Clathrin. Stärkere Stimuli wie längere Depolarisationen evozieren eine langsamere Form der Endozytose, die zusätzlich Clathrin-abhängig ist.

Durch die mechanistische Beschreibung hochfrequenter Signalübertragung an einer zentralen Synapse erweitern die Ergebnisse der vorliegenden Arbeit unser Verständnis von synaptischer Übertragung und Informationsverarbeitung im Zentralnervensystem.

# Inhaltsverzeichnis

<b>1</b>	<b>EINFÜHRUNG IN DIE THEMATIK</b>	<b>4</b>
1.1	Synaptische Übertragung	4
1.2	Die Rolle hochfrequenter Übertragung im Zentralnervensystem	6
1.3	Die zerebelläre Moosfaser-Körnerzell-Synapse	8
<b>2</b>	<b>ZIELSETZUNG</b>	<b>11</b>
<b>3</b>	<b>ORIGINALARBEITEN</b>	<b>13</b>
3.1	Ritzau-Jost*, Delvendahl* et al. 2014 Neuron 84, 152–163.	13
3.2	Delvendahl et al. 2015 Proc. Natl. Acad. Sci. USA 112, E3075–3084.	26
3.3	Delvendahl et al. 2015 Front. Cell. Neurosci. 9, 93.	37
3.4	Delvendahl et al. 2016 Neuron 90, 492–498.	46
<b>4</b>	<b>DISKUSSION UND AUSBLICK</b>	<b>54</b>
4.1	Die Mechanismen hochfrequenter synaptischer Übertragung	54
4.2	Bedeutung hochfrequenter Signalübertragung für neuronale Signalverarbeitung	59
4.3	Übertragbarkeit auf andere Synapsen	61
4.4	Zusammenfassung und Ausblick	64
<b>5</b>	<b>LITERATURVERZEICHNIS</b>	<b>67</b>
<b>6</b>	<b>ERKLÄRUNG</b>	<b>74</b>
<b>7</b>	<b>LEBENS LAUF</b>	<b>75</b>

# 1 Einführung in die Thematik

## 1.1 Synaptische Übertragung

Die Funktion des Zentralnervensystems beruht auf einer zeitlich präzisen Übertragung elektrischer Signale zwischen Neuronen. Diese Signalübertragung findet an spezialisierten Kontaktstellen, den Synapsen, mittels Ausschüttung eines Überträgerstoffes (chemische Synapse) oder über direkte elektrische Kopplung der Neurone (elektrische Synapse) statt. Der chemischen Übertragung kommt im Nervensystem eine besondere Bedeutung zu, sodass die Funktionsweise chemischer Synapsen entsprechend Gegenstand umfangreicher Forschung ist.

An chemischen Synapsen kontaktiert das Axon eines Neurons ein oder mehrere weitere Neurone. Das präsynaptische Neuron bildet dabei eine spezialisierte Nervenendigung oder –aufreibung aus, die von der postsynaptischen Zellmembran nur durch einen schmalen synaptischen Spalt von etwa 20 nm Durchmesser getrennt ist. Präsynaptische Nervenendigungen enthalten eine Vielzahl an synaptischen Vesikeln, deren Inhalt Neurotransmittermoleküle wie zum Beispiel Glutamat oder GABA sind und die mittels Exozytose freigesetzt werden. Die Vesikel in der präsynaptischen Nervenendigung können bei Eintreffen eines Aktionspotenzials  $\text{Ca}^{2+}$ -abhängig an den so genannten aktiven Zonen mit der Zellmembran verschmelzen und ihren Inhalt in den synaptischen Spalt freigeben (Abbildung 1; Neher und Sakaba, 2008). Für die  $\text{Ca}^{2+}$ -abhängige, synchrone Neurotransmitterfreisetzung ist ein komplexes Zusammenspiel mehrerer Proteine notwendig (Schneppenburger und Rosenmund, 2015). Zum gegenwärtigen Zeitpunkt geht man davon aus, dass das Protein Synaptotagmin die Erhöhung der präsynaptischen  $\text{Ca}^{2+}$ -Konzentration registriert und dass daraufhin vesikuläre sowie membranständige Proteine, die zusammen den so genannten SNARE-Komplex bilden, die Fusion von Vesikelmembran und Zellmembran vermitteln (Südhof, 2004). Nach der Fusion eines präsynaptischen



Vesikels gelangen die Neurotransmittermoleküle per Diffusion zur postsynaptischen Zellmembran und binden dort an entsprechende Rezeptoren. Typische Rezeptoren für Neurotransmitter wie zum Beispiel Glutamat bilden einen Ionenkanal in der postsynaptischen Membran, wodurch es bei Bindung des Transmitters zu einem  $\text{Na}^+$ -Einstrom im postsynaptischen Neuron kommt, der eine Depolarisation der Zellmembran bewirkt.

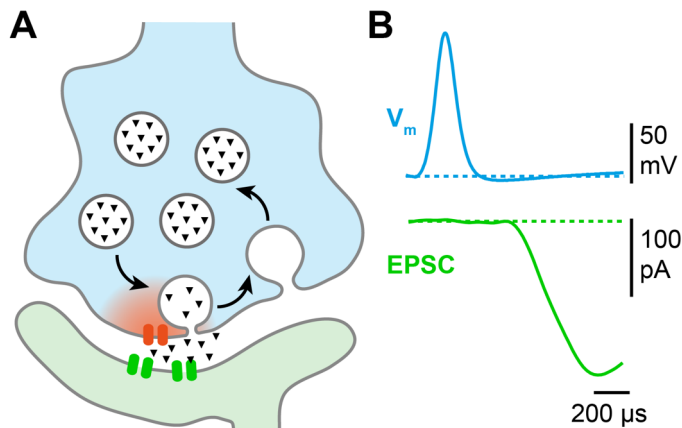


### Abb. 1: Synaptische Übertragung

(A) In der Präsynapse löst ein Aktionspotential einen  $\text{Ca}^{2+}$ -Einstrom durch  $\text{Ca}^{2+}$ -Kanäle (rot) aus. Daraufhin werden mit Neurotransmitter gefüllte Vesikel freigesetzt, der Transmitter (schwarze Dreiecke) diffundiert über den synaptischen Spalt und bindet an postsynaptische Rezeptoren (grün). (B) Das präsynaptische Aktionspotential ( $V_m$ , blau) führt mit nur kurzer Zeitverzögerung zu einem postsynaptischen Strom (EPSC, grün).

Die Vesikelfusion während der synaptischen Übertragung führt zu einer Vergrößerung der präsynaptischen Membranoberfläche. Diese zugewonnene Membran muss durch Endozytose wieder rückgeführt werden, um auf Dauer eine ungestörte Funktion und strukturelle Stabilität des präsynaptischen Neurons zu gewährleisten. Der Prozess der Endozytose kann zum Beispiel mit Hilfe von Elektronenmikroskopie (Heuser und Reese, 1973; Watanabe et al., 2013), Fluoreszenzmikroskopie (Hua et al., 2011; Kononenko et al., 2014; Ryan et al., 1996), oder Messungen der Zellmembrankapazität (Lou et al., 2008; von Gersdorff und Matthews, 1994) untersucht werden. In vorherigen Studien wurden die zeitlichen und mechanistischen Abläufe der Endozytose teilweise als sehr unterschiedlich beschrieben. Der Prozess der Endozytose an präsynaptischen Nervenendigungen ist daher Gegenstand einer kontroversen Diskussion (Kononenko und Haucke, 2015), die sich insbesondere auf den Zeitverlauf und die zugrunde liegenden Mechanismen bezieht.

Trotz intensiver Forschung sind einige der an der synaptischen Übertragung beteiligten Schritte bis heute nur unvollständig verstanden. Die Übertragung von einem prä- auf ein postsynaptisches Neuron findet an chemischen Synapsen meist in weniger als einer Millisekunde statt (Geiger und Jonas, 2000). Zwar sind viele der an synaptischer Übertragung beteiligten Proteine bekannt, doch welche genauen Mechanismen eine solch schnelle Signalübertragung ermöglichen ist bisher unklar. Auch ist unbekannt, in wie schneller Abfolge die komplexen Abläufe synaptischer Übertragung an zentralen Synapsen wiederholt stattfinden können.

## **1.2 Die Rolle hochfrequenter Übertragung im Zentralnervensystem**

Eine schnelle und präzise Informationsverarbeitung ist für die Funktion unseres Nervensystems von entscheidender Bedeutung, zum Beispiel um eine exakte Steuerung der Motorik zu gewährleisten. Dies hat dazu geführt, dass strukturelle und funktionelle Spezialisierungen von Axonen und Synapsen im Nervensystem eine erstaunlich schnelle Informationsverarbeitung ermöglichen. So besitzen die Aktionspotenziale in sensorisch afferenten Axonen von zum Beispiel Schnurrhaaren (Bale et al., 2015) oder der Cochlea (Wagner et al., 2005) eine zeitliche Präzision von ca. 20  $\mu$ s bei spezifischen Stimuli. Die Frequenz, mit der neuronale Signale weitergeleitet werden können, erhöht die Bandbreite an übertragbarer Information und ist ebenfalls äußerst wichtig für eine schnelle Informationsverarbeitung. Viele Neurone können Aktionspotenziale mit einer kontinuierlichen Rate von über 100 Hz (Blosa et al., 2015; van Kan et al., 1993), oder in Antwort auf einen Stimulus als kurze Signalfolge sogar mit über 1000 Hz (Garwicz et al., 1998; Rancz et al., 2007) feuern.

Ein einzelnes Neuron kann Informationen generell mittels *Ratenkodierung* (als mittlere Feuerrate) und/oder mittels *temporaler Kodierung* (als exakte

Zeitabstimmung des Aktionspotenzials) repräsentieren. Entsprechend ist eine Population an Nervenzellen in der Lage, Signale mittels Ratenkodierung oder temporaler Kodierung, aber auch mit Hilfe von Korrelationskodierung, Rangfolgenkodierung oder als räumlich-zeitliches Muster zu kodieren (Harris, 2005; Kumar et al., 2010; Rieke et al., 1997). Welche dieser Kodierungen im Zentralnervensystem dominiert, wird kontrovers diskutiert (London et al., 2010; Tchumatchenko et al., 2011; Wolfe et al., 2010). Allerdings scheint genereller Konsens zu herrschen, dass – wie bereits vor knapp einem Jahrhundert für Dehnungsrezeptoren im Muskel gezeigt wurde (Adrian und Zotterman, 1926) – die meisten sensorischen Neurone die Stärke eines Reizes als Frequenz der Aktionspotenziale enkodieren. Ebenfalls werden motorische Signale aus dem Zentralnervensystem ratenkodiert an die Muskulatur gesendet (Adrian und Bronk, 1929).

Die zeitliche Präzision einer Population an Nervenzellen, die Ratenkodierung verwenden, wird durch die Anzahl an Neuronen sowie die maximalen Feuerfrequenzen der jeweiligen Neurone determiniert (Rieke et al., 1997). Entwicklungsbiologische Zwänge wie Energieverbrauch und Größe und Gewicht

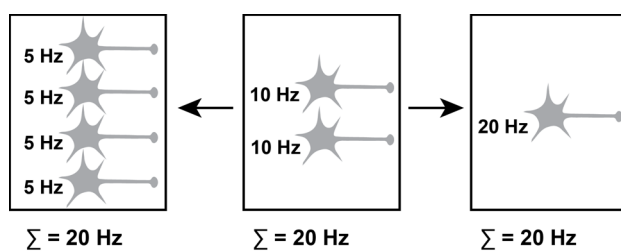
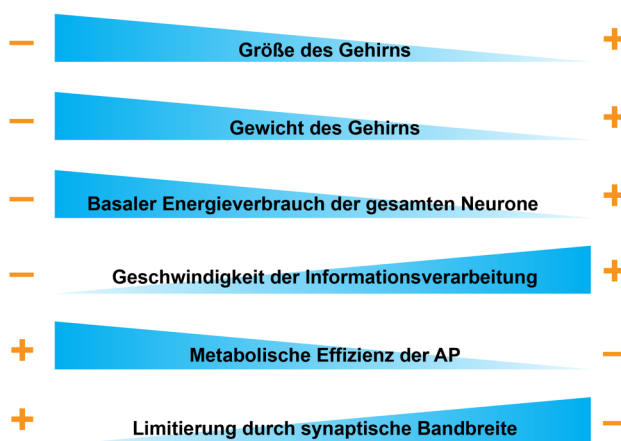


**Abb. 2: Vor- und Nachteile einer hochfrequenten neuronalen Kodierung**

Eine neuronale Population kann Information als (asynchrone) mittlere Aktionspotenzialfrequenz kodieren. Eine mittlere Feuerfrequenz von 20 Hz kann dabei z.B. durch vier Neurone mit je 5 Hz oder ein einzelnes Neuron mit 20 Hz Feuerrate erreicht werden. Eine geringere Anzahl an hochfrequenten Neuronen hat dabei folgende Vorteile: Die Größe und das Gewicht des Gehirns bleiben geringer, ebenso der basale Energieverbrauch aller Neurone des Nervensystems. Die Geschwindigkeit der neuronalen Informationsverarbeitung ist höher. Von Nachteil ist, dass die metabolische Effizienz der Aktionspotenziale sinkt, und dass die Informationsverarbeitung einer neuronalen Population stärker durch die synaptische Bandbreite limitiert wird.



des Nervensystems definieren daher höchstwahrscheinlich die optimale Anzahl an Neuronen und die maximale Feuerfrequenz dieser Zellen. Eine geringere Anzahl an Neuronen mit höheren Feuerraten haben in dieser Hinsicht verschiedene Vorzüge (Abbildung 2), weshalb das Nervensystem unter starkem evolutionärem Druck zu stehen scheint, hohe Aktionspotenzialfrequenzen und hochfrequente synaptische Übertragung zu nutzen.

### **1.3 Die zerebelläre Moosfaser-Körnerzell-Synapse**

Dem Kleinhirn wird eine zentrale Rolle bei der zeitlich präzisen Kontrolle von Bewegungen zugeschrieben. Eine vergleichsweise einfache anatomische Struktur liegt dieser Funktion zugrunde. In der weißen Substanz des Kleinhirns verlaufen afferente und efferente Fasern. Der zerebelläre Kortex kann in Körnerzellschicht, Purkinjellschicht und Molekularschicht aufgeteilt werden. Afferente sensorische Informationen erreichen den zerebellären Kortex über Kletter- und Moosfasern und ihre exzitatorischen Synapsen. Die Kletterfasern bilden Synapsen mit Purkinjellen aus, während die Information von Moosfasern in der Körnerzellschicht auf exzitatorische Interneurone, die zerebellären Körnerzellen, übertragen wird (Abbildung 3A). Die Körnerzellen wiederum bilden mit ihren Axonen, den so genannten Parallelfasern, in der Molekularschicht des zerebellären Kortex dann Synapsen mit mehreren Purkinjellen. Die Purkinjellen sind inhibitorische Zellen, die auf Neurone in den Kleinhirnkernen projizieren und damit die einzigen efferenten Neurone des zerebellären Kortex sind. Das Moosfaser-Körnerzell-Purkinjell-System ist in der Lage, mit erstaunlich hohen Aktionspotenzialfrequenzen zu arbeiten (Garwicz et al., 1998; Rancz et al., 2007; Valera et al., 2012; van Kan et al., 1993). Diese Eigenschaft scheint von wichtiger Bedeutung für die Verarbeitung von ratenkodierten sensorischen Informationen zu sein.

Moosfasern sind die myelinisierten Axone verschiedener Neurone im Hirnstamm oder Rückenmark, welche in den zerebellären Kortex projizieren. Im zerebellären Kortex bilden diese Moosfasern mehrere Kollateralen sowie viele Auftreibungen, so genannte Boutons, aus. Diese Moosfaserboutons (MFB) sind die Orte des synaptischen Kontakts zu Dendriten von etwa 10–100 postsynaptischen Körnerzellen pro MFB (Eccles et al., 1967; Jakab und Hámori, 1988; Ritzau-Jost et al., 2014). MFB haben meist eine komplexe Form und messen etwa 3–12  $\mu\text{m}$  im Durchmesser (Jakab und Hámori, 1988; Rollenhagen et al., 2007). Die präsynaptischen MFB bilden zusammen mit den Dendriten aller ihrer postsynaptischen Zellen eine glomeruläre Struktur, die von einer Glia-Hülle umgeben ist. Ultrastrukturelle Analysen ergaben, dass MFB tausende von synaptischen Vesikeln und eine Vielzahl an aktiven Zonen enthalten (Abbildung 3B; Kim et al., 2013; Xu-Friedman und Regehr, 2003), entsprechend der hohen Divergenz dieser Synapse. MFB setzen Glutamat als Neurotransmitter frei.

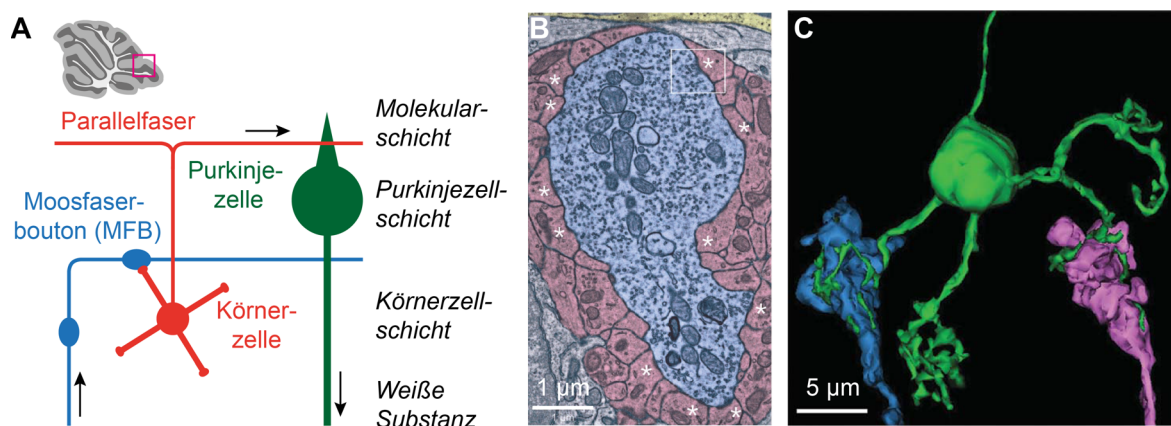


### Abb. 3: Anatomie der Moosfaser-Körnerzell-Synapse

(A) Oben: Sagittalschnitt durch das Kleinhirn. Unten: Schematische Darstellung der Moosfaser-Körnerzell-Synapse im zerebellären Kortex. Die Pfeile signalisieren die Richtung des neuronalen Informationsflusses. Andere Neurone des zerebellären Kortex werden aus Gründen der Übersichtlichkeit nicht dargestellt. (B) Elektronenmikroskopische Aufnahme eines MFB (blau). Synaptische Kontakte zu Körnerzeldendriten (rot) sind markiert (\*). Zu erkennen sind präsynaptische aktive Zonen, Mitochondrien sowie viele synaptische Vesikel im Zytosol der Präsynapse. Aus Xu-Friedman und Regehr (2003). (C) Dreidimensionale Rekonstruktion einer Körnerzelle (grün) mit zwei verbundenen MFB (blau und magenta). Man erkennt die komplexe anatomische Struktur der Moosfaser-Körnerzell-Synapse. Aus Livet et al. (2007).

Die Körnerzellen des Kleinhirns sind die häufigsten Neurone im menschlichen Gehirn (Williams und Herrup, 1988). Sie besitzen ein kleines Soma mit ca. 5–7  $\mu\text{m}$  Durchmesser und haben im Mittel vier kurze Dendriten (Abbildung 3C). Die Dendriten einer Körnerzelle sind in der Regel kürzer als 20  $\mu\text{m}$  und haben einen sehr dünnen Durchmesser von etwa 0.6  $\mu\text{m}$  (Cathala et al., 2003; Silver et al., 1992). Jeder Dendrit einer Körnerzelle endet in mehreren fingerförmigen Fortsätzen, die einen einzelnen MFB umschließen und dabei im Mittel drei synaptische Kontaktstellen ausbilden. Eine einzelne Körnerzelle kann mit ihren vier Dendriten sensorische Informationen von MFB unterschiedlichen Ursprungs erhalten (Chabrol et al., 2015; Livet et al., 2007). Körnerzellen haben ein dünnes Axon, das in die Molekularschicht aufsteigt, sich dort in zwei Parallelfasern verzweigt und in kleinen Boutons synaptische Verbindungen mit u.a. den Purkinjezellen eingeht.

Die relative Größe der präsynaptischen MFB erlaubt direkte Patch-Clamp Ableitungen sowohl *in vitro* als auch *in vivo* (Rancz et al., 2007). Solche präsynaptischen Ableitungen sind aktuell nur von wenigen Synapsen im Zentralnervensystem möglich. Auch die Körnerzellen bieten sehr gute Bedingungen für elektrophysiologische Messungen, wodurch die Anwendung hochauflösender Techniken sowohl auf prä- als auch auf postsynaptischer Seite möglich ist. Zudem wurde gezeigt, dass Moosfasern in der Lage sind, außergewöhnlich hohe Aktionspotenzialfrequenzen zu erreichen (Garwicz et al., 1998; Rancz et al., 2007). Aufgrund dieser Eigenschaften bietet die Moosfaser-Körnerzell-Synapse ideale Voraussetzungen, um die Mechanismen hochfrequenter synaptischer Übertragung genauer zu untersuchen. Bereits in früheren Arbeiten wurde mittels extrazellulären Ableitungen gezeigt, dass Moosfasern ratenkodierte sensorische Information an den zerebellären Kortex übermitteln (van Kan et al., 1993). Eine Untersuchung der Mechanismen synaptischer Übertragung an der Moosfaser-Körnerzell-Synapse kann daher einen wichtigen Beitrag leisten, das Verständnis der neuronalen Verarbeitung ratenkodierter Informationen zu verbessern.

## 2 Zielsetzung

Ziel dieser Arbeit war es, zu untersuchen, welche fundamentalen Mechanismen eine hochfrequente synaptische Übertragung im Zentralnervensystem ermöglichen. Zu diesem Zweck wurde die Moosfaser-Körnerzell-Synapse im Kleinhirn der Maus verwendet. Diese Synapse arbeitet mit sehr hohen Frequenzen und bietet im akuten Hirnschnitt sehr gute elektrophysiologische Ableitmöglichkeiten. Als zentrale Synapse ermöglicht dieses Präparat somit, entscheidende Erkenntnisse über die Mechanismen hochfrequenter synaptischer Übertragung zu gewinnen.

Im ersten Schritt wurde die maximale Feuerrate der präsynaptischen Axone gemessen und geprüft, ob solche Signale mit Frequenzen im Kilohertz-Bereich auf die postsynaptischen Körnerzellen übertragen werden können (Kapitel 3.1). Daraufhin wurden die Mechanismen untersucht, die derart schnelle präsynaptische Aktionspotenzialfrequenzen ermöglichen. Hierfür wurden sowohl prä- als auch postsynaptische Patch-Clamp Ableitungen eingesetzt und diese auch in Form von Paarableitungen kombiniert. Pharmakologische Experimente lieferten Erkenntnisse über die Subtypen der präsynaptischen Ionenkanäle in zerebellären Moosfasern und über deren Kinetik. Die Anwendung von präsynaptischen Kapazitätsmessungen und der Dekonvolution postsynaptischer Ströme ermöglichte zudem, wichtige Parameter der Fusion und der Bereitstellung synaptischer Vesikel mit hoher Auflösung zu charakterisieren.

Im Weiteren wurden präsynaptische quantitative  $\text{Ca}^{2+}$ -Konzentrationsmessungen mit Zweiphotonen-Fluoreszenzmikroskopie an der Moosfaser-Körnerzell-Synapse etabliert. In Kombination mit Computersimulationen der Diffusion und Pufferung von  $\text{Ca}^{2+}$ -Ionen konnte untersucht werden, wie präsynaptische  $\text{Ca}^{2+}$ -Signale mit hoher zeitlicher und räumlicher Präzision eine hochfrequente Vesikelfreisetzung vermitteln (Kapitel 3.2). Die quantitative Bestimmung der  $\text{Ca}^{2+}$ -Konzentration in Kombination mit hochaufgelösten lokalen Messungen lieferte dabei wichtige Erkenntnisse über die Mechanismen der präsynaptischen  $\text{Ca}^{2+}$ -

Pufferung. Die experimentell gewonnenen Daten determinierten daraufhin entscheidende Randbedingungen der Simulationen.

Um die Integration der eingehenden synaptischen Informationen an der Moosfaser-Körnerzell-Synapse besser zu verstehen, wurden direkte Patch-Clamp Ableitungen von Dendriten der Körnerzellen etabliert (Kapitel 3.3). Diese Technik wurde bisher nur an deutlich größeren Dendriten von zum Beispiel kortikalen Pyramidenzellen angewandt. Mit Hilfe dieser dendritischen Ableitungen war es möglich, die elektrotonische Kopplung zwischen den Dendriten und dem Soma von Körnerzellen zu quantifizieren und zu untersuchen, wie stark synaptische Potenziale durch die elektrischen Eigenschaften der Dendriten abgeschwächt werden.

Zuletzt wurde die Frage untersucht, mit welcher Geschwindigkeit und welchen molekularen Mechanismen die Endozytose präsynaptischer Membranfläche an der Moosfaser-Körnerzell-Synapse abläuft. Dazu wurden präsynaptische Patch-Clamp Ableitungen und Kapazitätsmessungen verwendet. Diese Methoden wurden in Hinsicht auf Auflösung und Signal-zu-Rauschverhältnis optimiert, sodass erstmalig die mit einem einzelnen Aktionspotenzial verbundene Exo- und Endozytose gemessen werden konnte. Mit Hilfe dieser entsprechend verbesserten Messtechnik konnte der Zeitverlauf der Endozytose genau charakterisiert werden (Kapitel 3.4). Pharmakologische Interventionen erlaubten zudem, die molekularen Mechanismen der Endozytose weiter aufzuschlüsseln.



### **3 Originalarbeiten**

**3.1 Ritzau-Jost\*, Delvendahl\* et al. 2014 Neuron 84, 152–163.**

Seite 14–25

# Ultrafast Action Potentials Mediate Kiloherzt Signaling at a Central Synapse

Andreas Ritzau-Jost,<sup>1,2,5</sup> Igor Delvendahl,<sup>1,2,5</sup> Annika Rings,<sup>1,2,5</sup> Niklas Byczkowitz,<sup>1,2</sup> Harumi Harada,<sup>3</sup> Ryuichi Shigemoto,<sup>3</sup> Johannes Hirrlinger,<sup>1,4</sup> Jens Eilers,<sup>1</sup> and Stefan Hallermann<sup>1,2,\*</sup>

<sup>1</sup>Carl-Ludwig-Institute for Physiology, Medical Faculty, University of Leipzig, Liebigstr. 27, 04103 Leipzig, Germany

<sup>2</sup>European Neuroscience Institute Göttingen, Grisebachstr. 5, 37077 Göttingen, Germany

<sup>3</sup>Institute of Science and Technology Austria, 3400 Klosterneuburg, Austria

<sup>4</sup>Department of Neurogenetics, Max-Planck-Institute for Experimental Medicine, Hermann-Rein-Strasse 3, 37075 Göttingen, Germany

<sup>5</sup>Co-first author

\*Correspondence: [hallermann@medizin.uni-leipzig.de](mailto:hallermann@medizin.uni-leipzig.de)

<http://dx.doi.org/10.1016/j.neuron.2014.08.036>

## SUMMARY

Fast synaptic transmission is important for rapid information processing. To explore the maximal rate of neuronal signaling and to analyze the presynaptic mechanisms, we focused on the input layer of the cerebellar cortex, where exceptionally high action potential (AP) frequencies have been reported *in vivo*. With paired recordings between presynaptic cerebellar mossy fiber boutons and postsynaptic granule cells, we demonstrate reliable neurotransmission up to ~1 kHz. Presynaptic APs are ultrafast, with ~100  $\mu$ s half-duration. Both  $K_{v1}$  and  $K_{v3}$  potassium channels mediate the fast repolarization, rapidly inactivating sodium channels ensure metabolic efficiency, and little AP broadening occurs during bursts of up to 1.5 kHz. Presynaptic  $Ca_v2.1$  (P/Q-type) calcium channels open efficiently during ultrafast APs. Furthermore, a subset of synaptic vesicles is tightly coupled to  $Ca^{2+}$  channels, and vesicles are rapidly recruited to the release site. These data reveal mechanisms of presynaptic AP generation and transmitter release underlying neuronal kHz signaling.

## INTRODUCTION

Information can be encoded by neural activity as the rate of action potentials (APs) (Arenz et al., 2008; London et al., 2010) and by correlations in spike timing (Rieke et al., 1997). The propagation speed of rate-coded information within a population of neurons is limited by the number of neurons and by the maximal AP frequency of each individual neuron (Rieke et al., 1997; Tchumachenko et al., 2011). In turn, the maximal sustainable frequency of each neuron is ultimately limited by the duration of the AP (Bean, 2007; Gittis et al., 2010; Lien and Jonas, 2003; Rudy and McBain, 2001). Therefore, the AP duration is a crucial parameter limiting the speed of information processing.

Cerebellar mossy fibers represent one of the main inputs to the cerebellum and send broad-bandwidth signals to the cerebellar cortex with firing frequencies up to 1.2 kHz *in vivo* (Garwicz et al.,

1998; Jörntell and Ekerot, 2006; Rancz et al., 2007). These high-frequency signals are conveyed to granule cells (GCs), the most abundant neurons in the entire brain. In order to connect to the large number of GCs, cerebellar mossy fibers form several collaterals and contain numerous presynaptic boutons along the myelinated axon. In addition, each cerebellar mossy fiber bouton (cMFB) contacts more than 10 GCs (Billings et al., 2014; Jakab and Hámori, 1988). Despite the high degree of divergence at cMFBs, signal transduction to the postsynaptic partners is very efficient (Chadderton et al., 2004; Jörntell and Ekerot, 2006; Rancz et al., 2007; Saviane and Silver, 2006). In a seminal study, Rancz and coworkers (2007) pioneered direct whole-cell patch-clamp recordings from cMFBs *in vitro* and *in vivo*, offering the opportunity to directly investigate the mechanisms of high-frequency signaling from single nerve terminals to a large number of postsynaptic partners.

Here, we establish paired patch-clamp recordings between cMFBs and GCs in acute cerebellar brain slices in combination with high-resolution analysis of presynaptic mechanisms. We focus on the properties of APs in cMFBs enabling kHz signaling and the mechanisms by which cMFBs can reliably release neurotransmitter to dozens of GCs. Our recordings demonstrate reliable neurotransmission at frequencies of up to ~1 kHz and reveal a surprisingly short duration of APs, which is more than 2-fold shorter than previous estimates at central neurons or axons. Furthermore, we show that efficient opening of presynaptic  $Ca^{2+}$  channels, tight coupling of vesicles to  $Ca^{2+}$  channels, and rapid vesicle recruitment sustain reliable neurotransmitter release during kHz signaling.

## RESULTS

### Kiloherzt Transmission at Single cMFB-GC Connections

Synaptic transmission of individual cMFB-GC connections was analyzed with paired whole-cell patch-clamp recordings from cMFBs and GCs in acute cerebellar brain slices of mature mice at physiological temperatures (schematically illustrated in Figure 1A). Recordings from cMFBs were obtained with the aid of two-photon targeted patching (Margrie et al., 2003) in transgenic mice expressing yellow fluorescent protein in a subset of mossy fibers (Figure 1B; Hirrlinger et al., 2005) or with differential interference contrast microscopy in wild-type mice. For an

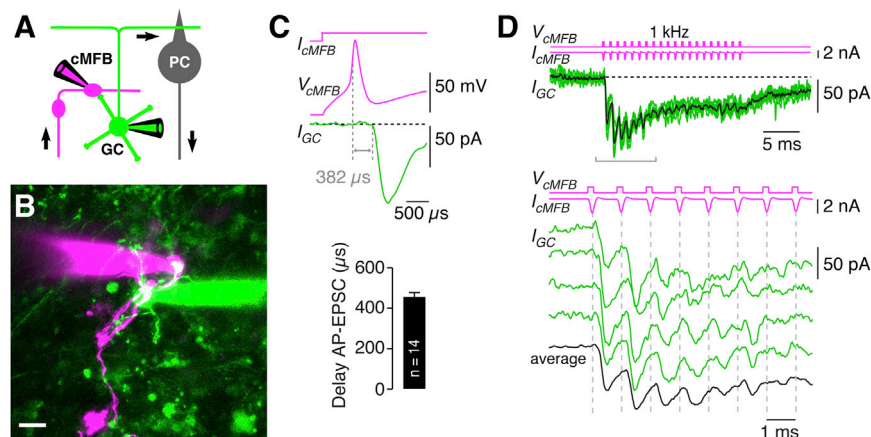


**Figure 1. Kilohertz Transmission at Single cMFB-GC Connections**

(A) Schematic illustration of the cellular connectivity within the cerebellar cortex. Mossy fibers (magenta) send information to the cerebellar cortex. Presynaptic cerebellar mossy fiber boutons (cMFB) transmit signals to postsynaptic granule cells (GCs, green), which excite Purkinje cells (PC, gray) via parallel fibers. Axons of Purkinje cells represent the sole output of the cerebellar cortex. Two patch-clamp pipettes illustrate the paired cMFB-GC recording configuration.

(B) Two-photon microscopic image of a paired whole-cell patch-clamp recording between a cMFB (magenta) and a GC (green) filled with the fluorescence dyes Atto 594 and Atto 488, respectively, in an acute cerebellar brain slice of a 39-day-old TgN(Thy1.2-EYFP) mouse expressing

EYFP in a subset of mossy fibers (green; maximal z-projection of a stack of images over 45  $\mu$ m; z-step 3  $\mu$ m). Scale bar, 10  $\mu$ m.

(C) Top: Example trace of a paired cMFB-GC recording with current injection ( $I_{cMFB}$ ) evoking an AP in the cMFB ( $V_{cMFB}$ ) and an EPSC in the postsynaptic GC ( $I_{GC}$ ). The synaptic delay is indicated. Bottom: Average synaptic delay of  $n = 14$  paired recordings (mean  $\pm$  SEM).

(D) Top: Voltage clamp of a cMFB with 20 AP-like depolarizations ( $V_{cMFB}$ ; 200  $\mu$ s to 0 mV) at a frequency of 1 kHz evoked presynaptic action currents in the cMFB ( $I_{cMFB}$ ) and EPSCs in the connected GC (four consecutive trials in green, average in black). Bottom: the first seven EPSCs on an expanded scale (cf. bracket in top panel, dashed lines are set to the peak of the action currents; see also Figure S1).

unequivocal identification of cMFBs, we determined the characteristic morphological and electrophysiological properties (see Supplemental Experimental Procedures; Figure S1; Rancz et al., 2007). Brief current injection into cMFBs evoked an AP in the cMFB and an excitatory postsynaptic current (EPSC) in a synaptically connected GC with a synaptic delay of  $457 \pm 20 \mu$ s ( $n = 14$ ; Figure 1C). To directly analyze transmission in the kHz regime, presynaptic stimulation with 20 AP-like depolarizations (0 mV, 200  $\mu$ s duration) at a frequency of 1 kHz was used to evoke presynaptic action currents in cMFBs. These presynaptic kHz bursts evoked EPSCs in GCs, consisting of a phasic EPSC, which is related to direct release onto the GC, and a tonic component, part of which is probably due to glutamate spillover from neighboring release sites onto the recorded GC (Figure 1D; DiGregorio et al., 2002). In the example shown in Figure 1D, the average phasic steady-state amplitude of the last ten EPSCs was 8.1 pA. When taking into account the previously reported reduction in EPSC amplitude due to postsynaptic depression of  $\sim 30\%$  and the miniature EPSC amplitude of 17 pA (Hallermann et al., 2010), this corresponds to release of about one vesicle each millisecond in this cMFB-GC connection (see below for detailed analysis of the rate of vesicle recruitment). This example demonstrates that a single cMFB-GC connection can reliably transmit information during short bursts at a frequency of 1 kHz.

### Ultrafast APs in cMFBs

In order to understand the mechanisms of high-frequency burst signaling, we next analyzed the properties of presynaptic APs. Upon current injection, cMFBs fired APs with durations at half-maximal amplitude of  $107 \pm 4 \mu$ s ( $n = 44$ ; referred to as half-duration in the following; Figure 2B). To analyze APs undisturbed by a presynaptic depolarization, cMFBs and the adjacent axon were filled with a fluorescent dye (Figure 2A) and a distal part of the axon was approached with a stimulation pipette. We systematically compared APs elicited by current injection and axonal stim-

ulation. The half-duration of APs elicited in the same cMFB was not significantly different between the two modes of AP generation ( $n = 10$ ,  $p = 0.1$ , Wilcoxon signed-rank test; Figure 2C). These data demonstrate that APs of cMFBs are ultrafast with a half-duration of  $\sim 100 \mu$ s.

To gain insights into the mechanisms allowing such short AP half-duration, we analyzed which  $K^+$  channel subtypes are responsible for AP repolarization. Focal application of the  $K_{v3}$  channel gating modifier BDS-I (3  $\mu$ M; Martina et al., 2007) prolonged AP half-duration to  $202 \pm 14 \mu$ s ( $n = 11$ ,  $p < 0.001$ , Mann-Whitney U test), whereas bath application of the  $K_{v1}$  channel blocker  $\alpha$ -dendrotoxin (DTX, 0.2 mM) prolonged the half-duration to  $265 \pm 27 \mu$ s ( $n = 11$ ,  $p < 0.001$ , Mann-Whitney U test; Figures 2D, 2E, and S2). The impact of  $K_{v3}$  channels could be underestimated in these experiments because of incomplete focal application of BDS-I or the fact that BDS-I only slows gating but does not block  $K_{v3}$  completely (Martina et al., 2007). However, bath application of 1 mM TEA, which blocks  $K_{v1.1}$  and all  $K_{v3}$  channel subtypes (Gutman et al., 2005), did not have a stronger effect on AP half-duration than focal BDS-I application ( $p = 0.75$ ; Mann-Whitney U test; Figure 2E). This finding indicates that BDS-I application was successful and that the slowing of the  $K_{v3}$  activation kinetics by BDS-I (Martina et al., 2007) corresponds to a complete  $K_{v3}$  block during the duration of our APs. Finally, application of 5 mM 4-AP, which blocks  $K_{v1}$  and  $K_{v3}$  channels, resulted in APs with half-durations of  $\sim 1$  ms ( $n = 5$ ,  $p < 0.001$ , Mann-Whitney U test; Figures 2D and 2E). Although we have not addressed  $K_{v2}$  and  $K_{v4}$  channels specifically, a strong contribution to the AP repolarization is unlikely, because  $K_{v2}$  channels activate slowly and contribute only to repolarization of longer APs (Liu and Bean, 2014), and  $K_{v4}$  channels have been shown to localize preferentially to somata and dendrites (Sheng et al., 1992). These data indicate that primarily  $K^+$  channels of the  $K_{v1}$  and the  $K_{v3}$  channel families mediate the repolarization of ultrafast cMFB APs.

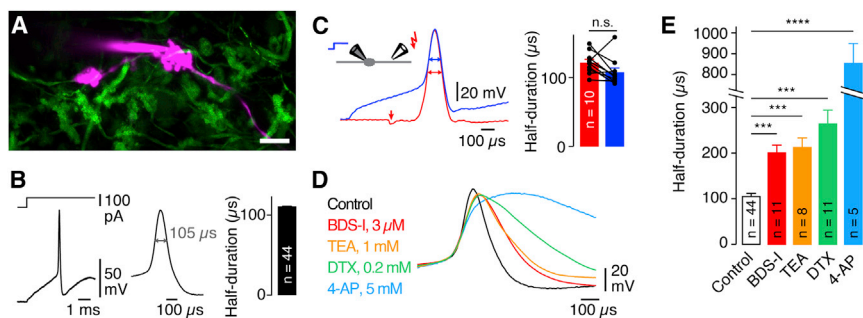


**Figure 2. Ultrafast APs in cMFBs**

(A) Two-photon image of a whole-cell patch-clamped cMFB and the adjacent axon (magenta; Atto 594 in the pipette solution) in an acute cerebellar brain slice of a 48-day-old TgN(Thy1.2-EYFP) mouse with EYFP-labeled mossy fibers (green; maximal z-projection of a stack of images over 20 μm; z-step 1 μm). Scale bar, 10 μm.

(B) Example of an AP recorded in a cMFB evoked by current injection. Middle: Same example on an expanded time scale (AP half-duration is indicated). Right: Average AP half-duration elicited by current injection (mean ± SEM; n refers to the number of cMFBs).

(C) Left: Comparison of APs elicited by current injection (blue) and axonal stimulation with a second pipette (red) in the same cMFB as illustrated by the color code of the inset. Example APs elicited in both ways are superimposed (arrow indicates stimulation artifact). Right: Comparison between the AP half-duration elicited by axonal stimulation (red) and current injection (blue) in the same cMFBs (mean ± SEM; connected dots represent results from the two stimulation conditions in the same cMFB).

(D) Examples of cMFB APs measured in the presence of indicated K<sup>+</sup> channel blockers. APs were evoked by current injection. Voltage traces are aligned to the AP threshold.

(E) Average AP half-duration after application of the indicated K<sup>+</sup> channel blockers (mean ± SEM). Asterisks indicate significance as described in the text (see also Figure S2).

### Fast Inactivating Na<sup>+</sup> and Activating K<sup>+</sup> Channels Generate Ultrafast and Metabolically Efficient APs

We next applied an AP waveform (measured in cMFBs with axonal stimulation) as voltage command to outside-out patches from cMFBs to analyze the Na<sup>+</sup> and K<sup>+</sup> currents underlying the fast cMFB APs. The pharmacologically isolated currents had very short half-durations of  $73 \pm 9 \mu\text{s}$  ( $n = 6$ ) and  $61 \pm 2 \mu\text{s}$  ( $n = 5$ ; Figures 3A and 3B) for Na<sup>+</sup> and K<sup>+</sup>, respectively. Metabolic efficiency was quantified as the Na<sup>+</sup> excess ratio, defined as the total Na<sup>+</sup> influx (Na<sup>+</sup> current integrated over the entire duration of the AP) divided by the Na<sup>+</sup> flux until the time of the AP peak (Figure 3C). The Na<sup>+</sup> excess ratio was  $1.76 \pm 0.12$  ( $n = 6$ ), which is efficient compared with APs of short duration at other preparations (Carter and Bean, 2009, 2011).

To analyze the mechanisms that generate ultrafast but metabolically efficient APs, we studied the kinetic parameters of Na<sup>+</sup> and K<sup>+</sup> currents. Step-depolarizations from  $-80$  to  $0$  mV applied to outside-out patches revealed rapid Na<sup>+</sup> channel inactivation with a time constant of  $81 \pm 3 \mu\text{s}$  ( $n = 5$ ; Figure 3D), which is consistent with corresponding recordings from axons of fast-spiking interneurons at room temperature, assuming a Q<sub>10</sub> temperature coefficient of 2.6 (time constant  $\sim 300 \mu\text{s}$ ; Hu and Jonas, 2014). Maximally activating voltage steps from  $-80$  to  $+40$  mV were applied to investigate the kinetics of K<sup>+</sup> currents at cMFBs. The activation time constant was  $225 \pm 24 \mu\text{s}$  ( $n = 12$ ; Figure 3E), which is consistent with previous studies of rapidly activating K<sup>+</sup> channels (Martina et al., 2007). Thus, rapid inactivation of Na<sup>+</sup> and activation of K<sup>+</sup> channels underlie efficient cMFB APs.

In order to further dissect whether the kinetics or rather the density of Na<sup>+</sup> and K<sup>+</sup> channels cause the short half-duration of the APs, we estimated current densities from outside-out patches and performed Hodgkin-Huxley modeling based on the measured gating kinetics (Figure S3; see Supplemental Experimental Procedures). However, with the estimated Na<sup>+</sup> and K<sup>+</sup> conductance ( $\bar{g}_{\text{Na}} = 722$  and  $\bar{g}_{\text{K}} = 82 \text{ pS} \cdot \mu\text{m}^{-2}$ ), the model predicted a too-long half-duration (Figure S3E). To obtain the measured half-duration, a  $\sim 10$ -fold higher K<sup>+</sup> current density was required. An inhomogeneous distribution of K<sup>+</sup> channels

could explain this finding (see Discussion). Thus, our approach of high-resolution kinetic analysis of Na<sup>+</sup> and K<sup>+</sup> currents in combination with Hodgkin-Huxley modeling provides indirect evidence for an inhomogeneous distribution of K<sup>+</sup> channels and indicates a high density of Na<sup>+</sup> channels.

### Stable APs during kHz Bursts

We evoked presynaptic APs by axonal stimulation at increasing rates (250–2,000 Hz) to analyze the AP shape during high-frequency firing. cMFBs were capable of firing failure-free trains of APs at exceptionally high frequencies (Figure 4A). In the illustrated example, failure-free trains of APs were elicited at up to 1.6 kHz and had almost constant amplitude and half-duration up to 1 kHz (Figures 4A and 4B), suggesting a rapid recovery from sodium channel inactivation (Leão et al., 2005). At frequencies close to the maximal failure-free frequency, slight amplitude reduction and broadening occurred, which fully recovered within a few tens of milliseconds (Figure 4B). Interestingly, the maximal failure-free AP frequency correlated with the AP half-duration (Figure 4C). On average, failure-free frequency for 11 APs was  $1.0 \pm 0.1 \text{ kHz}$  ( $n = 10$ ; Figure 4D). At the frequency tested before the maximal failure-free frequency (mean  $800 \pm 89.8 \text{ Hz}$ ), last AP half-duration was  $111 \pm 2.5\%$ , and AP amplitude  $95.1 \pm 1.7\%$  of the first AP ( $n = 10$ ). These data are similar to findings obtained at the calyx of Held (Wang and Kaczmarek, 1998) and at cMFBs in vivo (Rancz et al., 2007). In contrast, nerve terminals operating at lower frequencies, such as hippocampal mossy fiber boutons, exhibit pronounced AP broadening even at frequencies of 1–100 Hz (Geiger and Jonas, 2000). Thus, cMFBs can generate APs at kHz frequencies with little amplitude reduction and broadening.

### Efficient Opening of Ca<sup>2+</sup> Channels during cMFB APs

In order to understand the mechanisms of synaptic transmission at these frequencies, we next investigated whether the ultrafast APs in cMFBs can reliably open Ca<sup>2+</sup> channels. With optimized recording conditions (see Supplemental Experimental Procedures), AP-evoked Ca<sup>2+</sup> currents (Borst and Sakmann, 1998)



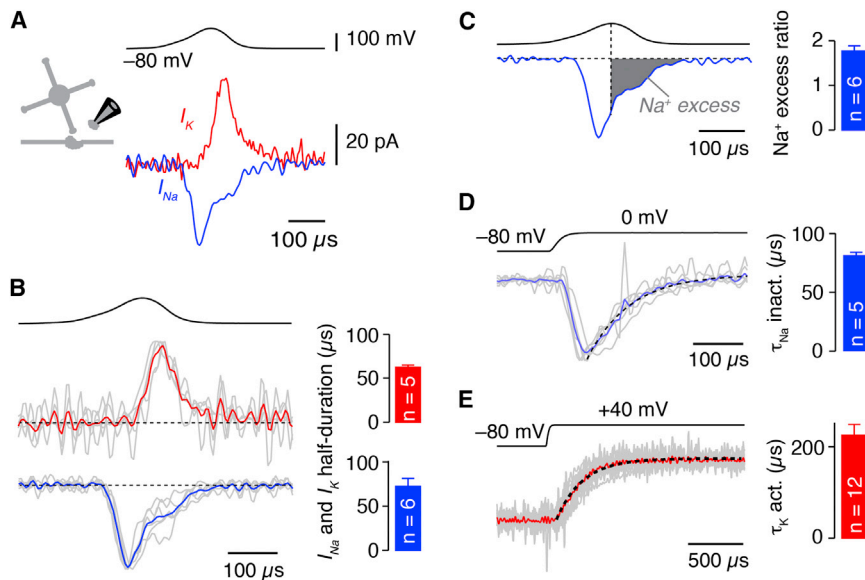


**Figure 3. Fast Inactivating Na<sup>+</sup> and Activating K<sup>+</sup> Channels Generate Ultrafast and Metabolically Efficient APs**

(A) Examples of pharmacologically isolated Na<sup>+</sup> (blue) and K<sup>+</sup> currents (red) in two different outside-out patches from cMFBs, elicited by a previously recorded AP voltage command (top). Traces are averages of 82 and 101 sweeps for Na<sup>+</sup> and K<sup>+</sup> currents, respectively. Inset: Schematic illustration of the recording configuration.

(B) Superposition of peak normalized AP-evoked currents (gray traces; n = 6 for Na<sup>+</sup>, n = 5 for K<sup>+</sup>; n represents number of outside-out patches) with the corresponding grand averages (Na<sup>+</sup>, blue; K<sup>+</sup>, red). Right: Average half-duration of AP-evoked Na<sup>+</sup> (blue) and K<sup>+</sup> current (red; mean ± SEM).

(C) Average AP-evoked Na<sup>+</sup> current. Filled gray area indicates the excess Na<sup>+</sup> influx following the peak of the AP. Right: Average Na<sup>+</sup> excess ratio calculated as total Na<sup>+</sup> influx divided by the Na<sup>+</sup> influx until the time of the AP peak (mean ± SEM).

(D) Superposition of peak normalized Na<sup>+</sup> currents (n = 5, gray) elicited by 3 ms depolarization from

–80 mV to 0 mV with the grand average (blue) and an exponential fit to the time course of inactivation (black dashed line). Right: Average time constant of inactivation (mean ± SEM).

(E) Superposition of peak normalized K<sup>+</sup> currents (n = 12, gray) evoked by 3 ms depolarizations from –80 mV to +40 mV with the grand average (red) and an exponential fit to the time course of activation (black dashed line). Right: Average time constant of activation (mean ± SEM; see also Figure S3).

could be resolved having an amplitude of  $543 \pm 62$  pA and a half-duration of  $99 \pm 4$   $\mu$ s (n = 9; Figure 5A). To determine the relative open probability of Ca<sup>2+</sup> channels during an AP, Ca<sup>2+</sup> currents were elicited by AP-like depolarizations of variable duration (Figure 5B). On average, 59% of the available Ca<sup>2+</sup> current was recruited during an AP (Figure 5C). To understand the efficient opening during short APs, we measured the kinetics of Ca<sup>2+</sup> currents in cMFBs and found rapid activation and deactivation (Figures S4A and S4B). A two-gate Hodgkin-Huxley model based on the measured activation and deactivation kinetics (Figure S4C) reproduced the AP-evoked Ca<sup>2+</sup> current (Figure 5A) and predicted a relative open probability of 77% during an AP. Thus, rapid kinetics of presynaptic Ca<sup>2+</sup> channels can explain the efficient opening of Ca<sup>2+</sup> channels during short APs at cMFBs.

#### Ca<sub>v</sub>2.1 Ca<sup>2+</sup> Channels at Active Zones of cMFBs

To identify the molecular identity of the presynaptic Ca<sup>2+</sup> channels at cMFBs, whole-cell Ca<sup>2+</sup> currents were recorded during application of specific Ca<sup>2+</sup> channel blockers (Figure 6A).  $\omega$ -Aga-toxin (0.5  $\mu$ M), which selectively blocks Ca<sub>v</sub>2.1 (P/Q-type) Ca<sup>2+</sup> channels, inhibited  $70.8\% \pm 4.3\%$  (n = 10) of the Ca<sup>2+</sup> current. In contrast, 1  $\mu$ M  $\omega$ -Conotoxin, which blocks Ca<sub>v</sub>2.2 (N-type) Ca<sup>2+</sup> channels, and 0.5  $\mu$ M SNX-482, which blocks Ca<sub>v</sub>2.3 (R-type) Ca<sup>2+</sup> channels, inhibited only  $15.5\% \pm 2.8\%$  (n = 11) and  $11.9\% \pm 1.8\%$  (n = 5) of the Ca<sup>2+</sup> current, respectively (Figure 6B). Thus, Ca<sub>v</sub>2.1 Ca<sup>2+</sup> channels mediate the majority of the Ca<sup>2+</sup> current at cMFBs. To investigate whether these channels are localized at the active zone, we analyzed the localization of Ca<sub>v</sub>2.1 Ca<sup>2+</sup> channels using pre-embedding immunogold labeling for Ca<sub>v</sub>2.1 in mice (Indriati et al., 2013). Immunogold particles

for Ca<sub>v</sub>2.1 were often found in the presynaptic active zone of cMFBs making synapses onto granule cell dendrites (Figure 6C). The density of particles was  $\sim 50$  times higher at the active zone compared with extrasynaptic membrane (Figure 6D). Consistently, freeze-fracture replica labeling of cerebellar granule cell layer also showed clustered Ca<sub>v</sub>2.1 Ca<sup>2+</sup> channels at putative active zones of cMFBs (Figure 6E). These data indicate that Ca<sub>v</sub>2.1 Ca<sup>2+</sup> channels, which are clustered at active zones, represent the majority of Ca<sup>2+</sup> channels at cMFBs.

#### Measuring Vesicular Release Simultaneously from Presynaptic Capacitance Increase and Postsynaptic Currents

To understand how the brief Ca<sup>2+</sup> influx can elicit synchronous release during kHz bursts, we next analyzed fundamental parameters of release, such as the number of release-ready vesicles, the speed of vesicle recruitment, and the vesicle to Ca<sup>2+</sup> channel coupling distance. We combined two independent techniques to measure these parameters in the paired-recording configuration: presynaptic capacitance measurements and deconvolution of postsynaptic currents (Sakaba, 2006; Sun and Wu, 2001; von Gersdorff et al., 1998; Wölfel et al., 2007). Depolarizing pulses of increasing duration (0 mV; 1–100 ms) were applied to the presynaptic terminal (Figure 7A). The presynaptic Ca<sup>2+</sup> current, the induced capacitance increase due to vesicle exocytosis, and the evoked postsynaptic current were measured simultaneously. Deconvolution of postsynaptic currents led to an estimate of presynaptic release rates during the pulses (Figure 7A; see Supplemental Experimental Procedures). The capacitance increase and the number of vesicles estimated by deconvolution scaled linearly for depolarizations of 1–100 ms

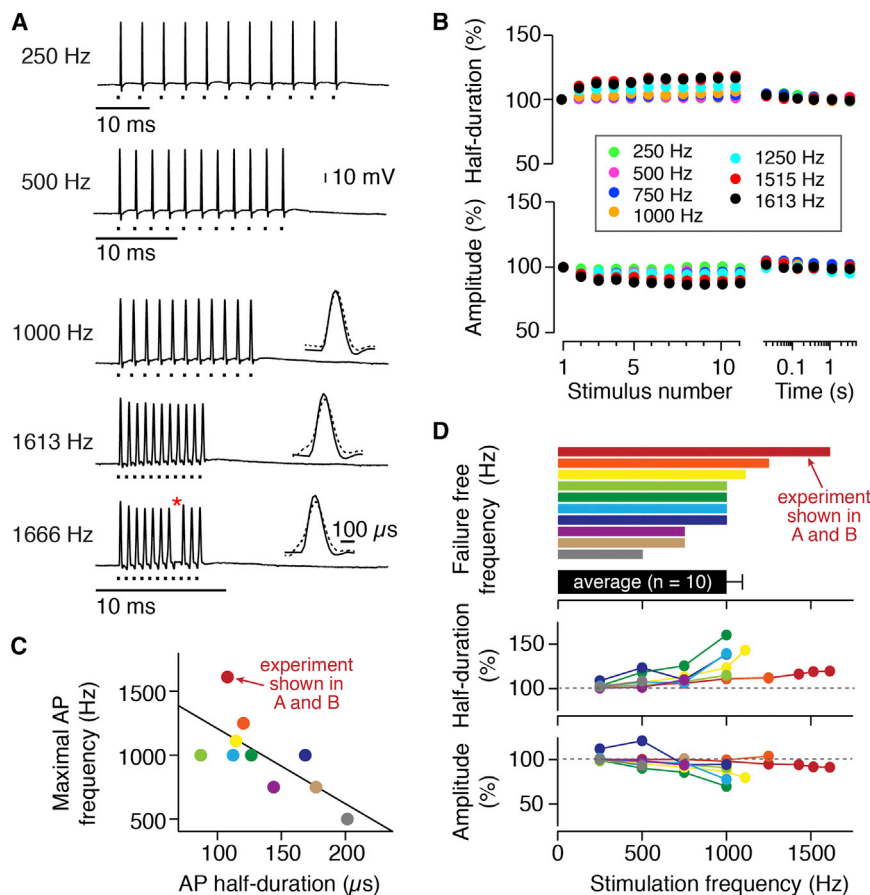


**Figure 4. Stable APs during kHz Bursts**

(A) Examples of APs recorded in a cMFB elicited at the indicated frequencies by axonal stimulation with an extracellular stimulation pipette (stimulation time points are indicated as dots below the traces; lowest scale bar applies to all three lowest traces). An overlay of the first (solid) and last (11<sup>th</sup>, dashed) AP is shown on the right. Note the failure after the seventh AP at 1,666 Hz (red asterisk).

(B) Time course of AP broadening and amplitude reduction of the experiment shown in (A) at the color-coded frequencies. The amplitude and half-duration of 11 APs during the train are plotted versus the stimulus number (normalized to the first AP). The properties of the APs that were elicited with increasing intervals following the train stimulation (not shown in A) are plotted versus the time after the end of the train. Note the stable half-duration and amplitude during bursts of up to 1 kHz frequency.

(C) Correlation of the maximal failure-free AP frequency and the AP half-duration recorded in  $n = 10$  mossy fibers (Pearson's correlation coefficient  $R = -0.71$ ;  $p = 0.02$ ).

(D) Maximum failure-free frequency plotted versus stimulation frequency (top). The black bar shows the mean  $\pm$  SEM ( $n = 10$ ); colors indicate individual experiments. Corresponding half-duration (middle) and amplitude (bottom) of the last AP in the train normalized to the first AP.

(Figure 7B). Whereas capacitance measurements sample the total release from the entire cMFB, deconvolution based on the postsynaptic current from a GC samples only the fraction of total release of the cMFB that is directed toward the single GC recorded from (see illustration in Figure 7A). Therefore, quantitative comparison of the number of released vesicles with both techniques results in an estimate of the number of postsynaptic GCs per cMFB for each cMFB-GC pair. Assuming a single vesicle capacitance of 70 aF, the comparison revealed on average  $100 \pm 10$  GCs per cMFB (Figure 7C,  $n = 10$  cell pairs). This is higher than previous estimates ( $\sim 10$ , Billings et al., 2014;  $\sim 50$ , Jakab and Hámori, 1988), but, e.g., a bias towards larger terminals, ectopic vesicle release, postsynaptic rundown, or release onto Golgi cells would lead to an overestimation of the connectivity ratio. Thus, we established two independent techniques with high temporal resolution, which allowed us to measure release at cMFBs directly.

#### Ultrafast Vesicle Recruitment and Tight $\text{Ca}^{2+}$ Channel-Vesicle Coupling

Next we determined the number of release-ready vesicles, a central parameter to understanding the mechanisms of high-frequency synaptic transmission (Hallermann and Silver, 2013; Neher, 2010). The release rate based on deconvolution techniques showed an initial peak and a subsequent sustained part (cf. Figure 7A). The first peak most likely reflects fusion of

release-ready vesicles, whereas the sustained part reflects vesicle recruitment (Sakaba and Neher, 2001b). Analysis of the cumulative release rates (Figure 8A) revealed that the initial release was best described by two exponential components with time constants of  $0.43 \pm 0.05$  and  $5.6 \pm 1.4$  ms (consisting of  $N_1 = 15.2 \pm 4.3$  and  $N_2 = 7.3 \pm 1.4$  vesicles;  $n = 10$ ; Table S1). These estimates of the number of release-ready vesicles are slightly higher than estimates using extracellular stimulation techniques (5–10 vesicles; Saviane and Silver, 2006; Hallermann et al., 2010), but much smaller than estimates at the calyx of Held (range 700–5,000; Borst and Soria van Hoeve, 2012). The sustained part was well described by a line with an average slope of  $358 \pm 132$  vesicles  $\cdot$  s $^{-1}$  ( $n = 10$ ; Figure 8A; Table S1). These data indicate two populations of release-ready vesicles and a rapid recruitment speed of  $\sim 350$  vesicles  $\cdot$  s $^{-1}$ , which can be sustained for up to 100 ms.

To analyze the coupling distance of vesicles to  $\text{Ca}^{2+}$  channels, we substantially increased the intrabouton  $\text{Ca}^{2+}$  buffering by raising the concentration of the slow  $\text{Ca}^{2+}$  buffer EGTA in the presynaptic solution from our control value of 200  $\mu$ M to 5 mM. The time constant and the amplitude of the first component of release were not significantly changed by 5 mM EGTA ( $p = 0.42$  and  $0.96$ , respectively, Mann-Whitney U test; Figure 8A), which indicates that these vesicles are tightly coupled to  $\text{Ca}^{2+}$  channels. However, including 5 mM EGTA in the presynaptic pipette resulted in a decrease of the slowly releasing

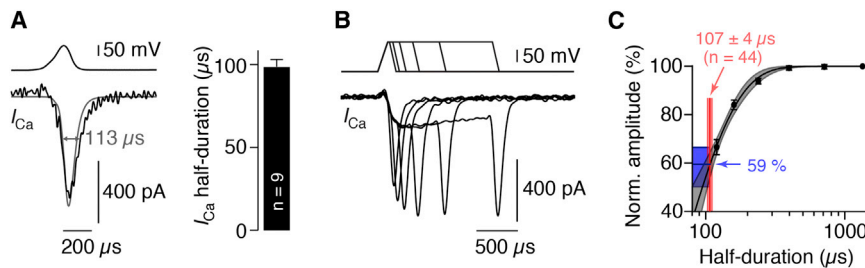


**Figure 5. Efficient Opening of  $\text{Ca}^{2+}$  Channels during cMFB APs**

(A) Left: Pharmacologically isolated  $\text{Ca}^{2+}$  current ( $I_{\text{Ca}}$ , bottom) evoked by an AP voltage command recorded in a cMFB (top) superimposed with the prediction of a  $m^2$  Hodgkin-Huxley model calculated with the AP-voltage command. The half-duration of the measured current is indicated. Right: Average half-duration of the measured  $\text{Ca}^{2+}$  current (mean  $\pm$  SEM;  $n$  represents number of cMFBs).

(B) Pharmacologically isolated  $\text{Ca}^{2+}$  current evoked by AP-like voltage commands of different

half-durations (120, 160, 240, 400, 720, 1,360  $\mu\text{s}$ ).

(C) Peak amplitudes of  $\text{Ca}^{2+}$  currents evoked by AP-like voltage commands. Data (means  $\pm$  SEM,  $n = 10$ ) were normalized to the maximum value of each experiment and fit with a monoexponential function (black line). Superposition of the 95% confidence band of the fit (gray) with the average AP half-duration ( $104 \pm 7 \mu\text{s}$ ,  $n = 44$ ; red) results in an estimate of relative  $\text{Ca}^{2+}$  channel open probability during an AP of 59% with a range of 50%–66% (blue; see also Figure S4).

component ( $N_2$ ,  $p < 0.01$ , Mann-Whitney U test; Figure 8A), suggesting that these vesicles are remote from  $\text{Ca}^{2+}$  channels (Wadel et al., 2007) or that they have a lower intrinsic  $\text{Ca}^{2+}$  affinity (Lee et al., 2013; Wölfel et al., 2007). The slope of the linear part of the fits was not reduced with 5 mM EGTA ( $p = 0.11$ , Mann-Whitney U test; Figure 8A), indicating that EGTA does not block recruitment of vesicles to the release site. We further analyzed the kinetics of release with capacitance measurements. As with deconvolution techniques, two components of release and a linear vesicle recruitment rate were observed. The second release component was blocked by 5 mM EGTA, but the slope of the linear component was unaffected (Figure 8B; Table S1).

To relate these parameters to release evoked by AP trains, we recorded EPSCs in GCs elicited by extracellular stimulation of mossy fibers at 300 Hz (Figure 8C). We analyzed the number of release-ready vesicles and the vesicle recruitment rate by back-extrapolation of the cumulative EPSC amplitude (Figure 8D; Schneggenburger et al., 1999; Thanawala and Regehr, 2013). This analysis revealed  $13.7 \pm 3.4$  release-ready vesicles and a recruitment rate of  $469 \pm 150 \text{ s}^{-1}$  ( $n = 10$ ), consistent with previous estimates at this synapse (Saviane and Silver, 2006; Hallermann et al., 2010). Interestingly, the values are similar to  $N_1$  and  $s$  determined with prolonged depolarizations (cf. Figure 8A). This indicates that fast-releasing ( $N_1$ ) but not slow-releasing vesicles ( $N_2$ ) contribute to AP-evoked release (Sakaba, 2006) and that the maximal vesicle recruitment rate is similar during AP trains and prolonged presynaptic voltage steps. Furthermore, application of the membrane-permeable  $\text{Ca}^{2+}$  chelator EGTA-AM (100  $\mu\text{M}$ ) reduced the EPSC amplitude by 37% ( $p < 0.01$ , Wilcoxon signed-rank test; Figure 8C). Since 100  $\mu\text{M}$  EGTA-AM was continuously applied at physiological temperatures, the intracellular EGTA concentration could be much higher than 5 mM. Therefore, no conclusions about the coupling distance can be drawn from these experiments. In contrast, the rate of vesicle recruitment was not significantly changed upon EGTA-AM application ( $p = 0.77$ , Wilcoxon signed-rank test; Figure 8D), which is again consistent with the lack of effect of 5 mM EGTA on the vesicle recruitment rate during depolarizations (cf. Figure 8A). In order to relate the recruitment rate to the vesicles that contribute to AP-evoked release, we divided the recruitment rate by the number of fast-releasing vesicles that mediate AP-evoked release. This resulted in a

recruitment rate of  $24 \text{ s}^{-1}$  with prolonged depolarization using deconvolution,  $50 \text{ s}^{-1}$  with prolonged depolarization using capacitance measurements, and  $34 \text{ s}^{-1}$  with train stimulation using back-extrapolation (Table S1). Thus, deconvolution technique, capacitance measurements, and train stimulation revealed a small pool of release-ready vesicles, containing vesicles tightly coupled to  $\text{Ca}^{2+}$  channels, and rapid vesicle recruitment that can be sustained for  $> 100 \text{ ms}$ .

## DISCUSSION

In this study, paired recordings between cMFBs and GC allowed us to analyze the mechanisms of high-frequency signaling at highly divergent presynaptic boutons transmitting onto dozens of postsynaptic partners (Jörntell and Ekerot, 2006; Rancz et al., 2007; Saviane and Silver, 2006). We identified a unique set of presynaptic properties enabling single cMFB-GC connections to sustain kHz transmission during short bursts of APs: ultrafast, metabolically efficient APs can occur at bursts of up to 1.5 kHz,  $\text{Ca}_v2.1$   $\text{Ca}^{2+}$  channels open efficiently during APs, a subset of vesicles is tightly coupled to  $\text{Ca}^{2+}$  channels, and vesicles are rapidly recruited to the release site. Thus, our results establish a set of parameters enabling central synapses to operate in the kHz range.

### Ultrafast APs

The AP is the basal unit for neuronal information processing, and its duration represents an ultimate limit for the maximal firing frequency. We recorded APs in cMFBs with  $\sim 100 \mu\text{s}$  half-duration (Figure 2). All previously measured AP half-durations are at least 2-fold longer. This is surprising because the AP shape has been studied extensively at a large number of cell types, including cells that transmit high-frequency signals (Borst and Sakmann, 1998; Rancz et al., 2007; Sabatini and Regehr, 1996). At cMFBs, previous estimates of AP half-duration in rats at physiological temperature (Rancz et al., 2007) and in turtles at room temperature (Thomsen et al., 2010) were several-fold longer; however, species differences and different recording conditions may account for this discrepancy. Yet extracellular recordings from cats in vivo are consistent with 100  $\mu\text{s}$  half-durations of APs in cMFBs (Garwicz et al., 1998). Furthermore, a half-duration of  $\sim 100 \mu\text{s}$  is expected for the mature calyx of Held at physiological



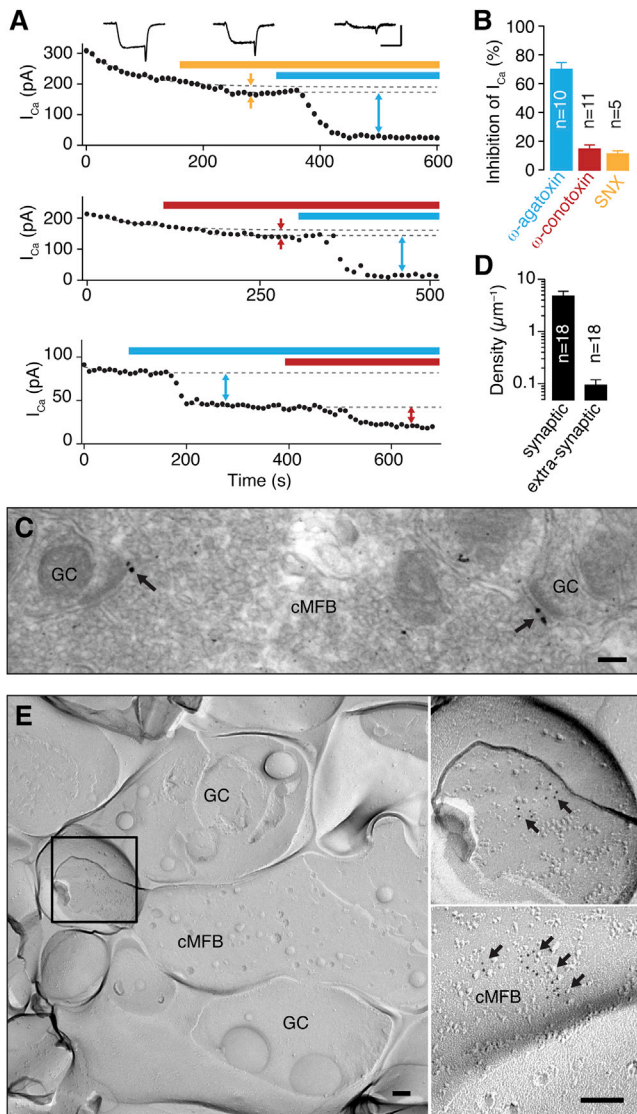


**Figure 6.  $Ca_v2.1$   $Ca^{2+}$  Channels at Active Zones of cMFBs**

(A) Steady-state amplitude of  $Ca^{2+}$  currents evoked by 3 ms depolarizations to 0 mV before and during application of 0.5  $\mu M$  SNX-482 and 0.5  $\mu M$   $\omega$ -Agatoxin (top), 1  $\mu M$   $\omega$ -Conotoxin and 0.5  $\mu M$   $\omega$ -Agatoxin (middle), or 0.5  $\mu M$   $\omega$ -Agatoxin and 1  $\mu M$   $\omega$ -Conotoxin (bottom). Horizontal bars indicate time of toxin application and dashed lines represent single exponential fits to the initial part of  $Ca^{2+}$  current amplitudes to account for rundown. Inset: Example  $Ca^{2+}$  currents for the first shown experiment before (left trace) and after wash-in of the toxins (middle and right traces). Scale bars, 200 pA and 2 ms.

(B) Average inhibition of  $Ca^{2+}$  currents by 0.5  $\mu M$   $\omega$ -Agatoxin, 1  $\mu M$   $\omega$ -Conotoxin, and 0.5  $\mu M$  SNX-482 (mean  $\pm$  SEM).

(C) Pre-embedding immunogold electron-microscopic labeling showing localization of  $Ca_v2.1$   $Ca^{2+}$  channels in the presynaptic active zones of a cMFB from a wild-type mouse. GC, granule cell dendrite. Arrows point toward gold particles. Scale bar, 100 nm.

(D) Average  $Ca_v2.1$  immunogold density in cMFB profiles within and outside the active zones on a logarithmic scale (mean  $\pm$  SEM).

(E) Freeze-fracture replica electron micrograph showing clusters of  $Ca_v2.1$   $Ca^{2+}$  channels in cMFBs from a 3-week-old mouse. Left: Low-magnification electron micrograph showing cross-fracture of a mossy fiber terminal (cMFB) with vesicles and continuous P-face of the same terminal contacting a granule

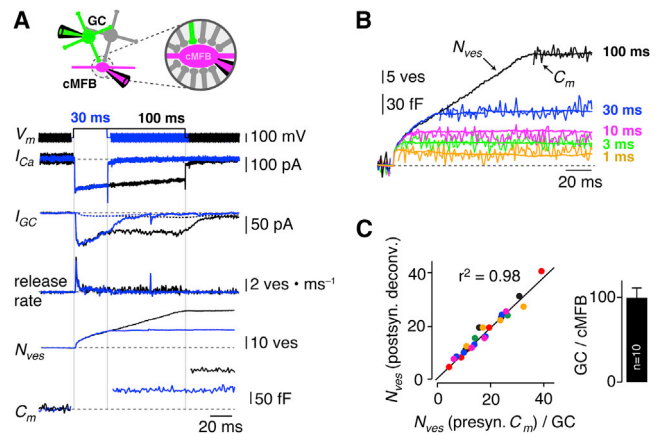


**Figure 7. Measuring Vesicular Release Simultaneously from Presynaptic Capacitance Increase and Postsynaptic Currents**

(A) Top: Illustration of the paired cMFB-GC recording configuration. The inset highlights the divergence of each cMFB contacting the GC recorded from (green) as well as many other GCs' dendrites (gray). Below: Example voltage command for cMFB ( $V_m$ ),  $Ca^{2+}$  current in cMFB ( $I_{Ca}$ ), EPSC in the GC ( $I_{GC}$ ), deconvolved release rate, cumulative release rate ( $N_{ves}$ ), and the capacitance increase in the cMFB ( $C_m$ ) are plotted for a 30 ms (blue) and 100 ms (black) cMFB depolarization.

(B) Superposition of capacitance increase ( $C_m$ ) in cMFB and cumulative release rate ( $N_{ves}$ ) estimated by deconvolution of the postsynaptic GC EPSC for different pulse durations as indicated for the example experiment shown in (A).

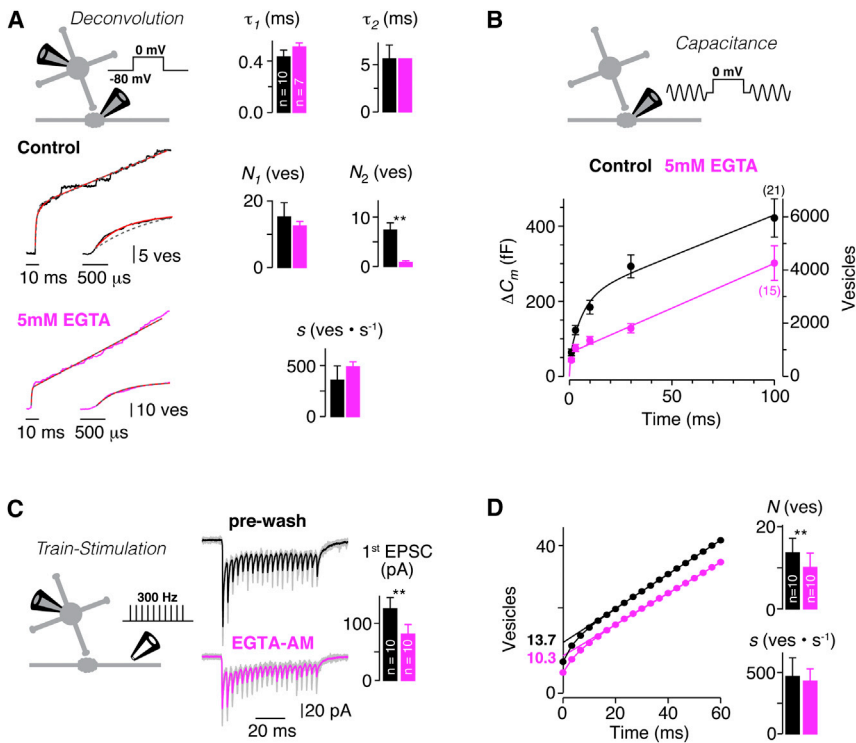
(C) Left: Comparison of the presynaptic ( $C_m$ ) and postsynaptic (deconvolution) estimates of the number of released vesicles per MF-GC connection. Each color represents a paired cMFB-GC recording with duration of depolarizations ranging from 1 to 100 ms. Right: Resulting average number of GC per cMFB based on  $n = 10$  paired recordings (mean  $\pm$  SEM).

temperature (Taschenberger and von Gersdorff, 2000), although such recordings have not been performed, and previously measured values at the immature calyx or at room temperatures were  $> 200 \mu s$  (Borst and Sakmann, 1998; Taschenberger and von Gersdorff, 2000; Yang and Wang, 2006). In general, fast-spiking neurons seem to have APs with short duration (Carter and Bean, 2009). Accordingly, maximal firing frequency and AP half-duration were correlated within the here-analyzed population of cMFBs (Figure 4C). Similar results have been obtained at two classes of vestibular nucleus neurons (Gittis et al., 2010). The very short half-duration of APs in cMFBs likely represents a special adaptation to the high frequencies that these presynaptic terminals operate at (Figure 4; Rancz et al., 2007).

To get an insight into the underlying mechanisms, we analyzed the properties of  $Na^+$  and  $K^+$  channels. Our estimated  $Na^+$  current density was similar to the density at axons of hippocampal interneurons (Hu and Jonas, 2014). Furthermore,  $Na^+$  channels were rapidly inactivating, resulting in a  $Na^+$  excess ratio of  $\sim 1.8$  (Figure 3), which is similar to the axon initial segment of layer 5 pyramidal cells (Hallermann et al., 2012) and slightly larger

cell dendrite (GC). A square part is enlarged (upper right) to show nine particles for  $Ca_v2.1$  clustered at the active zone. Lower right: The picture derives from a different cMFB showing 17 particles. Arrows point toward gold particles. Scale bars, 100 nm.





(D) Left: Average cumulative number of released vesicles before (black) and after application of EGTA-AM (magenta). The estimated number of release-ready vesicles by back-extrapolation is indicated. Right: Average number of release-ready vesicles ( $N$ ) and slope ( $s$ ) estimated from the back-extrapolation of individual experiments before and after application of EGTA-AM (mean  $\pm$  SEM; see also Table S1).

than at hippocampal mossy fiber boutons (Alle et al., 2009). The AP efficiency is surprising because short half-durations of APs tend to come at a cost of metabolic inefficiency (Carter and Bean, 2009, 2011).

The repolarization of cMFB APs was mediated by both  $K_{v1}$  and  $K_{v3}$  channels (Figure 2). This is in contrast to findings at the Purkinje cell soma, the boutons of cerebellar interneuron axons, or the calyx of Held, where  $K_{v3}$  dominates the repolarization (Ishikawa et al., 2003; Martina et al., 2007; Rowan et al., 2014; Wang et al., 1998). However, both  $K_{v1}$  and  $K_{v3}$  channels cause the repolarization of hippocampal mossy fiber boutons (Alle et al., 2011). The speed of  $K^+$  channel activation measured here at cMFBs was fast, but comparable to  $K^+$  channel activation kinetics measured previously (Alle et al., 2011; Martina et al., 2007), indicating that the ultrafast APs at cMFBs cannot be explained by rapid activation kinetics alone. Indeed, our Hodgkin-Huxley modeling based on measured gating kinetics predicted a high density of  $K^+$  channels at cMFBs (Figure S3). However, in most outside-out patches from cMFBs, the estimated  $K^+$  current density was low. This discrepancy is consistent with electron microscopic analysis showing that  $K_{v1}$  channels are highly clustered at fine protuberances of cMFBs, making density estimates from outside-out patches unreliable (Figure S3E; McNamara et al., 1996). In addition, cMFBs and the adjacent myelinated axons have structural similarities with nodes of Ranvier (Palay and Chan-Palay, 1974), suggesting that  $K^+$  channels are clustered at the adjacent mossy fiber

### Figure 8. Ultrafast Vesicle Recruitment and Tight $Ca^{2+}$ Channel-Vesicle Coupling

(A) Left: Example of cumulative release rates during a 100 ms depolarization in control (black; presynaptic pipette contained 200  $\mu$ M EGTA) and with increased  $Ca^{2+}$  buffering in the cMFB (magenta; 5 mM EGTA) superimposed with a fit consisting of the sum of a biexponential function and a line (red) and the sum of a monoexponential function and a line (dashed gray). Inset: Initial cumulative release rate on an expanded timescale. Right: Average fit parameters of the sum of a biexponential function and a line for control (black) and high-EGTA conditions (magenta; mean  $\pm$  SEM;  $n$  represents the number of paired cMFB-GC recordings). For 5 mM EGTA,  $\tau_2$  was fixed to the control value.

(B) Average capacitance increases ( $\Delta C_m$ ) plotted versus the length of the depolarizing pulse in control condition (black;  $n = 21$ ) and with 5 mM EGTA (magenta; mean  $\pm$  SEM;  $n = 15$ ;  $n$  represents the number of cMFB recordings). The right axis indicates the number of vesicles based on 70 aF/vesicle. See Table S1 for parameters of the fits.

(C) Left: Example EPSCs (gray) evoked by 300 Hz axonal stimulation (20 stimuli; recording configuration depicted by the inset) recorded in a cMFB superimposed with the corresponding average before (black) and after bath application of 100  $\mu$ M EGTA-AM (magenta). Right: Average amplitude of the first EPSC for control and EGTA-AM (black and magenta, respectively; mean  $\pm$  SEM;  $n = 10$ ).

axon comparable to the  $K^+$  channel clustering observed at juxtaparanodal zones of the nodes of Ranvier (Rasband and Shrager, 2000). Thus, although we have no direct experimental evidence, our results suggest a high density of inhomogeneously distributed  $K^+$  channels. Furthermore, our data indicate a high density of rapidly gating  $Na^+$  channels underlying ultrafast but metabolically efficient APs at cMFBs.

### Presynaptic $Ca^{2+}$ Currents

The exceptionally short duration of cMFB APs raised the question how  $Ca^{2+}$  channels are recruited during APs. In principle, reliable synaptic transmission can be obtained either by efficient opening of few presynaptic  $Ca^{2+}$  channels during APs (as shown, e.g., at the calyx of Held; Borst and Sakmann, 1998; but see also Sheng et al., 2012) or by inefficient opening of many  $Ca^{2+}$  channels (as shown, e.g., at the neuromuscular junction; Luo et al., 2011). Our analysis indicates efficient  $Ca^{2+}$  channel opening despite the short duration of APs (Figure 5). This implies that activation kinetics of  $Ca^{2+}$  channels is very fast. Indeed, experiments with step-like depolarizations revealed activation kinetics of  $< 100 \mu$ s at 0 mV (Figure S4). This is more than 5-fold faster than previous estimates at central synapses at room temperature (Borst and Sakmann, 1998; Li et al., 2007; Lin et al., 2011) and is consistent with a strong temperature dependence of  $Ca^{2+}$  channel kinetics (Sabatini and Regehr, 1996). Furthermore, a Hodgkin-Huxley-type model of  $Ca^{2+}$  channels based on the measured activation and inactivation kinetics predicted efficient

channel opening. To gain insight into the molecular mechanism of fast  $\text{Ca}^{2+}$  channel gating, we determined the contribution of the different  $\text{Ca}^{2+}$  channel subtypes at cMFBs. Electrophysiological recordings showed that  $\text{Ca}_v2.1$   $\text{Ca}^{2+}$  channels contribute  $\sim 70\%$  of the total  $\text{Ca}^{2+}$  current in cMFBs (Figure 6B). Furthermore, pre-embedding immunogold and freeze-fracture replica labeling indicated clustering of  $\text{Ca}_v2.1$   $\text{Ca}^{2+}$  channels at the active zone (Figures 6C and 6D). Thus, rapidly activating  $\text{Ca}_v2.1$   $\text{Ca}^{2+}$  channels ensure efficient calcium influx at the active zone during fast cMFB APs.

### Tight Vesicle to $\text{Ca}^{2+}$ Channel Coupling

The first component of release was not significantly slowed by 5 mM EGTA in cMFB (Figure 8A). In contrast, at the immature calyx of Held synapse, 5 mM EGTA prolonged the first component of release (Sakaba and Neher, 2001a). Thus, compared with loose vesicle to  $\text{Ca}^{2+}$  channel coupling at the immature calyx (Meinrenken et al., 2002), the mature cMFBs studied here display tight vesicle to  $\text{Ca}^{2+}$  channel coupling. Tight coupling has been observed at many synapses mediating high frequency synaptic transmission, such as the mature calyx of Held (Wang et al., 2008), the hippocampal basket cell to granule cell synapse (Bucurenciu et al., 2008), and the parallel fiber to Purkinje cell synapse (Schmidt et al., 2013). On the other hand, the mature hippocampal mossy fiber to CA3 pyramidal cell synapse exhibits loose coupling (Vyleta and Jonas, 2014). The tight and loose vesicle to  $\text{Ca}^{2+}$  channel coupling in cerebellar and hippocampal mossy fiber boutons, respectively, seems consistent with their markedly different function within the corresponding neuronal network (Delvendahl et al., 2013).

### Vesicle Recruitment Rate

We found a vesicle recruitment rate of  $\sim 400$  vesicles  $\cdot$  s $^{-1}$  during 100 ms depolarizations and during high-frequency synaptic transmission for each cMFB-GC connection at physiological temperatures (Figure 8). For the entire cMFB, the rate was 30,000 vesicles  $\cdot$  s $^{-1}$  (Figure 8B). At the calyx of Held synapse, at which vesicle recruitment has been intensely studied, a value of less than 10,000 vesicles  $\cdot$  s $^{-1}$  has been estimated at room temperature (Neher, 2010; Sakaba and Neher, 2001b; Wölfel et al., 2007), but higher values have also been obtained (100,000 and 170,000 vesicles  $\cdot$  s $^{-1}$ , at room and physiological temperatures; based on 7,500 and 12,300 fF/s, respectively; Kushmerick et al., 2006). Relating the vesicle recruitment rate to the number of fast-releasing vesicles in cMFBs resulted in estimates ranging from 24 to 50 s $^{-1}$  (Figure 8). This is lower than previous estimates based on postsynaptic techniques at cMFBs ( $\sim 70$  s $^{-1}$ ; Saviane and Silver, 2006; Hallermann et al., 2010), but higher than estimates at the calyx of Held ( $\sim 11$  s $^{-1}$ ; physiological temperature; Kushmerick et al., 2006). High rates of vesicle recruitment have also been observed at cerebellar parallel fibers (Crowley et al., 2007; Valera et al., 2012; but see van Beugen et al., 2013). Thus, vesicle recruitment at cMFBs is remarkably fast.

### Limited Surface Area at a Highly Divergent Synapse

One obvious explanation for the high vesicle recruitment rate in cMFBs could reside in the fact that each cMFB contacts more

than 10 dendrites of GCs (Billings et al., 2014; Jakab and Hámori, 1988; Figure 7C). This limits the surface area that is available for each postsynaptic partner. The limited number of release sites must therefore rely on rapid vesicle recruitment (Saviane and Silver, 2006). Consistently, the cMFB-GC synapse has been described as a “device to secure a high mossy fiber to GC divergence with minimal physical structure” (Eccles et al., 1967). In contrast, large synapses with 1:1 connectivity, such as the neuromuscular junction (Luo et al., 2011), the Purkinje cell to cerebellar nuclear neuron synapse (Telgkamp et al., 2004), the hippocampal mossy fiber to CA3 pyramidal neuron synapse (Hallermann et al., 2003), the vestibular afferent synapse (Bagnall et al., 2008), and the endbulb of Held synapse (Lin et al., 2011), rely on a large pool of release-ready vesicles with low release probabilities. Therefore, these 1:1 synapses can sustain efficient release by the parallel usage of many release sites despite slow vesicle recruitment at each site, whereas cMFB-GC synapses sustain efficient release with fewer release sites and rapid vesicle recruitment (cf. Box 1 in Hallermann and Silver, 2013). Thus, the limited space for synaptic contact at the cMFB-GC synapse might provide an explanation for the rapid vesicle recruitment.

### Implications for Information Processing

To control timing (Ivry and Keele, 1989), the cerebellar cortex relies on high-frequency firing of mossy fibers (Garwicz et al., 1998; Rancz et al., 2007), granule cells (Jörntell and Ekerot, 2006), and Purkinje cells (Blot and Barbour, 2014; Thach, 1972). Quantitative comparison of these data suggests that the frequency of a signal is highest in mossy fibers and gradually becomes lower during propagation through granule and Purkinje cells. Interestingly, GCs may linearly encode the strength of cMFB firing (Chadderton et al., 2004; Gabbiani et al., 1994). Linear processing also occurs at parallel fiber to Purkinje cell transmission, but in a lower frequency range (Walter and Khodakhah, 2006). The frequency reduction and the linear processing suggest that the cerebellar cortex receives mossy fiber input in the kHz range (Rancz et al., 2007; Figure 4), performs additive and (via gain modulation) multiplicative scaling of rate-coded inputs (Silver, 2010), and provides an output at frequencies still high but lower than the input. Thereby, computation at exceptionally fast timescales can be achieved. Future studies will have to analyze the advantages of high-frequency firing of individual neurons, in particular in consideration of the fact that other brain regions, such as the visual system, can process information rapidly, even though the firing rates of the individual neurons are much lower (Rieke et al., 1997; Tchumatchenko et al., 2011).

In summary, by using paired recordings between cMFBs and GCs in combination with high-resolution techniques, we were able to directly measure fundamental parameters that enable high-frequency synaptic transmission. Our study provides insight into the exceptionally diverse repertoire of synaptic functions at central synapses.

### EXPERIMENTAL PROCEDURES

Methods are described in detail in the [Supplemental Experimental Procedures](#).

**Presynaptic Recordings from cMFBs**

Recordings were performed in acute sagittal cerebellar slices from mature (>P20) TgN(Thy1-EYFP) (Hirrlinger et al., 2005) or C57BL/6 mice at 35°C – 37°C. To increase the success rate of presynaptic recordings from cMFBs, two-photon guided patch-clamp recordings (Margrie et al., 2003) were performed in the TgN(Thy1-EYFP)-mice with a Femto-2D two-photon microscope (Femtonics, Budapest) and a 60x Olympus (NA 1.0) objective. Alternatively, cMFBs were identified with infrared differential interference contrast (DIC) optics using a FN-1 microscope from Nikon with a 100x objective (NA 1.1). All current-clamp and voltage-clamp recordings from cMFBs and GCs were performed with an EPC10/2 amplifier (HEKA Elektronik, Lambrecht/Pfalz).

**Identification of cMFB Recordings**

To unequivocally identify cMFBs, two alternative methods were used: (1) in presynaptic recordings with potassium-based intracellular solutions, the distinctive electrical properties including pronounced outward rectification and time-dependent “sag” of membrane potential on hyperpolarization were used (Rancz et al., 2007); (2) in presynaptic recordings with cesium-based intracellular solutions (and TTX in the bath), the capacitance increase upon depolarization confirmed the identity of cMFBs, since other cells such as GCs did not show capacitance increases (if any, < 20 fF). In addition, Atto 594 in the presynaptic intracellular solution allowed visualizing the mossy fiber axon.

**Paired Recordings between cMFBs and GC**

For paired pre- and postsynaptic recordings, GCs were whole-cell patch-clamped with intracellular solution containing 100 μM Atto 594 or Atto 488, and cMFBs near dendrites were identified by their EYFP expression in TgN(Thy1-EYFP) mice or by differential interference contrast microscopy. The reliable induction of an EPSC in the GC upon depolarization of the presynaptic structure was used to unequivocally identify a cMFB.

**SUPPLEMENTAL INFORMATION**

Supplemental Information includes Supplemental Experimental Procedures, four figures, and one table and can be found with this article online at <http://dx.doi.org/10.1016/j.neuron.2014.08.036>.

**ACKNOWLEDGMENTS**

We would like to thank Erwin Neher for helpful discussions and for advice during the implementation of the deconvolution of postsynaptic currents; Erwin Neher, Maarten Kole, and Manfred Heckmann for critically reading the manuscript; Masahiko Watanabe for providing Ca<sub>v</sub>2.1 antibody; and Walter Kaufmann for technical assistance. This work was supported by the Heisenberg Program of the German Research Foundation to S.H. (HA 6386/1-1, 2-1, and 3-1) and by the German Research Foundation to J.H. (HI1414/2-1) and partly funded by the Wellcome Trust (ref: 097829) through the Centre for Chronic Diseases and Disorders (C2D2) at the University of York.

Accepted: August 17, 2014

Published: September 11, 2014

**REFERENCES**

Alle, H., Roth, A., and Geiger, J.R.P. (2009). Energy-efficient action potentials in hippocampal mossy fibers. *Science* 325, 1405–1408.

Alle, H., Kubota, H., and Geiger, J.R. (2011). Sparse but highly efficient K<sub>v</sub>3 outpace BK<sub>Ca</sub> channels in action potential repolarization at hippocampal mossy fiber boutons. *J. Neurosci.* 31, 8001–8012.

Arenz, A., Silver, R.A., Schaefer, A.T., and Margrie, T.W. (2008). The contribution of single synapses to sensory representation in vivo. *Science* 321, 977–980.

Bagnall, M.W., McElvain, L.E., Faulstich, M., and du Lac, S. (2008). Frequency-independent synaptic transmission supports a linear vestibular behavior. *Neuron* 60, 343–352.

Bean, B.P. (2007). The action potential in mammalian central neurons. *Nat. Rev. Neurosci.* 8, 451–465.

Billings, G., Piasini, E., Lőrincz, A., Nusser, Z., and Silver, R.A. (2014). Network structure within the cerebellar input layer enables lossless sparse encoding. *Neuron* 83, 960–974.

Blot, A., and Barbour, B. (2014). Ultra-rapid axon-axon ephaptic inhibition of cerebellar Purkinje cells by the pinceau. *Nat. Neurosci.* 17, 289–295.

Borst, J.G., and Sakmann, B. (1998). Calcium current during a single action potential in a large presynaptic terminal of the rat brainstem. *J. Physiol.* 506, 143–157.

Borst, J.G., and Soria van Hoeve, J. (2012). The calyx of held synapse: from model synapse to auditory relay. *Annu. Rev. Physiol.* 74, 199–224.

Bucurenciu, I., Kulić, A., Schwaller, B., Frotscher, M., and Jonas, P. (2008). Nanodomain coupling between Ca<sup>2+</sup> channels and Ca<sup>2+</sup> sensors promotes fast and efficient transmitter release at a cortical GABAergic synapse. *Neuron* 57, 536–545.

Carter, B.C., and Bean, B.P. (2009). Sodium entry during action potentials of mammalian neurons: incomplete inactivation and reduced metabolic efficiency in fast-spiking neurons. *Neuron* 64, 898–909.

Carter, B.C., and Bean, B.P. (2011). Incomplete inactivation and rapid recovery of voltage-dependent sodium channels during high-frequency firing in cerebellar Purkinje neurons. *J. Neurophysiol.* 105, 860–871.

Chadderton, P., Margrie, T.W., and Häusser, M. (2004). Integration of quanta in cerebellar granule cells during sensory processing. *Nature* 428, 856–860.

Crowley, J.J., Carter, A.G., and Regehr, W.G. (2007). Fast vesicle replenishment and rapid recovery from desensitization at a single synaptic release site. *J. Neurosci.* 27, 5448–5460.

Delvendahl, I., Weyhersmüller, A., Ritzau-Jost, A., and Hallermann, S. (2013). Hippocampal and cerebellar mossy fibre boutons – same name, different function. *J. Physiol.* 591, 3179–3188.

DiGregorio, D.A., Nusser, Z., and Silver, R.A. (2002). Spillover of glutamate onto synaptic AMPA receptors enhances fast transmission at a cerebellar synapse. *Neuron* 35, 521–533.

Eccles, J.C., Ito, M., and Szentagothai, J. (1967). *The Cerebellum as a Neuronal Machine*. (Berlin: Springer-Verlag).

Gabbiani, F., Midtgaard, J., and Knöpfel, T. (1994). Synaptic integration in a model of cerebellar granule cells. *J. Neurophysiol.* 72, 999–1009.

Garwicz, M., Jörntell, H., and Ekerot, C.F. (1998). Cutaneous receptive fields and topography of mossy fibres and climbing fibres projecting to cat cerebellar C3 zone. *J. Physiol.* 512, 277–293.

Geiger, J.R.P., and Jonas, P. (2000). Dynamic control of presynaptic Ca<sup>2+</sup> inflow by fast-inactivating K<sup>+</sup> channels in hippocampal mossy fiber boutons. *Neuron* 28, 927–939.

Gittis, A.H., Moghadam, S.H., and du Lac, S. (2010). Mechanisms of sustained high firing rates in two classes of vestibular nucleus neurons: differential contributions of resurgent Na, Kv3, and BK currents. *J. Neurophysiol.* 104, 1625–1634.

Gutman, G.A., Chandy, K.G., Grissmer, S., Lazdunski, M., McKinnon, D., Pardo, L.A., Robertson, G.A., Rudy, B., Sanguinetti, M.C., Stühmer, W., and Wang, X. (2005). International Union of Pharmacology. LIII. Nomenclature and molecular relationships of voltage-gated potassium channels. *Pharmacol. Rev.* 57, 473–508.

Hallermann, S., and Silver, R.A. (2013). Sustaining rapid vesicular release at active zones: potential roles for vesicle tethering. *Trends Neurosci.* 36, 185–194.

Hallermann, S., Pawlu, C., Jonas, P., and Heckmann, M. (2003). A large pool of releasable vesicles in a cortical glutamatergic synapse. *Proc. Natl. Acad. Sci. USA* 100, 8975–8980.

Hallermann, S., Fejtova, A., Schmidt, H., Weyhersmüller, A., Silver, R.A., Gundelfinger, E.D., and Eilers, J. (2010). Bassoon speeds vesicle reloading at a central excitatory synapse. *Neuron* 68, 710–723.

- Hallermann, S., de Kock, C.P., Stuart, G.J., and Kole, M.H. (2012). State and location dependence of action potential metabolic cost in cortical pyramidal neurons. *Nat. Neurosci.* *15*, 1007–1014.
- Hirrlinger, P.G., Scheller, A., Braun, C., Quintela-Schneider, M., Fuss, B., Hirrlinger, J., and Kirchhoff, F. (2005). Expression of reef coral fluorescent proteins in the central nervous system of transgenic mice. *Mol. Cell. Neurosci.* *30*, 291–303.
- Hu, H., and Jonas, P. (2014). A supercritical density of Na<sup>+</sup> channels ensures fast signaling in GABAergic interneuron axons. *Nat. Neurosci.* *17*, 686–693.
- Indriati, D.W., Kamasawa, N., Matsui, K., Meredith, A.L., Watanabe, M., and Shigemoto, R. (2013). Quantitative localization of Ca<sub>v</sub>2.1 (P/Q-type) voltage-dependent calcium channels in Purkinje cells: somatodendritic gradient and distinct somatic coclustering with calcium-activated potassium channels. *J. Neurosci.* *33*, 3668–3678.
- Ishikawa, T., Nakamura, Y., Saitoh, N., Li, W.B., Iwasaki, S., and Takahashi, T. (2003). Distinct roles of Kv1 and Kv3 potassium channels at the calyx of Held presynaptic terminal. *J. Neurosci.* *23*, 10445–10453.
- Ivry, R.B., and Keele, S.W. (1989). Timing functions of the cerebellum. *J. Cogn. Neurosci.* *1*, 136–152.
- Jakab, R.L., and Háromi, J. (1988). Quantitative morphology and synaptology of cerebellar glomeruli in the rat. *Anat. Embryol. (Berl.)* *179*, 81–88.
- Jöntell, H., and Ekerot, C.F. (2006). Properties of somatosensory synaptic integration in cerebellar granule cells *in vivo*. *J. Neurosci.* *26*, 11786–11797.
- Kushmerick, C., Renden, R., and von Gersdorff, H. (2006). Physiological temperatures reduce the rate of vesicle pool depletion and short-term depression via an acceleration of vesicle recruitment. *J. Neurosci.* *26*, 1366–1377.
- Leão, R.M., Kushmerick, C., Pinaud, R., Renden, R., Li, G.L., Taschenberger, H., Spirou, G., Levinson, S.R., and von Gersdorff, H. (2005). Presynaptic Na<sup>+</sup> channels: locus, development, and recovery from inactivation at a high-fidelity synapse. *J. Neurosci.* *25*, 3724–3738.
- Lee, J.S., Ho, W.K., Neher, E., and Lee, S.H. (2013). Superpriming of synaptic vesicles after their recruitment to the readily releasable pool. *Proc. Natl. Acad. Sci. USA* *110*, 15079–15084.
- Li, L., Bischofberger, J., and Jonas, P. (2007). Differential gating and recruitment of P/Q-, N-, and R-type Ca<sup>2+</sup> channels in hippocampal mossy fiber boutons. *J. Neurosci.* *27*, 13420–13429.
- Lien, C.C., and Jonas, P. (2003). Kv3 potassium conductance is necessary and kinetically optimized for high-frequency action potential generation in hippocampal interneurons. *J. Neurosci.* *23*, 2058–2068.
- Lin, K.H., Oleskevich, S., and Taschenberger, H. (2011). Presynaptic Ca<sup>2+</sup> influx and vesicle exocytosis at the mouse endbulb of Held: a comparison of two auditory nerve terminals. *J. Physiol.* *589*, 4301–4320.
- Liu, P.W., and Bean, B.P. (2014). Kv2 channel regulation of action potential repolarization and firing patterns in superior cervical ganglion neurons and hippocampal CA1 pyramidal neurons. *J. Neurosci.* *34*, 4991–5002.
- London, M., Roth, A., Beeren, L., Häusser, M., and Latham, P.E. (2010). Sensitivity to perturbations *in vivo* implies high noise and suggests rate coding in cortex. *Nature* *466*, 123–127.
- Luo, F., Dittrich, M., Stiles, J.R., and Meriney, S.D. (2011). Single-pixel optical fluctuation analysis of calcium channel function in active zones of motor nerve terminals. *J. Neurosci.* *31*, 11268–11281.
- Margrie, T.W., Meyer, A.H., Caputi, A., Monyer, H., Hasan, M.T., Schaefer, A.T., Denk, W., and Brecht, M. (2003). Targeted whole-cell recordings in the mammalian brain *in vivo*. *Neuron* *39*, 911–918.
- Martina, M., Metz, A.E., and Bean, B.P. (2007). Voltage-dependent potassium currents during fast spikes of rat cerebellar Purkinje neurons: inhibition by BDS-1 toxin. *J. Neurophysiol.* *97*, 563–571.
- McNamara, N.M., Averill, S., Wilkin, G.P., Dolly, J.O., and Priestley, J.V. (1996). Ultrastructural localization of a voltage-gated K<sup>+</sup> channel  $\alpha$  subunit (K<sub>v</sub> 1.2) in the rat cerebellum. *Eur. J. Neurosci.* *8*, 688–699.
- Meinrenken, C.J., Borst, J.G., and Sakmann, B. (2002). Calcium secretion coupling at calyx of held governed by nonuniform channel-vesicle topography. *J. Neurosci.* *22*, 1648–1667.
- Neher, E. (2010). What is rate-limiting during sustained synaptic activity: vesicle supply or the availability of release sites. *Front Synaptic Neurosci* *2*, 144, <http://dx.doi.org/10.3389/fnsyn.2010.00144>.
- Palay, S.M., and Chan-Palay, V. (1974). *Cerebellar Cortex: Cytology and Organization*. (Berlin: Springer).
- Rancz, E.A., Ishikawa, T., Duguid, I., Chadderton, P., Mahon, S., and Häusser, M. (2007). High-fidelity transmission of sensory information by single cerebellar mossy fibre boutons. *Nature* *450*, 1245–1248.
- Rasband, M.N., and Shrager, P. (2000). Ion channel sequestration in central nervous system axons. *J. Physiol.* *525*, 63–73.
- Rieke, F., Warland, D., de Ruyter van Steveninck, R.R., and Bialek, W. (1997). *Spikes: Exploring the Neural Code*. (Cambridge, Massachusetts: MIT Press).
- Rowan, M.J.M., Tranquill, E., and Christie, J.M. (2014). Distinct K<sub>v</sub> channel subtypes contribute to differences in spike signaling properties in the axon initial segment and presynaptic boutons of cerebellar interneurons. *J. Neurosci.* *34*, 6611–6623.
- Rudy, B., and McBain, C.J. (2001). Kv3 channels: voltage-gated K<sup>+</sup> channels designed for high-frequency repetitive firing. *Trends Neurosci.* *24*, 517–526.
- Sabatini, B.L., and Regehr, W.G. (1996). Timing of neurotransmission at fast synapses in the mammalian brain. *Nature* *384*, 170–172.
- Sakaba, T. (2006). Roles of the fast-releasing and the slowly releasing vesicles in synaptic transmission at the calyx of held. *J. Neurosci.* *26*, 5863–5871.
- Sakaba, T., and Neher, E. (2001a). Calmodulin mediates rapid recruitment of fast-releasing synaptic vesicles at a calyx-type synapse. *Neuron* *32*, 1119–1131.
- Sakaba, T., and Neher, E. (2001b). Quantitative relationship between transmitter release and calcium current at the calyx of held synapse. *J. Neurosci.* *21*, 462–476.
- Saviane, C., and Silver, R.A. (2006). Fast vesicle reloading and a large pool sustain high bandwidth transmission at a central synapse. *Nature* *439*, 983–987.
- Schmidt, H., Brachtendorf, S., Arendt, O., Hallermann, S., Ishiyama, S., Bornschein, G., Gall, D., Schiffmann, S.N., Heckmann, M., and Eilers, J. (2013). Nanodomain coupling at an excitatory cortical synapse. *Curr. Biol.* *23*, 244–249.
- Schneggenburger, R., Meyer, A.C., and Neher, E. (1999). Released fraction and total size of a pool of immediately available transmitter quanta at a calyx synapse. *Neuron* *23*, 399–409.
- Sheng, M., Tsaur, M.L., Jan, Y.N., and Jan, L.Y. (1992). Subcellular segregation of two A-type K<sup>+</sup> channel proteins in rat central neurons. *Neuron* *9*, 271–284.
- Sheng, J., He, L., Zheng, H., Xue, L., Luo, F., Shin, W., Sun, T., Kuner, T., Yue, D.T., and Wu, L.G. (2012). Calcium-channel number critically influences synaptic strength and plasticity at the active zone. *Nat. Neurosci.* *15*, 998–1006.
- Silver, R.A. (2010). Neuronal arithmetic. *Nat. Rev. Neurosci.* *11*, 474–489.
- Sun, J.Y., and Wu, L.G. (2001). Fast kinetics of exocytosis revealed by simultaneous measurements of presynaptic capacitance and postsynaptic currents at a central synapse. *Neuron* *30*, 171–182.
- Taschenberger, H., and von Gersdorff, H. (2000). Fine-tuning an auditory synapse for speed and fidelity: developmental changes in presynaptic waveform, EPSC kinetics, and synaptic plasticity. *J. Neurosci.* *20*, 9162–9173.
- Tchumatchenko, T., Malyshev, A., Wolf, F., and Volgushev, M. (2011). Ultrafast population encoding by cortical neurons. *J. Neurosci.* *31*, 12171–12179.
- Telgkamp, P., Padgett, D.E., Ledoux, V.A., Woolley, C.S., and Raman, I.M. (2004). Maintenance of high-frequency transmission at purkinje to cerebellar nuclear synapses by spillover from boutons with multiple release sites. *Neuron* *41*, 113–126.
- Thach, W.T. (1972). Cerebellar output: properties, synthesis and uses. *Brain Res.* *40*, 89–102.



- Thanawala, M.S., and Regehr, W.G. (2013). Presynaptic calcium influx controls neurotransmitter release in part by regulating the effective size of the readily releasable pool. *J. Neurosci.* *33*, 4625–4633.
- Thomsen, L.B., Jörtell, H., and Midtgaard, J. (2010). Presynaptic calcium signalling in cerebellar mossy fibres. *Front Neural Circuits* *4*, 1.
- Valera, A.M., Doussau, F., Poulain, B., Barbour, B., and Isope, P. (2012). Adaptation of granule cell to Purkinje cell synapses to high-frequency transmission. *J. Neurosci.* *32*, 3267–3280.
- van Beugen, B.J., Gao, Z., Boele, H.J., Hoebeek, F., and De Zeeuw, C.I. (2013). High frequency burst firing of granule cells ensures transmission at the parallel fiber to purkinje cell synapse at the cost of temporal coding. *Front Neural Circuits* *7*, 95.
- von Gersdorff, H., Sakaba, T., Berglund, K., and Tachibana, M. (1998). Submillisecond kinetics of glutamate release from a sensory synapse. *Neuron* *21*, 1177–1188.
- Vyleta, N.P., and Jonas, P. (2014). Loose coupling between  $\text{Ca}^{2+}$  channels and release sensors at a plastic hippocampal synapse. *Science* *343*, 665–670.
- Wadel, K., Neher, E., and Sakaba, T. (2007). The coupling between synaptic vesicles and  $\text{Ca}^{2+}$  channels determines fast neurotransmitter release. *Neuron* *53*, 563–575.
- Walter, J.T., and Khodakhah, K. (2006). The linear computational algorithm of cerebellar Purkinje cells. *J. Neurosci.* *26*, 12861–12872.
- Wang, L.Y., and Kaczmarek, L.K. (1998). High-frequency firing helps replenish the readily releasable pool of synaptic vesicles. *Nature* *394*, 384–388.
- Wang, L.Y., Gan, L., Forsythe, I.D., and Kaczmarek, L.K. (1998). Contribution of the Kv3.1 potassium channel to high-frequency firing in mouse auditory neurons. *J. Physiol.* *509*, 183–194.
- Wang, L.Y., Neher, E., and Taschenberger, H. (2008). Synaptic vesicles in mature calyx of Held synapses sense higher nanodomain calcium concentrations during action potential-evoked glutamate release. *J. Neurosci.* *28*, 14450–14458.
- Wölfel, M., Lou, X., and Schneggenburger, R. (2007). A mechanism intrinsic to the vesicle fusion machinery determines fast and slow transmitter release at a large CNS synapse. *J. Neurosci.* *27*, 3198–3210.
- Yang, Y.M., and Wang, L.Y. (2006). Amplitude and kinetics of action potential-evoked  $\text{Ca}^{2+}$  current and its efficacy in triggering transmitter release at the developing calyx of held synapse. *J. Neurosci.* *26*, 5698–5708.

**3.2 Delvendahl et al. 2015 Proc. Natl. Acad. Sci. USA 112,  
E3075–3084.**

Seite 27–36

# Reduced endogenous $\text{Ca}^{2+}$ buffering speeds active zone $\text{Ca}^{2+}$ signaling

 Igor Delvendahl<sup>a,1</sup>, Lukasz Jablonski<sup>a</sup>, Carolin Baade<sup>a</sup>, Victor Matveev<sup>b</sup>, Erwin Neher<sup>c,1</sup>, and Stefan Hallermann<sup>a,1</sup>
<sup>a</sup>Carl-Ludwig-Institute for Physiology, Medical Faculty, University of Leipzig, 04103 Leipzig, Germany; <sup>b</sup>Department of Mathematical Sciences, New Jersey Institute of Technology, Newark, NJ 07102; and <sup>c</sup>Max-Planck-Institute for Biophysical Chemistry, 37077 Göttingen, Germany

Contributed by Erwin Neher, April 30, 2015 (sent for review March 9, 2015; reviewed by Gary Matthews and Bert Sakmann)

**Fast synchronous neurotransmitter release at the presynaptic active zone is triggered by local  $\text{Ca}^{2+}$  signals, which are confined in their spatiotemporal extent by endogenous  $\text{Ca}^{2+}$  buffers. However, it remains elusive how rapid and reliable  $\text{Ca}^{2+}$  signaling can be sustained during repetitive release. Here, we established quantitative two-photon  $\text{Ca}^{2+}$  imaging in cerebellar mossy fiber boutons, which fire at exceptionally high rates. We show that endogenous fixed buffers have a surprisingly low  $\text{Ca}^{2+}$ -binding ratio ( $\sim 15$ ) and low affinity, whereas mobile buffers have high affinity. Experimentally constrained modeling revealed that the low endogenous buffering promotes fast clearance of  $\text{Ca}^{2+}$  from the active zone during repetitive firing. Measuring  $\text{Ca}^{2+}$  signals at different distances from active zones with ultra-high-resolution confirmed our model predictions. Our results lead to the concept that reduced  $\text{Ca}^{2+}$  buffering enables fast active zone  $\text{Ca}^{2+}$  signaling, suggesting that the strength of endogenous  $\text{Ca}^{2+}$  buffering limits the rate of synchronous synaptic transmission.**

active zone | calcium signaling | presynaptic | neurotransmitter release | calcium buffers

At presynaptic nerve terminals, the opening of voltage-gated  $\text{Ca}^{2+}$  channels during action potentials (APs) leads to a brief  $\text{Ca}^{2+}$  influx. The resulting microdomain  $\text{Ca}^{2+}$  signals reach several tens of micromolar amplitude near open  $\text{Ca}^{2+}$  channels and trigger neurotransmitter release at presynaptic active zones (1, 2). After  $\text{Ca}^{2+}$  channel closing, the binding to endogenous  $\text{Ca}^{2+}$  buffers and diffusion of  $\text{Ca}^{2+}$  within the cytosol lead to collapse of the microdomain, increasing the residual  $[\text{Ca}^{2+}]$  in the presynaptic terminal to not more than a fraction of micromolar. During this equilibration with  $\text{Ca}^{2+}$  buffers, the majority of entering  $\text{Ca}^{2+}$  ions are bound to endogenous  $\text{Ca}^{2+}$  buffers (3). The strength of intracellular  $\text{Ca}^{2+}$  buffering can be characterized by the  $\text{Ca}^{2+}$ -binding ratio defined as the ratio of buffer-bound  $\text{Ca}^{2+}$  to free  $\text{Ca}^{2+}$  (4). It is established that strong  $\text{Ca}^{2+}$  buffering limits the spread of  $\text{Ca}^{2+}$  ions at active zones and thus restricts neurotransmitter release to the vicinity of  $\text{Ca}^{2+}$  channels (5). Rapid removal of calcium from the active zone is essential to sustain synchronous release during repetitive activity. However, the mechanisms controlling the speed of active zone  $\text{Ca}^{2+}$  signaling during repetitive synaptic transmission and the clearance of  $\text{Ca}^{2+}$  from the active zone in between APs remain elusive.

The cerebellar mossy fiber bouton (cMFB) to granule cell synapse is ideally suited to analyze  $\text{Ca}^{2+}$  signaling during repetitive synaptic transmission because of the synchronous neurotransmitter release at exceptionally high frequencies (6–8). Understanding rapid active zone  $\text{Ca}^{2+}$  signaling requires knowledge about the  $\text{Ca}^{2+}$  dynamics and the strength, mobility, and binding kinetics of endogenous  $\text{Ca}^{2+}$  buffers. In particular, a dissection of fixed and mobile buffers (9, 10) is needed, which is technically challenging and requires access to the presynaptic terminal.

Here, we perform quantitative two-photon  $\text{Ca}^{2+}$  imaging in cMFBs, which are dialyzed with the pipette solution, and in remote cMFBs along the same axon, which are minimally perturbed, to separately characterize fixed and mobile  $\text{Ca}^{2+}$  buffers. We show that rapid active zone  $\text{Ca}^{2+}$  signaling is achieved by a

low  $\text{Ca}^{2+}$ -binding ratio of endogenous fixed buffers with low affinity and mobile buffers with high affinity. Our data explain how a central synapse achieves the speed of active zone  $\text{Ca}^{2+}$  signaling required for fast and synchronous transmitter release and suggest that the strength of endogenous  $\text{Ca}^{2+}$  buffering limits the precision and synchronicity of repetitive synaptic activity.

## Results

**Quantitative Two-Photon  $\text{Ca}^{2+}$  Imaging in cMFBs.** Quantitative knowledge about presynaptic  $\text{Ca}^{2+}$  dynamics is crucial to understanding the mechanisms of active zone  $\text{Ca}^{2+}$  signaling. Here, we combined direct patch-clamp recordings from en passant cMFBs (6, 8) (Fig. 1 *A–C*) with quantitative two-photon  $\text{Ca}^{2+}$  imaging. Single APs produced distinct and reproducible fluorescence transients (Fig. 1 *D–F*), consistent with previous measurements in mice and turtles (11, 12). Presynaptic recordings permit quantifying  $\text{Ca}^{2+}$  transients using a dual-indicator method (13) (Fig. 1*G*). For each combination of  $\text{Ca}^{2+}$ -sensitive (green) and  $\text{Ca}^{2+}$ -insensitive (red) dye, the signals were calibrated with presynaptic recordings by adding 10 mM EGTA or 10 mM  $\text{CaCl}_2$  to the intracellular solution (*Materials and Methods*). The  $\text{Ca}^{2+}$  concentration at rest ( $[\text{Ca}^{2+}]_{\text{rest}}$ ) was  $57 \pm 7$  nM in cMFBs based on recordings with the  $\text{Ca}^{2+}$  indicator OGB-1 ( $n = 30$ ; Fig. *S1B*), consistent with other presynaptic terminals (14–16). Establishing quantitative two-photon  $\text{Ca}^{2+}$  imaging in combination with in-cell calibration measurements at cMFBs (Figs. *S1* and *S2*) enabled us to analyze the  $\text{Ca}^{2+}$  dynamics at these presynaptic terminals in detail.

## Significance

**Calcium influx during action potentials triggers neurotransmitter release at presynaptic active zones. Calcium buffers limit the spread of calcium and restrict neurotransmitter release to the vicinity of calcium channels. To sustain synchronous release during repetitive activity, rapid removal of calcium from the active zone is essential, but the underlying mechanisms are unclear. Therefore, we focused on cerebellar mossy fiber synapses, which are among the fastest synapses in the mammalian brain and found very weak presynaptic calcium buffering. One might assume that strong calcium buffering has the potential to efficiently remove calcium from active zones. In contrast, our results show that weak calcium buffering speeds active zone calcium clearance. Thus, the strength of presynaptic buffering limits the rate of synaptic transmission.**

Author contributions: I.D., E.N., and S.H. designed research; I.D., L.J., and C.B. performed research; V.M. and E.N. contributed new reagents/analytic tools; I.D., L.J., V.M., E.N., and S.H. analyzed data; and I.D. and S.H. wrote the paper.

Reviewers: G.M., SUNY Stony Brook; and B.S., Max Planck Institut für Neurobiologie.

The authors declare no conflict of interest.

Freely available online through the PNAS open access option.

<sup>1</sup>To whom correspondence may be addressed. Email: igor.delvendahl@medizin.uni-leipzig.de, eneher@gwdg.de, or hallermann@medizin.uni-leipzig.de.

This article contains supporting information online at [www.pnas.org/lookup/suppl/doi:10.1073/pnas.1508419112/-DCSupplemental](http://www.pnas.org/lookup/suppl/doi:10.1073/pnas.1508419112/-DCSupplemental).

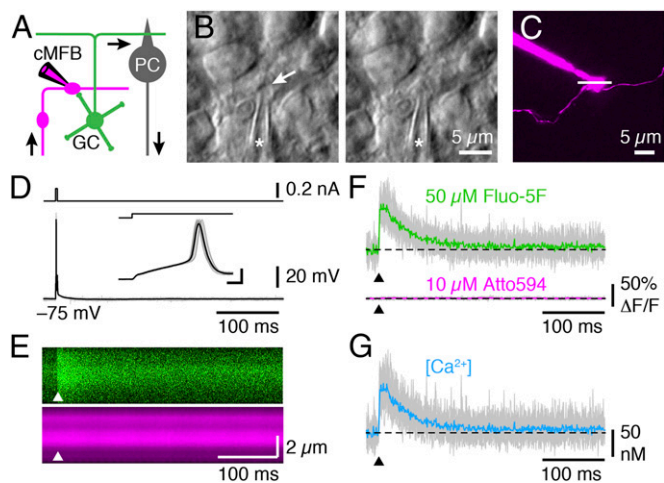


**Fig. 1.** Quantitative two-photon  $\text{Ca}^{2+}$  imaging in cMFBs. (A) Illustration of the cellular connectivity within cerebellar cortex. Mossy fibers (magenta) send information to the cerebellar cortex. Presynaptic cerebellar mossy fiber boutons (cMFBs) transmit signals to postsynaptic granule cells (GC, green), which excite Purkinje cells (PC, gray) via parallel fibers. Purkinje cell axons represent the sole output of the cerebellar cortex. Patch-clamp pipette illustrates presynaptic recording configuration. (B) (Left) Infrared image of a cMFB in an acute cerebellar slice during patch-clamp process. Arrow indicates membrane dimpling before seal formation. (Right) Same bouton after gaining whole-cell access. Asterisks indicate patch-pipette. (C) Two-photon image of a patched bouton filled with 10  $\mu\text{M}$  Atto594 and 50  $\mu\text{M}$  Fluo-5F (maximum z-projection of a stack of images over 45  $\mu\text{m}$ ; z-step, 2.5  $\mu\text{m}$ ). Line scan position is indicated. (D) cMFB APs elicited by current injection (200 pA, 3 ms). (Inset) APs on expanded time scale; superposition of 15 consecutive APs (gray) with average (black). (Scale bars, 200  $\mu\text{s}$  and 20 mV.) (E) Two-photon line scans for the green and red channel. Arrowheads denote time point of AP. (F) Change in fluorescence intensity within the cMFB ( $\Delta F/F$ ) for the green and red channel. Colored traces are averages of 15 sweeps (gray). (G) Corresponding calculated  $\text{Ca}^{2+}$  concentration.

**Low  $\text{Ca}^{2+}$ -Binding Ratio of Endogenous Fixed Buffers.** The  $\text{Ca}^{2+}$ -binding ratio of endogenous fixed buffers ( $\kappa_{E,\text{fixed}}$ ) can be estimated by loading a cellular compartment with various amounts of  $\text{Ca}^{2+}$  indicator dye (4, 17), as direct whole-cell recording from a small subcellular compartment leads to substantial wash-out of mobile  $\text{Ca}^{2+}$  buffers. We used  $\text{Ca}^{2+}$ -sensitive dyes of different affinities to measure  $\text{Ca}^{2+}$  transients evoked by single APs (Fig. 2A and B). Increasing the  $\text{Ca}^{2+}$ -binding ratio of the added  $\text{Ca}^{2+}$  indicator ( $\kappa_B$ ), which also acts as a  $\text{Ca}^{2+}$  buffer, reduced the amplitude and prolonged the decay of  $\text{Ca}^{2+}$  transients (Fig. 2A and B and Fig. S3A). According to the single compartment model, the inverse of the amplitude ( $A^{-1}$ ) and the decay time constant ( $\tau$ ) were linearly related to  $\kappa_B$  (4, 14) (Fig. 2C and D). Hence, the  $\text{Ca}^{2+}$  transient without added buffer was estimated by linear extrapolation, yielding amplitude of 204 nM and  $\tau$  of 50.3 ms. The  $\text{Ca}^{2+}$ -extrusion rate ( $\gamma$ ) was determined as  $267 \text{ s}^{-1}$  and  $\kappa_{E,\text{fixed}}$  as 17.1 and 12.5 from  $A^{-1}$  and  $\tau$  extrapolation, respectively, resulting in a mean estimate of  $\sim 15$  (Fig. 2C and D). The product of  $A$  and  $\tau$  was independent of  $\kappa_B$  (18) (Fig. 2E). Statistical reliability was addressed with a bootstrap method, resulting in  $\kappa_{E,\text{fixed}}$  of  $17.5 \pm 7.5$  and  $12.7 \pm 7.2$  from  $A^{-1}$  and  $\tau$  extrapolation, respectively (mean  $\pm$  SEM, corresponding to a 16–84% CI based on 152 experiments; *Materials and Methods* and Fig. S3B).

These results depend on correct quantification of presynaptic  $[\text{Ca}^{2+}]$ . To confirm that our two-photon imaging with dual-indicator calibration reliably estimates  $[\text{Ca}^{2+}]$ , we recorded  $\text{Ca}^{2+}$  transients in response to a single AP using the  $\text{Ca}^{2+}$  indicator Fura-2 and epifluorescence illumination with two alternating wavelengths ( $n = 12$ ; Fig. 2B). The amplitude and decay time constant were in close agreement to the measurements with two-

photon imaging (Fig. 2C and D). Furthermore, a single-indicator method applicable for high-affinity  $\text{Ca}^{2+}$  dyes (being independent of intrabouton calibration measurements) (19) yielded very similar amplitudes (Fig. S3A). Thus, these data demonstrate that at cMFBs the  $\text{Ca}^{2+}$ -binding ratio of endogenous fixed buffers is very low compared with other presynaptic terminals (14, 15, 20–22).

### $\text{Ca}^{2+}$ Transients in Remote Boutons Indicate Wash-Out of Mobile Buffers.

To analyze a potential wash-out of endogenous mobile buffers during presynaptic recordings, we measured  $\text{Ca}^{2+}$  transients in remote boutons along the mossy fiber axon of patched cMFBs (Fig. 3A). There,  $\text{Ca}^{2+}$  transients elicited by single APs became smaller in amplitude and decayed more slowly during dye loading (Fig. 3B). Intrabouton concentration and  $\text{Ca}^{2+}$ -binding ratio  $\kappa_B$  of Fluo-5F were calculated from the fluorescence intensity (Fig. 3C and D). For quantification of  $\text{Ca}^{2+}$  signals, we corrected for a faster loading of Atto594 compared with Fluo-5F (*Materials and Methods*). Linear extrapolation of  $A^{-1}$  and  $\tau$  vs.  $\kappa_B$  resulted in low and sometimes negative estimates of  $\kappa_{E,\text{fixed}}$  (Fig. 3E and F). These results indicate a wash-out of slow mobile  $\text{Ca}^{2+}$  buffers, because slow buffers speed the decay of  $\text{Ca}^{2+}$  transients and the initial presence of slow buffers consequently leads to an underestimation of  $\kappa_{E,\text{fixed}}$  (23). Indeed, simulating the wash-in of

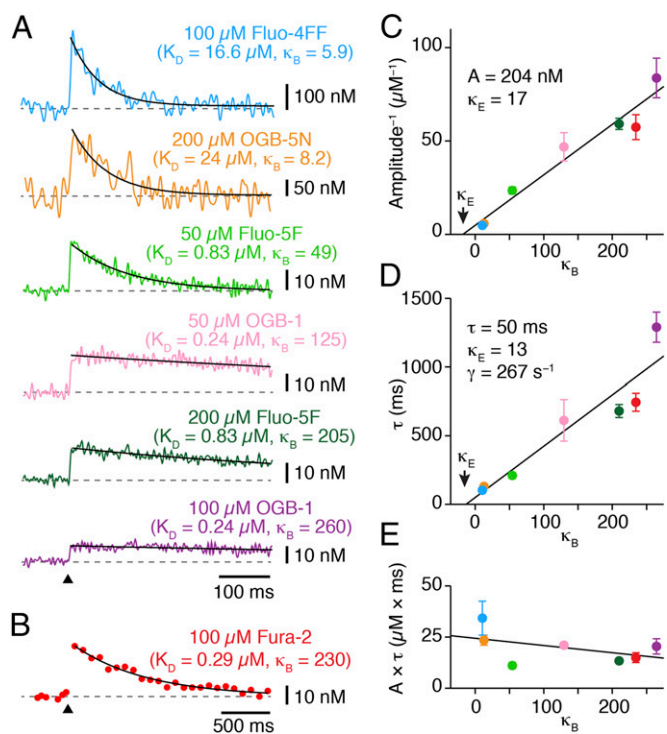


**Fig. 2.** Low  $\text{Ca}^{2+}$ -binding ratio of endogenous fixed buffers. (A) Example traces of  $\text{Ca}^{2+}$  transients in response to single APs recorded with different indicators (color-coded). Traces are averages of 25–30 sweeps and were digitally filtered for display (Fluo-4FF and OGB-5N examples were filtered to 100 Hz; remaining traces to 170 Hz). Black lines are exponential fits; arrowhead denotes time point of AP. The affinity ( $K_D$ ) and  $\text{Ca}^{2+}$ -binding ratio ( $\kappa_B$ ) of  $\text{Ca}^{2+}$  indicators are specified. (B) Example trace of  $\text{Ca}^{2+}$  transient in response to a single AP recorded with Fura-2 (average of 20 sweeps). (C) Inverse of the amplitude of AP-evoked  $\text{Ca}^{2+}$  transients recorded using different dyes plotted vs.  $\text{Ca}^{2+}$ -binding ratio of the indicator ( $\kappa_B$ ). The line represents a linear fit. Extrapolation to the abscissa gave an estimate of the  $\text{Ca}^{2+}$ -binding ratio of endogenous fixed buffers (arrow). Color-coding is identical to A and B. (D) Corresponding analysis of the decay time constant ( $\tau$ ) of  $\text{Ca}^{2+}$  transients. Resulting parameters are indicated. (E) Product of  $A$  and  $\tau$  plotted vs.  $\kappa_B$ . The line represents a linear fit.



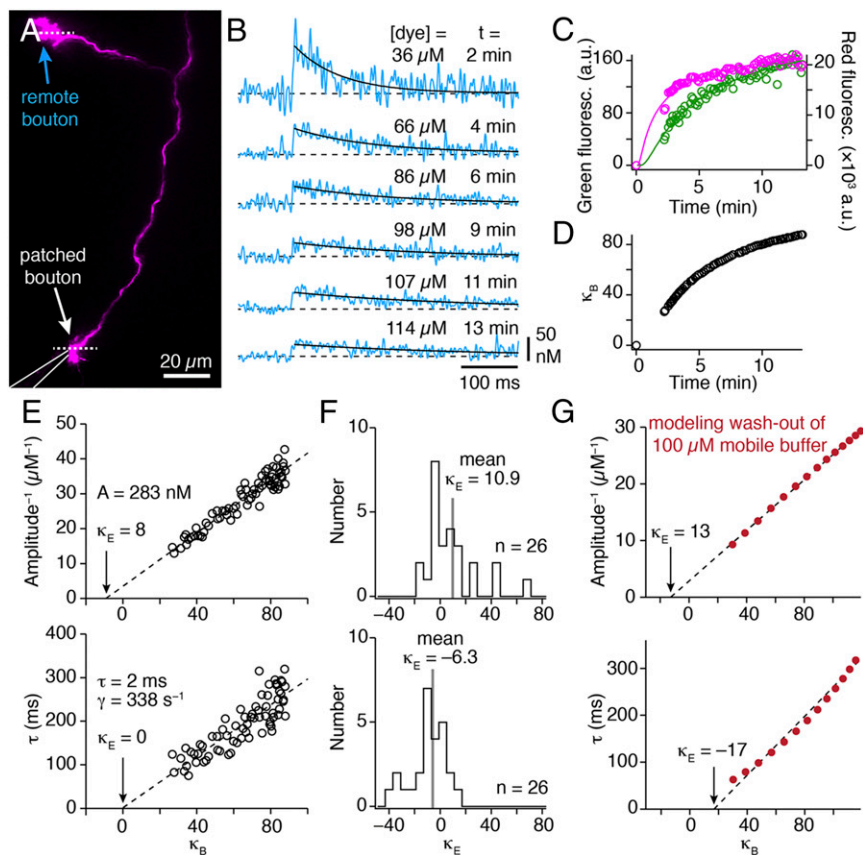


**Fig. 3.**  $\text{Ca}^{2+}$  transients in remote boutons indicate wash-out of a mobile buffer. (A) Two-photon image of a patched bouton filled with  $10 \mu\text{M}$  Atto594 and  $200 \mu\text{M}$  Fluo-5F (maximum z-projection of a stack of images over  $80 \mu\text{m}$ ; z-step,  $4 \mu\text{m}$ ; patch-pipette is illustrated schematically). Dotted lines indicate line scan positions in the patched and remote bouton. (B) Example traces of  $\text{Ca}^{2+}$  transients during dye loading in a remote bouton elicited by single APs at different time points after gaining whole-cell access. Time and estimated dye concentration are indicated; black lines represent exponential fits. (C) Red and green fluorescence at a remote bouton increase with time during whole-cell recording. Fluorescence was background subtracted and calculated over the whole trace (600 ms, red channel) or 90 ms of baseline before stimulation (green channel). Black lines are fits of Eq. 8. (D)  $\text{Ca}^{2+}$ -binding ratio of added buffer ( $\kappa_B$ ) vs. time. Dye concentration was calculated from the fit in C, and  $\kappa_B$  was computed using Eq. 5. (E) Inverse of the amplitude (Upper) and time constant  $\tau$  (Lower) of  $\text{Ca}^{2+}$  transients recorded during dye loading are plotted vs.  $\kappa_B$ . Lines represent linear fits; same experiment as in B. (F) Histograms of extrapolated  $\kappa_E$  values obtained from extrapolation of  $A^{-1}$  (Upper) and  $\tau$  (Lower) in 26 dye loading experiments. Mean value is indicated in gray. (G) Simulating  $\text{Ca}^{2+}$  transients during dye loading and simultaneous washout of a slow endogenous buffer ( $100 \mu\text{M}$  mobile buffer with EGTA-like kinetics, red circles). Wash-out of the slow buffer impacts on  $\tau$ -extrapolation, resulting in a negative  $\kappa_E$  estimate (dashed lines indicate linear extrapolation).

Fluo-5F and simultaneous wash-out of mobile buffers with slow binding kinetics reproduced well our observations (Fig. 3G).

To gain additional evidence that unperturbed cMFBs contain mobile  $\text{Ca}^{2+}$  buffers, we analyzed  $\text{Ca}^{2+}$  transients at the beginning of dye loading experiments. If a remote bouton was rapidly detected and recorded from, the initial concentration of added  $\text{Ca}^{2+}$  indicator was low ( $\kappa_B < 15$ ; mean  $\kappa_B = 9.0 \pm 1.3$ ;  $n = 8$ ).  $\text{Ca}^{2+}$  transients at the beginning of these experiments decayed with a time constant of  $51.2 \pm 12.5$  ms. Despite the presence of the  $\text{Ca}^{2+}$  indicator, the time constant is comparable to what the extrapolation to  $\kappa_B = 0$  predicted for patched boutons ( $\tau = 50$  ms; Fig. 2D). This observation again indicates that slow mobile buffers speed the decay of residual  $\text{Ca}^{2+}$  in cMFBs. We thus infer that cMFBs contain a substantial amount of endogenous mobile buffers.

**Mobile Buffers at cMFBs Have Slow Bindings Kinetics.** To gain insights into the properties of the mobile buffers, we compared  $\text{Ca}^{2+}$  transients in remote and patched boutons at identical dye concentration. In the dye loading experiments (Fluo-5F pipette concentration,  $200 \mu\text{M}$ ), we selected transients measured at  $\sim 50 \mu\text{M}$  Fluo-5F concentration ( $48.2 \pm 2.1 \mu\text{M}$ ,  $n = 24$ ) during dye loading in remote cMFBs to compare with  $\text{Ca}^{2+}$  transients recorded using  $50 \mu\text{M}$  Fluo-5F in separate experiments in patched cMFBs (Fig. 4A). The amplitudes were similar ( $P = 0.75$ ), but the decay was significantly faster in remote compared with patched cMFBs ( $P < 0.001$ ; Fig. 4B). This result is consistent with the presence of a mobile buffer with slow binding kinetics in remote boutons, because slow buffers speed the initial decay of the  $\text{Ca}^{2+}$  transient with little effect on amplitude (24). Note that the limited duration (500 ms) of our recordings precluded a detailed analysis of the slower exponential component resulting from the slow buffer, as discussed previously (25).

However, including  $100 \mu\text{M}$  EGTA in the patch-pipette reproduced the speeding of the initial decay time constant observed in remote boutons (Fig. 4A and B). Furthermore, simulating the effect of mobile buffers with EGTA-like kinetics on the  $\text{Ca}^{2+}$  transient replicated well our results (Fig. S4A and B). These data indicate that the endogenous mobile buffers at cMFBs have slow binding kinetics, high affinity, and are equivalent to  $\sim 100 \mu\text{M}$  EGTA (9).

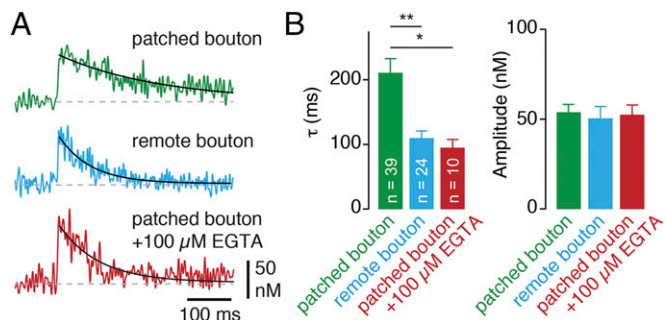


**Fig. 4.** Mobile buffers at cMFBs have slow bindings kinetics. (A) Example traces of  $\text{Ca}^{2+}$  transients evoked by a single AP. (Top)  $\text{Ca}^{2+}$  transient at a patched bouton recorded with  $50 \mu\text{M}$  Fluo-5F. (Middle)  $\text{Ca}^{2+}$  transient recorded with  $46 \mu\text{M}$  Fluo-5F in a remote bouton at the beginning of dye loading ( $200 \mu\text{M}$  Fluo-5F in the pipette solution). (Bottom)  $\text{Ca}^{2+}$  transient at a patched bouton measured with  $50 \mu\text{M}$  Fluo-5F and  $100 \mu\text{M}$  of the slow  $\text{Ca}^{2+}$  buffer EGTA. Traces are single sweeps. (B) Decay time constant ( $\tau$ ) and amplitude of  $\text{Ca}^{2+}$  transients evoked at patched (green) or remote boutons (blue) and with EGTA added to the pipette solution (red). The estimated concentration of Fluo-5F at remote boutons in the initial phase of dye loading was  $48.2 \pm 2.1 \mu\text{M}$  ( $n = 24$ ), which is comparable to the Fluo-5F concentration in patched cMFBs ( $50 \mu\text{M}$ ).

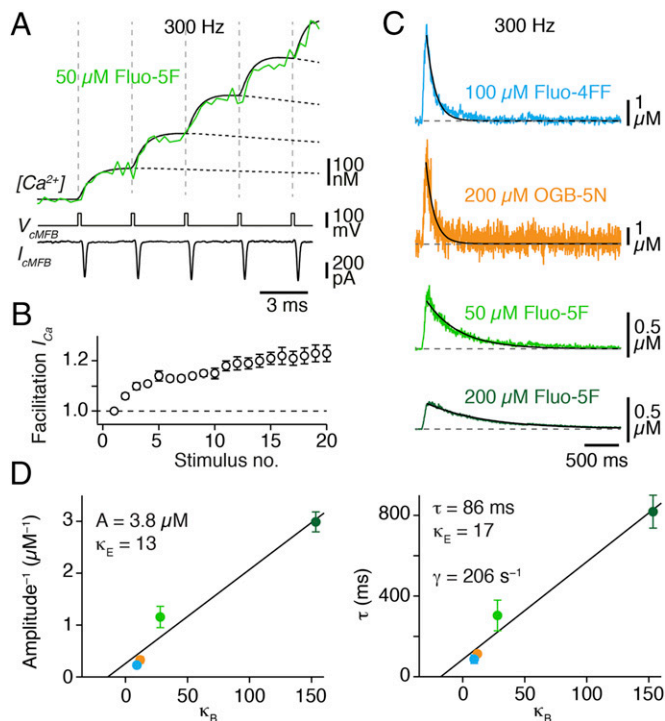


**Fig. 5.** Buildup of residual  $\text{Ca}^{2+}$  concentration during high-frequency firing. (A) (Top)  $\text{Ca}^{2+}$  concentration measured during the first five stimuli of 300-Hz AP firing in a cMFB with  $50 \mu\text{M}$  Fluo-5F (3-kHz temporal resolution) superimposed with the prediction of our model. (Middle) Voltage command. (Bottom) Corresponding presynaptic  $\text{Ca}^{2+}$  currents. Note the facilitation of the peak  $\text{Ca}^{2+}$  current amplitude. (B) Average peak  $\text{Ca}^{2+}$  current amplitude during high-frequency trains normalized to the first amplitude and plotted vs. stimulus number ( $n = 5$  cells). (C) Example traces of  $\text{Ca}^{2+}$  transients in response to a train of 20 APs at a frequency of 300 Hz measured with different  $\text{Ca}^{2+}$  indicators. Traces are averages of two to five sweeps; black lines represent exponential fits. (D) Inverse of the amplitude and time constants ( $\tau$ ) of  $\text{Ca}^{2+}$  transients in response to 20 APs at 300 Hz vs.  $\kappa_B$ . Lines represent linear fits; color-coding is identical to C.

**Buildup of Residual  $\text{Ca}^{2+}$  During High-Frequency Firing.** In vivo, cMFBs fire bursts of APs with exceptionally high frequencies (6, 26), where vesicular transmitter release is remarkably synchronous (8, 27). To understand which mechanisms enable synchronous high-frequency release, we measured the buildup of  $\text{Ca}^{2+}$  during high-frequency bursts (20 APs at 300 Hz). First, we analyzed the  $\text{Ca}^{2+}$  influx per AP during train stimulation by pharmacologically isolating the  $\text{Ca}^{2+}$  current elicited by AP-like stimuli (200  $\mu\text{s}$  to 0 mV; Fig. 5A).  $\text{Ca}^{2+}$  currents displayed facilitation during 300-Hz bursts (Fig. 5B), consistent with P/Q-type voltage-gated  $\text{Ca}^{2+}$  channels at cMFBs (8). Next, we used  $\text{Ca}^{2+}$  imaging to measure the increased spatially averaged residual  $[\text{Ca}^{2+}]$  by 300-Hz train stimulations (Fig. 5C). The increase caused by individual APs could be resolved well and appeared constant for the first APs of the train (Fig. 5A). Peak residual  $[\text{Ca}^{2+}]$  during the train in the absence of  $\text{Ca}^{2+}$  indicators was estimated as  $3.8 \mu\text{M}$  by back-extrapolation (Fig. 5D;  $[3.1\text{--}5.5 \mu\text{M}]$ , bootstrap 16–84% CI based on 40 experiments). The amplitude of  $3.8 \mu\text{M}$  indicates that the  $\text{Ca}^{2+}$  transients from single APs (amplitude,  $0.20 \mu\text{M}$ ; Fig. 2C) summate markedly during short high-frequency bursts, resulting in high peak  $[\text{Ca}^{2+}]$  during trains. The estimates for  $\tau$ ,  $\kappa_E$ , and  $\gamma$  from train stimulation ( $\tau = 86 \pm 26$  ms;  $\kappa_E = 13 \pm 5$  and  $17 \pm 7$  for  $A^{-1}$  and  $\tau$  extrapolation, respectively;  $\gamma = 210 \pm 27$   $\text{s}^{-1}$ ; bootstrap SEM based on  $n = 40$ ) were comparable to estimates from single APs (Fig. 2 and Fig. S3). However, analysis of stronger stimuli such as 100-ms depolarizations to 0 mV suggests a speeding of  $\text{Ca}^{2+}$  extrusion at higher  $[\text{Ca}^{2+}]$ , as previously described (28). To in-

vestigate the contribution of mobile buffers, we added  $100 \mu\text{M}$  of EGTA to the intracellular solution (Fig. S4C), which reduced the average peak amplitude by  $\sim 30\%$  ( $P = 0.046$ ; Fig. S4D). In excellent agreement, adding  $100 \mu\text{M}$  EGTA in simulations predicted a 31% reduction (Fig. S4E and F). The fast  $\text{Ca}^{2+}$ -extrusion mechanisms in cMFBs prevent a summation of the slow component of residual  $\text{Ca}^{2+}$  transients caused by mobile buffers, which can evoke delayed release at some synapses (29, 30). These data demonstrate that endogenous mobile buffers reduce the buildup of residual  $\text{Ca}^{2+}$  during high-frequency bursts at cMFBs.

**Modeling  $\text{Ca}^{2+}$  Transients in an Unperturbed Bouton.** Because  $\text{Ca}^{2+}$  indicators perturb intracellular  $[\text{Ca}^{2+}]$ , we used back-extrapolation to  $\kappa_B = 0$  in Figs. 2 and 5. Extrapolation, however, does not address wash-out of mobile buffers. We therefore developed a detailed model to analyze residual  $\text{Ca}^{2+}$  (Fig. 6) and active zone  $\text{Ca}^{2+}$  (Fig. 7) of the unperturbed terminal. The model cMFB included the experimentally determined endogenous buffers (Figs. 2–5),  $\text{Ca}^{2+}$  current amplitude (8), and  $\text{Ca}^{2+}$  current facilitation (Fig. 5B). The predicted free  $[\text{Ca}^{2+}]$  was calculated from  $\text{Ca}^{2+}$  indicator occupancy, similarly as experimentally performed (Materials and Methods). Kinetic parameters of endogenous buffers were taken as experimentally determined values (see below). The remaining free parameters were optimized to reproduce the experimental data for single APs and trains of APs at 300 Hz with a single set of parameters (Fig. 6A and B). With this model, we then analyzed  $\text{Ca}^{2+}$  transients in unperturbed boutons (without dyes, including mobile buffers), neglecting the possible influence of the intracellular solution on  $\text{Ca}^{2+}$ -extrusion mechanisms. Adding a mobile buffer (corresponding to  $100 \mu\text{M}$  EGTA) markedly speeded  $\text{Ca}^{2+}$  transients to a decay time constant of  $\sim 26$  ms (Fig. 6C and D). Thus, our data suggest that residual  $\text{Ca}^{2+}$  decays with a time constant of  $\sim 26$  ms and summates to a few micromolar during high-frequency firing in unperturbed boutons.

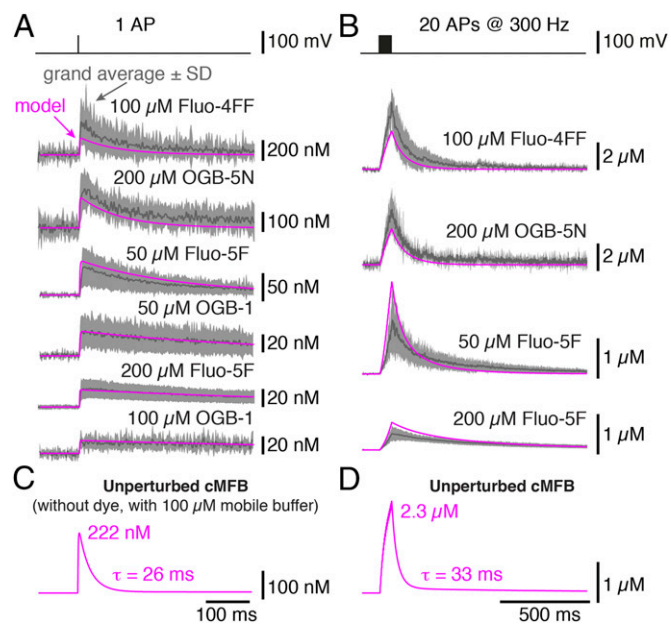


**Fig. 6.** Modeling  $\text{Ca}^{2+}$  transients in an unperturbed bouton. (A and B)  $\text{Ca}^{2+}$  transients elicited by a single AP (A) and a train of 20 APs at 300 Hz (B) recorded with different dyes superimposed with the corresponding model prediction (magenta). Bold lines are grand averages; gray shaded areas represent  $\pm$ SD. The model was optimized to best reproduce all traces with a single set of parameters. (C and D) Simulation of a  $\text{Ca}^{2+}$  transient in response to a single AP (C) and a train of 20 APs at 300 Hz (D) at an unperturbed bouton (containing  $100 \mu\text{M}$  of mobile buffer and no indicator dye).



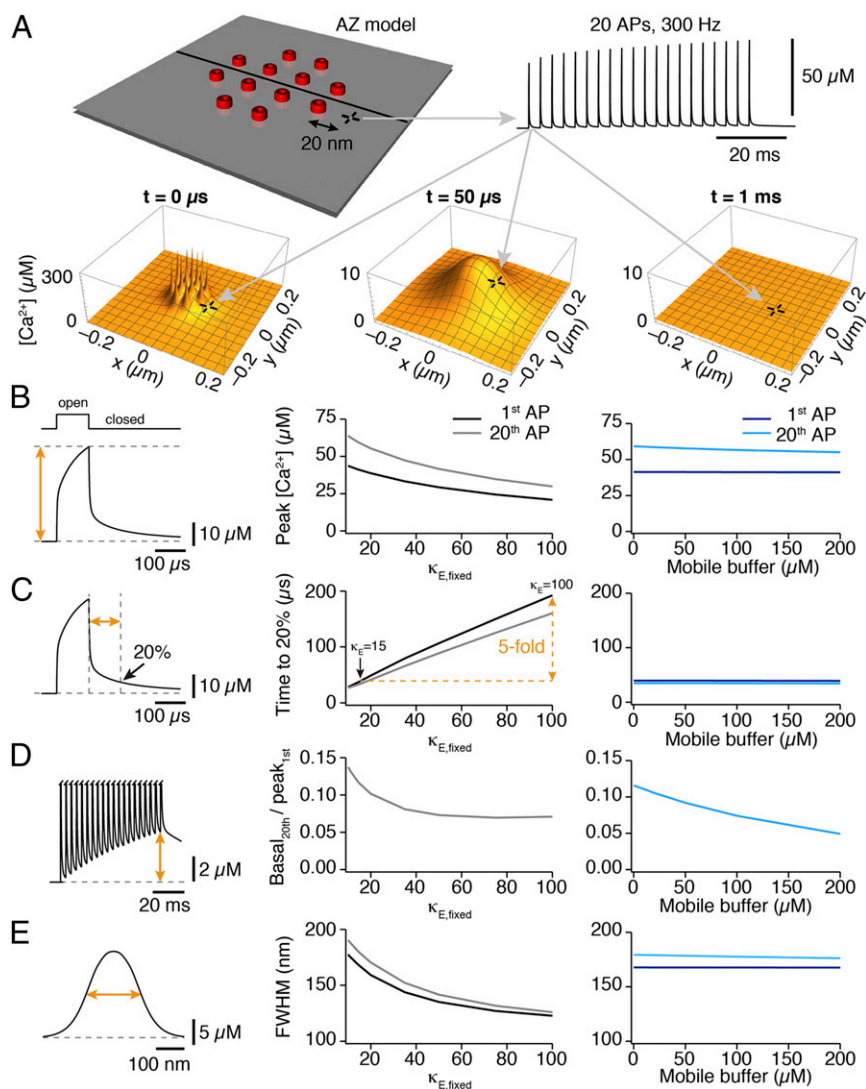


**Fig. 7.** Weak endogenous fixed buffers accelerate active zone Ca<sup>2+</sup> signaling. (A) Visualization of the active zone model. The active zone contained 12 Ca<sup>2+</sup> channels (red) spaced at 30 nm. The model simulated the influx, 3D buffered diffusion, and extrusion of Ca<sup>2+</sup>. For one point at a distance of 20 nm from the channel (cross), the [Ca<sup>2+</sup>] is shown during a train of 20 APs at 300 Hz (Upper Right). Note that the increase in peak amplitude is mainly due to the implemented Ca<sup>2+</sup> current facilitation (Fig. 5 A and B). The collapse of the free [Ca<sup>2+</sup>] microdomain is illustrated for three time points after the first AP ( $t = 0 \mu\text{s}$ ,  $50 \mu\text{s}$ , and  $1 \text{ ms}$ ; end of the AP defined as  $t = 0$ ). Within  $50 \mu\text{s}$ , the Ca<sup>2+</sup> domains of individual Ca<sup>2+</sup> channels collapsed to a microdomain Ca<sup>2+</sup> signal, which itself collapsed within  $1 \text{ ms}$ . (B) Peak amplitude of local [Ca<sup>2+</sup>] at a distance of 20 nm from the Ca<sup>2+</sup> channel during the 1st and 20th AP at 300 Hz was reduced by increasing  $\kappa_{E, \text{fixed}}$  (light and dark gray), but remained unaltered by increasing the concentration of mobile buffer (light and dark blue). The Ca<sup>2+</sup> channel opening and the resulting local [Ca<sup>2+</sup>] are illustrated on the left. (C) Active zone Ca<sup>2+</sup> clearance (defined as the time until the local [Ca<sup>2+</sup>] at 20 nm distance from the Ca<sup>2+</sup> channel reaches 20% of its peak amplitude) was considerably slowed by increasing  $\kappa_{E, \text{fixed}}$ , being approximately fivefold longer for  $\kappa_{E, \text{fixed}} = 100$  than for  $\kappa_{E, \text{fixed}} = 15$ . Active zone Ca<sup>2+</sup> clearance was independent of the amount of mobile buffer between 0 and 200  $\mu\text{M}$ . (D) Relative Ca<sup>2+</sup> buildup during repetitive firing (defined as the [Ca<sup>2+</sup>] before the 20th AP normalized to the peak [Ca<sup>2+</sup>] of the 1st AP) was reduced by increasing  $\kappa_{E, \text{fixed}}$  up to 50 and by increasing concentrations of mobile buffer. (E) The spatial extent of active zone Ca<sup>2+</sup> (defined as FWHM of a line profile through the center of the active zone  $50 \mu\text{s}$  after the AP) decreased with increasing  $\kappa_{E, \text{fixed}}$  but was unaffected by the amount of mobile buffer.

### Weak Endogenous Fixed Buffers Accelerate Active Zone Ca<sup>2+</sup> Signaling.

How can cMFBs sustain synchronous vesicular release despite the substantial summation of residual Ca<sup>2+</sup> during high-frequency firing? To address this question, we investigated the spatiotemporal dynamics of Ca<sup>2+</sup> at the active zone and the influence of endogenous fixed and mobile buffers. We simulated active zone Ca<sup>2+</sup> diffusion and buffering based on the model established above (*Materials and Methods*) during a train of 20 APs at 300 Hz. The local [Ca<sup>2+</sup>] of the 1st and 20th AP was analyzed at a distance of 20 nm from a channel (Fig. 7A). We focused our analysis on four functionally important parameters: First, the local peak [Ca<sup>2+</sup>] of the 1st and 20th AP, which was markedly decreased with increasing  $\kappa_{E, \text{fixed}}$ , but increasing the slow mobile buffer concentration (0–200  $\mu\text{M}$ ), had little effect (Fig. 7B). Second, the local Ca<sup>2+</sup> clearance was defined as the time needed for [Ca<sup>2+</sup>] to decrease to 20% of the peak during the AP. Clearance was much faster for lower  $\kappa_{E, \text{fixed}}$  (fivefold acceleration with  $\kappa_{E, \text{fixed}}$  of 15 compared with 100), but depended little on the amount of mobile buffer (Fig. 7C). Third, the relative Ca<sup>2+</sup> buildup during repetitive firing was defined as the [Ca<sup>2+</sup>] before the 20th AP normalized to the peak [Ca<sup>2+</sup>] of the 1st AP. Increasing  $\kappa_{E, \text{fixed}}$  up to 50 reduced the relative buildup by a factor of  $\sim 2$ , and increasing  $\kappa_{E, \text{fixed}}$  above 50 had no further effect. Increasing the mobile buffer concentration up to 200  $\mu\text{M}$  reduced the relative buildup by a factor of  $\sim 3$  (Fig. 7D).

Fourth, the spatial extent of active zone Ca<sup>2+</sup> was measured as full-width at half-maximum (FWHM) of a line profile through the center of the active zone  $50 \mu\text{s}$  after the AP. FWHM was markedly enlarged with lower  $\kappa_{E, \text{fixed}}$ , but remained unaltered by changing the amount of mobile buffer (Fig. 7E), consistent with previous analytical calculations of the length constant (mean distance a Ca<sup>2+</sup> ion diffuses before being captured by a buffer molecule) (31, 32). To investigate the sensitivity of our results on the parameters of the model, we varied these parameters and obtained similar results to those shown in Fig. 7, revealing the robustness of our modeling approach (*Materials and Methods*).

These data demonstrate that a low  $\kappa_{E, \text{fixed}}$  enables active zone Ca<sup>2+</sup> signals with high amplitude, large spatial extent, and rapid decay. Furthermore, a high concentration of mobile buffer reduces the buildup of Ca<sup>2+</sup> between APs. Thus, fixed endogenous buffers with low affinity and low Ca<sup>2+</sup>-binding ratio in combination with mobile buffers with high affinity seem ideally suited to speed active zone Ca<sup>2+</sup> clearance and thus enable synchronous and reliable high-frequency transmission.

**Ca<sup>2+</sup> Signals at Different Distances from Active Zones.** The rapid clearance of Ca<sup>2+</sup> from the active zone suggests that during an AP, Ca<sup>2+</sup> rapidly diffuses from active zones into the center of the presynaptic terminal. One might therefore expect that [Ca<sup>2+</sup>] rises slightly slower at the center of the cMFB than at the edge

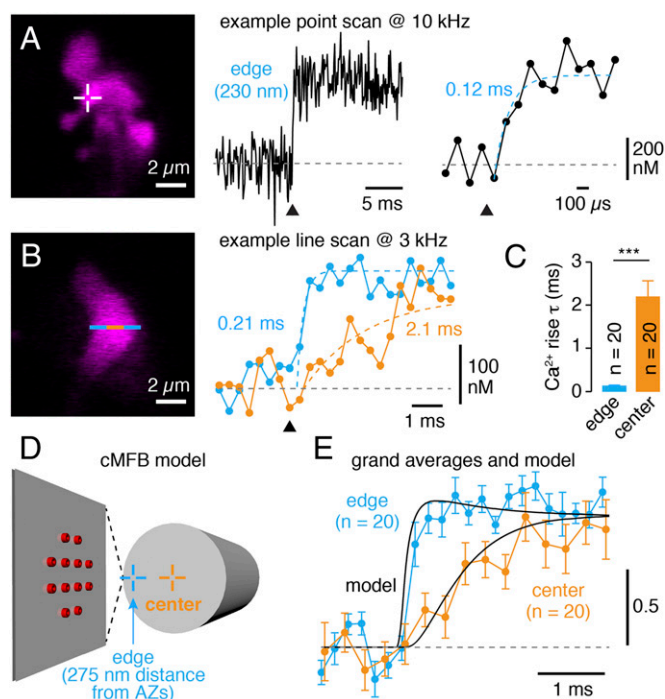


**Fig. 8.**  $\text{Ca}^{2+}$  signals at different distances from active zones. (A) Example of a two-photon point scan (sampling rate, 10 kHz) close to the edge of a cMFB (230 nm). (Left) Two-photon image of bouton filled with  $10 \mu\text{M}$  Atto594 and  $200 \mu\text{M}$  OGB-5N. (Center) In response to an AP (arrowhead), a rapid rise of  $[\text{Ca}^{2+}]$  was observed. Unfiltered data trace; average of 34 traces. (Right) Rise of  $[\text{Ca}^{2+}]$  on expanded time scale superimposed with exponential fit (blue dotted line; time constant,  $120 \mu\text{s}$ ). (B) Example of two-photon line scan at 3-kHz resolution at the center and close to the edge of boutons. (Left) Two-photon image of a bouton filled with  $10 \mu\text{M}$  Atto594 and  $200 \mu\text{M}$  OGB-5N. (Right) In response to an AP (arrowhead), a faster rise of  $[\text{Ca}^{2+}]$  was observed close to the edge of the cMFB compared with the center. Average of 49 traces each; blue and orange dotted lines are exponential fits, time constants are indicated. (C) Average rise time constants ( $n = 20$  each,  $P < 0.00001$ , unpaired  $t$  test). (D) Illustration of the cylindrical cMFB model.  $\text{Ca}^{2+}$  influx occurs at the surface of the cylinder, where active zones are located. (E) Grand averages of subbouton  $\text{Ca}^{2+}$  signals superimposed with the model predictions at two distances from the surface (edge,  $275 \text{ nm}$ ; center,  $0.9 \mu\text{m}$ ) as illustrated in D. Data were peak normalized and binned with  $0.2\text{-ms}$  (edge,  $n = 20$ ) or  $0.3\text{-ms}$  bin duration (center,  $n = 20$ ); error bars represent SEM.

where active zones are located. To experimentally confirm this prediction, we performed measurements with the low-affinity dye OGB-5N and with increased spatial and temporal resolution. High-resolution point and line measurements (5- to 10- and 1- to 3-kHz sampling rate, respectively) revealed extremely rapid rise kinetics at the edge of cMFBs ( $0.143 \pm 0.01 \text{ ms}$ ;  $n = 20$ ; average distance to edge,  $278 \pm 42 \text{ nm}$ ), significantly faster than at the center ( $2.20 \pm 0.37 \text{ ms}$ ,  $n = 20$ ;  $P < 0.001$ , unpaired  $t$  test; Fig. 8 A–C). The resolved difference in  $\text{Ca}^{2+}$  kinetics is most likely caused by equilibration of  $\text{Ca}^{2+}$  microdomains within cMFBs. In our cMFB model, the  $\text{Ca}^{2+}$  influx is restricted to the surface of the cylinder, representing the  $\sim 300$  active zones at the surface of cMFBs (Fig. 8D). The model nicely reproduced the high-resolution  $\text{Ca}^{2+}$  measurements (Fig. 8E), providing an independent validation of our modeling approach.

From the high-resolution data at the edge of cMFBs, we additionally determined limits for the binding kinetics of the endogenous fixed buffers. The analyses (Fig. S5) revealed that  $k_{\text{off}}$  must be  $>10,000 \text{ s}^{-1}$ ,  $K_{\text{D}} > 20 \mu\text{M}$ , and  $k_{\text{on}} < 6 \times 10^9 \text{ s}^{-1}\cdot\text{M}^{-1}$ , which is close to the upper diffusion limit. Our boundaries for  $k_{\text{off}}$  and  $K_{\text{D}}$  are similar to previous approximations at the calyx of

Held presynaptic terminal (20, 33) and at chromaffin cells (34) and indicate that the endogenous fixed buffers at cMFBs are of low affinity with fast binding kinetics.

#### Weak Endogenous Fixed Buffers Enable Highly Synchronous Release.

To investigate whether the rapid clearance of  $\text{Ca}^{2+}$  from the active zone caused by weak endogenous fixed buffers promotes synchronous neurotransmitter release, we simulated the time course of release rate for a single AP (Fig. 9A). The duration and amplitude of the vesicular release rate were highly dependent on  $\kappa_{\text{E, fixed}}$ . With  $\kappa_{\text{E, fixed}} = 15$ , the FWHM of the release rate was  $114 \mu\text{s}$ , similar to previously measured values (27). With  $\kappa_{\text{E, fixed}} = 100$ , however, the FWHM was prolonged 2.8-fold (Fig. 9B). These results had little dependence on the implementation of the release scheme (Fig. S6). Thus, the strength of endogenous fixed  $\text{Ca}^{2+}$  buffers limits the synchronicity of release.

#### Discussion

In this study, we identified the mechanisms controlling the speed of active zone  $\text{Ca}^{2+}$  signaling using quantitative two-photon  $\text{Ca}^{2+}$  imaging with submillisecond temporal and subbouton spatial resolution at central presynaptic terminals. We found a surprisingly low  $\text{Ca}^{2+}$ -binding ratio of endogenous fixed buffers. Our experimentally constrained model revealed that such weak  $\text{Ca}^{2+}$  buffering enables rapid diffusional removal of  $\text{Ca}^{2+}$  from the active zone. Thus, our study provides a framework of presynaptic  $\text{Ca}^{2+}$  signaling explaining how central synapses can sustain fast and synchronous neurotransmitter release.

**Low  $\text{Ca}^{2+}$ -Binding Ratio.** Dissection of fixed and mobile  $\text{Ca}^{2+}$  buffers requires efficient control of the cytosolic solution. This procedure has been performed at few preparations such as chromaffin cells (23, 35) and dendrites dialyzed via somatic recordings (18, 36–39). Previous studies investigating  $\kappa_{\text{E}}$  at presynaptic terminals provided estimates ranging from  $\sim 20$  at hippocampal mossy fiber boutons (15),  $\sim 56$  at boutons of cerebellar granule cells (21), and  $\sim 140$  at boutons of layer 2/3 neocortical pyramidal cells (22), to up to  $\sim 1,000$  at the crayfish neuromuscular junction (40). Due to somatic or axonal loading in these studies, however, mobile buffers might have contributed,

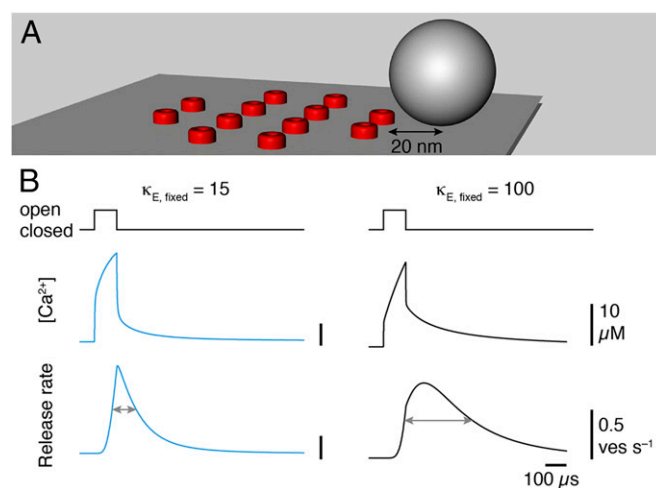


**Fig. 9.** Weak endogenous fixed buffers enable highly synchronous release. (A) Visualization of the active zone model (Fig. 7).  $\text{Ca}^{2+}$  channel to vesicle coupling distance was  $20 \text{ nm}$ . The release scheme was based on ref. 75; see Fig. S6 for details. (B) Comparison of the local  $[\text{Ca}^{2+}]$  at the position of the vesicle (Middle) and release rate (Bottom) for a single AP ( $\text{Ca}^{2+}$  channel opening illustrated at Top) with different binding ratios of fixed buffer ( $\kappa_{\text{E, fixed}} = 15$  and  $100$ ). Low  $\kappa_{\text{E, fixed}}$  leads to highly synchronous release.



leading either to overestimation of  $\kappa_{E, \text{fixed}}$  or, as demonstrated in Fig. 3G, to underestimation of  $\kappa_{E, \text{fixed}}$ . To our knowledge, a rigorous dissection of mobile and fixed buffers at presynaptic terminals has only been possible at preloaded and whole-cell dialyzed calyx of Held synapses (9) and at somatically loaded presynaptic terminals of retinal bipolar cells (10). At the calyx of Held, values for  $\kappa_{E, \text{fixed}}$  of  $\sim 22$  (25),  $\sim 40$  (14, 20), or  $\sim 46$  (41) have been determined. By systematic dialysis of cMFBs with  $\text{Ca}^{2+}$  indicators of different affinity, we demonstrate a  $\text{Ca}^{2+}$ -binding ratio of the fixed buffers of  $\sim 15$  (Fig. 2). Thus, our data show that  $\kappa_{E, \text{fixed}}$  at cMFBs is lower than all previously determined values.

Because the estimate of  $\kappa_{E, \text{fixed}}$  depends on correct quantification of  $[\text{Ca}^{2+}]$ , we used three independent quantification approaches: two-photon  $\text{Ca}^{2+}$  imaging with dual-indicator quantification based on intrabouton calibration; two-photon  $\text{Ca}^{2+}$  imaging with single-indicator quantification based on an independent calibration approach (Figs. S1 and S2); and ratiometric  $\text{Ca}^{2+}$  imaging with Fura-2 using UV-epifluorescence excitation. The three independent methods were in excellent agreement, demonstrating the reliability of our quantification.

In addition, our high-resolution experiments revealed that the endogenous fixed buffers have low affinity ( $K_D > 20 \mu\text{M}$ ; Fig. S5), consistent with estimates at the calyx of Held (20, 33), indicating that fixed buffers are present at  $>300 \mu\text{M}$  concentration in cMFBs (calculated from  $\kappa_E = 15$  and  $K_D > 20 \mu\text{M}$ ; Fig. S5).

**Mobile  $\text{Ca}^{2+}$  Buffers with Slow Binding Kinetics.** By comparing remote and dialyzed boutons we demonstrate that—in addition to the background of fixed buffers—there is a small but substantial contribution of mobile  $\text{Ca}^{2+}$  buffers with slow, EGTA-like kinetics (Figs. 3 and 4). These high-affinity mobile buffers speed the decay of residual  $\text{Ca}^{2+}$  in cMFBs (Fig. 4) in a strikingly similar way to mobile buffers at the calyx of Held (9). In contrast, we found that mobile buffers had little impact on active zone  $\text{Ca}^{2+}$  clearance (see below). Simple calculation of the  $\text{Ca}^{2+}$ -binding ratio of mobile buffers ( $\kappa_B = [B]/K_D$ ) results in  $\sim 500$ . However, the concept of a binding ratio is only useful if  $\text{Ca}^{2+}$  and buffers are in kinetic equilibrium and if the equilibration time constant between slow buffers and  $\text{Ca}^{2+}$  is faster than the  $\text{Ca}^{2+}$ -extrusion rate (23). At cMFBs, though, extrusion and equilibration time constant are both in the range of 100 ms (Figs. 2 and 5).

The molecular identity of endogenous mobile buffers is unknown at cMFBs, but  $\text{Ca}^{2+}$ -binding proteins including parvalbumin, calretinin, and calbindin-D28k are obvious candidates (3, 42). Kinetically, parvalbumin seems a likely candidate for a slow buffer (9, 43). However, we found very weak expression levels of parvalbumin, calretinin, and calbindin-D28k assessed with immunohistochemistry in cMFBs, indicating that none of these proteins is a dominant  $\text{Ca}^{2+}$  buffer in cMFBs. Because  $\text{Ca}^{2+}$  transients were very similar in patched boutons in the presence of EGTA and in remote boutons in the presence of mobile buffers (Fig. 4), we used a mobile buffer with kinetics of EGTA in our simulations and did not implement any cooperativity (44, 45).

**Speeding Active Zone  $\text{Ca}^{2+}$  Signaling.** We show that a low  $\text{Ca}^{2+}$ -binding ratio of endogenous fixed buffers is essential for  $\text{Ca}^{2+}$  microdomains with high amplitudes, large spatial extent, and rapid clearance (Fig. 7). Although one could assume that a high  $\kappa_{E, \text{fixed}}$  has the potential to efficiently remove  $\text{Ca}^{2+}$  from the active zone, our results show the opposite, namely that a low  $\kappa_{E, \text{fixed}}$  speeds active zone  $\text{Ca}^{2+}$  clearance (Fig. 7). This finding can be explained by the acceleration of the apparent  $\text{Ca}^{2+}$  diffusion by reduced fixed buffers (46) and, intuitively, by less unbinding of  $\text{Ca}^{2+}$  from the fixed buffers in-between APs.

In addition, slow mobile buffers help to prevent facilitation of intracellular  $[\text{Ca}^{2+}]$  during high-frequency firing but have little impact on active zone  $\text{Ca}^{2+}$  signals at cMFBs (Fig. 7 and Fig. S4). In contrast, mobile buffers seem to influence active zone  $\text{Ca}^{2+}$

signals at hippocampal mossy fiber boutons (47) and ribbon-type synapses (10, 48, 49). In these preparations, however, the mobile buffers have faster kinetics and/or the  $\text{Ca}^{2+}$  channel to vesicle coupling is less tight compared with cMFBs (8). Under these conditions, binding to the slow buffer and an acceleration of the apparent  $\text{Ca}^{2+}$  diffusion by mobile buffers (37, 46, 50) are expected to impact active zone  $\text{Ca}^{2+}$  signals. Furthermore, our data argue against substantial saturation of mobile buffers causing facilitation of release (38, 51). The low affinity of fixed buffers at cMFBs (Fig. S5) also prevents substantial saturation, which would allow slow buffers to impact local  $\text{Ca}^{2+}$  signals (43).

Thus, our results establish that active zone  $\text{Ca}^{2+}$  signaling is mainly accelerated by the lack of a large amount of fixed buffers allowing rapid diffusional collapse of local  $\text{Ca}^{2+}$  signals and by mobile buffers with slow kinetics that bind  $\text{Ca}^{2+}$  during fast repetitive firing. This concept of active zone  $\text{Ca}^{2+}$  signaling is consistent with the low  $\kappa_{E, \text{fixed}}$  found in cMFBs and the synchronous release of cMFBs during high-frequency transmission (8). The previously determined larger presynaptic  $\kappa_{E, \text{fixed}}$  and the slower firing regimes of the respective synapses corroborate the concept that the strength of endogenous fixed buffers limits the maximum synchronous transmission frequency.

**Resolving Intrabouton  $\text{Ca}^{2+}$  Diffusion During Single APs.** In this study, we resolved local  $\text{Ca}^{2+}$  signals during the equilibration of microdomain  $\text{Ca}^{2+}$  at a mammalian central synapse (Fig. 8). Recently, local  $\text{Ca}^{2+}$  signals at synaptic and nonsynaptic regions were resolved with different rise time and initial amplitude at the calyx of Held synapse (20). Furthermore, local  $\text{Ca}^{2+}$  signals with long-lasting differences in amplitude were recorded at hippocampal mossy fiber boutons (52). In contrast, we measured complete  $\text{Ca}^{2+}$  equilibration within the first few milliseconds of a single AP. The fast rise time ( $\sim 140 \mu\text{s}$ ) argues that our local  $\text{Ca}^{2+}$  signals were recorded very close to the  $\text{Ca}^{2+}$  entry site. The small size of cMFBs with active zones that are small (diameter, 160 nm) (53) and closely spaced ( $\sim 400 \text{ nm}$ ) (54) can explain the rapid equilibration (model prediction in Fig. 8E).

Experimental high-resolution analysis of intrabouton  $\text{Ca}^{2+}$  diffusion is essential to understand  $\text{Ca}^{2+}$  dynamics at the active zone and to constrain computer simulations. Previously, comparable analyses of local  $\text{Ca}^{2+}$  signals have also been performed at neuromuscular junctions (2, 55), cerebellar synaptosomes (56), chromaffin cells (57), and inner hair cells (58). Our results at bona fide central synapses are consistent with the previous studies and extend our understanding of microdomain signaling by elucidating the differential role of endogenous fixed and mobile buffers for active zone  $\text{Ca}^{2+}$ -signals.

## Conclusion

The fixed endogenous  $\text{Ca}^{2+}$  buffers of cerebellar mossy fiber boutons are of low affinity and have a very low binding capacity. The buffering properties of cMFBs are ideal for rapid clearance of  $\text{Ca}^{2+}$  from the active zone, which allows synchronous release at high repetition rates. These data pinpoint the mechanisms allowing highly synchronous, fast neurotransmitter release at central presynaptic terminals.

## Materials and Methods

**Electrophysiology.** Cerebellar slices were prepared from P21–P61 CD-1, or C57BL/6 mice of either sex. Animals were treated in accordance with the German Protection of Animals Act and with the guidelines for the welfare of experimental animals issued by the European Communities Council Directive. Mice were anesthetized with isoflurane and killed by rapid decapitation; the cerebellar vermis was quickly removed and mounted in a chamber filled with chilled extracellular solution. Parasagittal 300- $\mu\text{m}$ -thick slices were cut using a Leica VT1200 microtome (Leica Microsystems), transferred to an incubation chamber at 35 °C for  $\sim 30 \text{ min}$ , and then stored at room temperature until use. The extracellular solution for slice cutting, storage, and experiments contained (in mM) the following: NaCl 125,  $\text{NaHCO}_3$  25, glucose 20, KCl 2.5,  $\text{CaCl}_2$  2,  $\text{NaH}_2\text{PO}_4$  1.25,  $\text{MgCl}_2$  1 (310 mOsm,

pH 7.3 when bubbled with Carbogen [5% (vol/vol) O<sub>2</sub>/95% (vol/vol) CO<sub>2</sub>]. Presynaptic patch-pipettes were pulled to open-tip resistances of 6–16 MΩ (when filled with intracellular solution) from borosilicate glass (Science Products) using a DMZ Puller (Zeitz-Instruments). The intracellular solution contained (in mM) the following: K-Gluconate 150, NaCl 10, K-Hepes 10, Mg-ATP 3, and Na-GTP 0.3 (pH adjusted to 7.3 using KOH). Atto594 (10–20 μM) and one of the following Ca<sup>2+</sup>-sensitive dyes were added to the intracellular solution: OGB-1 (50 or 100 μM), Fluo-5F (50 or 200 μM), Fluo-4FF (100 μM), or OGB-5N (200 μM). Experiments were performed at 34–37 °C. We purchased Atto594 from Atto-Tec, Ca<sup>2+</sup>-sensitive fluorophores from Life Technologies, and all other chemicals from Sigma-Aldrich.

Cerebellar mossy fiber boutons were visualized with oblique illumination and infrared optics. Whole-cell patch-clamp recordings from cMFBs were made using a HEKA EPC10/2 amplifier (HEKA Elektronik). Presynaptic cMFBs were identified as previously described (8). Measurements were corrected for a liquid junction potential of +13 mV. Series resistance was typically <40 MΩ. APs were evoked in current-clamp mode by brief current pulses (amplitude 50–500 pA; duration 1–3 ms). For train stimulations (20 stimuli at a frequency of 300 Hz), brief depolarizations (0 mV, 200 μs) were applied in voltage-clamp mode. Ca<sup>2+</sup> transients recorded in response to current injections (current-clamp) or short depolarizations (voltage-clamp) did not differ in amplitude or decay time constant (Fig. S1C). In voltage-clamp experiments, the holding potential was –80 mV.

**Quantitative Two-Photon Ca<sup>2+</sup> Imaging.** Two-photon Ca<sup>2+</sup> imaging was performed with a Femto2D laser-scanning microscope (Femtonics) equipped with a pulsed Ti:Sapphire laser (MaiTai, SpectraPhysics) tuned to 810 nm, a 60×/1.0 NA objective (Olympus) or 100×/1.1 NA objective (Nikon), and a 1.4 NA oil-immersion condenser (Olympus). Data were acquired in line scan mode, typically at a 1-kHz sampling rate. In a subset of experiments, we performed line- and point-scan measurements with a sampling rate of 3–10 kHz (Figs. 5A and 8 and Figs. S4 and S5). Background was measured outside of boutons in a neighboring area and subtracted. Imaging data were acquired and processed using Mes software (Femtonics).

We calculated the ratio (R) of green-over-red fluorescence to quantify intracellular [Ca<sup>2+</sup>] with Ca<sup>2+</sup> indicators of different affinity. Using green and red indicators, [Ca<sup>2+</sup>] can be calculated as (13)

$$[\text{Ca}^{2+}] = K_D \frac{R - R_{\min}}{R_{\max} - R} \quad [1]$$

Minimum (R<sub>min</sub>) and maximum (R<sub>max</sub>) fluorescence ratios were determined with 10 mM EGTA or 10 mM CaCl<sub>2</sub> in the intracellular solution, respectively. We performed these measurements *in situ*, i.e., in cMFBs or cerebellar granule cells to account for possible different dye properties in cytosol (17). Details of the calibration are described in *SI Materials and Methods*. For the high-affinity dye OGB-1, we also compared single- and dual-indicator quantification methods, which gave very similar results (*SI Materials and Methods* and Figs. S1B and S3A).

The decay of the Ca<sup>2+</sup> concentration (C) was fit with an exponential function

$$C(t) = A_0 + A e^{-(t/\tau)}, \quad [2]$$

where A<sub>0</sub> was constrained to the baseline level calculated for 20–90 ms before stimulation. For display purposes, Ca<sup>2+</sup> transients in the figures were digitally filtered using Igor Pro software (Wavemetrics; –3-dB filter cutoff frequency, 170 Hz) unless stated otherwise (Figs. 2A, 5A, and 8 and Fig. S5).

The two-photon signal is a convolution of the imaged structure and the microscope's point-spread function. Typical dimensions of two-photon point-spread functions are <1 μm radially and <2 μm axially (59). Because most cMFBs have a diameter >3 μm (54), the heterogeneous fluorescence signal within boutons (Fig. 8) cannot be explained by artifacts due to partial overlap of the point-spread function with boutons but rather represents kinetic differences of the intrabouton [Ca<sup>2+</sup>].

**Ratiometric Fura-2 Ca<sup>2+</sup> Imaging.** In addition, presynaptic Ca<sup>2+</sup> transients were recorded using Fura-2 (100 μM) and a Ca<sup>2+</sup>-imaging system (TILL-Photonics) with an excitation light source (Polychrome V) coupled to the epifluorescence port of the microscope (FN-1 with 100×/1.1 NA objective; Nikon) via a light guide, following previous descriptions (18, 33, 60). Fluorescence was measured with a back-illuminated electron-multiplying frame-transfer charge coupled device camera (iXon DU897; Andor Technology). Fura-2 fluorescence at both 350 and 380 nm was sampled every 10–30 ms; camera binning was 8 × 8. Background was measured in an area close to the patched bouton and subtracted. In these experiments, [Ca<sup>2+</sup>] was calculated as previously described (18, 33, 60)

$$[\text{Ca}^{2+}] = K_{\text{eff}} \frac{R - R_{\min}}{R_{\max} - R}, \quad [3]$$

and the effective dissociation constant (K<sub>eff</sub>) as

$$K_{\text{eff}} = K_D \frac{R_{\max} + \alpha}{R_{\min} + \alpha}, \quad [4]$$

where α is the isocoefficient, K<sub>D</sub> the dissociation constant of Fura-2 (0.286 μM) (36), and R = F<sub>1</sub>/F<sub>2</sub>, where F<sub>1</sub> and F<sub>2</sub> are the background-subtracted fluorescence intensities at 350 and 380 nm, respectively. For Fura-2 experiments, R<sub>max</sub> and R<sub>min</sub> were measured in cells using 10 mM CaCl<sub>2</sub> or 10 mM EGTA, respectively. The isocoefficient α was determined by adjusting α to obtain a Ca<sup>2+</sup> independent sum of F<sub>1</sub> + αF<sub>2</sub> as previously described (35), resulting in a value of ~0.05.

**Estimation of Endogenous Buffer Ratio.** We used the “added buffer method” to estimate the endogenous buffering capacity at cMFBs (17). The incremental Ca<sup>2+</sup>-binding ratio of exogenous buffers (κ<sub>B</sub>) was calculated as (14)

$$\kappa_B = \frac{[B]K_D}{([\text{Ca}^{2+}]_{\text{rest}} + K_D)([\text{Ca}^{2+}]_{\text{peak}} + K_D)}, \quad [5]$$

where [B] is the concentration of the exogenous buffer, [Ca<sup>2+</sup>]<sub>rest</sub> is the free Ca<sup>2+</sup> concentration under resting conditions, and [Ca<sup>2+</sup>]<sub>peak</sub> = [Ca<sup>2+</sup>]<sub>rest</sub> + Δ[Ca<sup>2+</sup>]<sub>AP</sub>, where Δ[Ca<sup>2+</sup>]<sub>AP</sub> is the baseline subtracted amplitude of the AP-evoked Ca<sup>2+</sup> transient. According to the single-compartment model, the decay time constant (τ) and the inverse of the amplitude (A<sup>–1</sup>) of the Ca<sup>2+</sup> transient depend linearly on κ<sub>B</sub> of the added buffer (4, 36)

$$A = \frac{Q_{\text{Ca}}/(2FV)}{(1 + \kappa_B + \kappa_E)}, \quad [6]$$

$$\tau = \frac{(1 + \kappa_B + \kappa_E)}{\gamma}, \quad [7]$$

where Q<sub>Ca</sub> is the charge flowing into the presynaptic terminal, F is the Faraday constant, V is the accessible volume of the terminal, and γ is the Ca<sup>2+</sup>-extrusion rate. We plotted A<sup>–1</sup> and τ obtained from experiments vs. κ<sub>B</sub>. Extrapolation of the linear regression line to κ<sub>B</sub> = 0 yields an estimate of the Ca<sup>2+</sup> transient without added exogenous buffer; the x axis intercept equals –(1 + κ<sub>E</sub>) (4). Gluconate and nucleotides in the intracellular solution contribute an additional κ of ~4.5 (61). We therefore added 4.5 to all κ<sub>B</sub> values of the intracellular solutions in our analysis.

Confidence intervals of κ<sub>E</sub>, A, τ, and γ estimates by back-extrapolation (Figs. 2 and 5) were determined by bootstrap procedures (62) implemented in Mathematica 10. An artificial dataset was taken from the original dataset, with replacement. Ten thousand datasets were generated and analyzed as the original dataset.

**Dye Loading in Remote Boutons.** cMFBs were filled with 10–20 μM Atto594 for visualization and 200 μM Fluo-5F to record Ca<sup>2+</sup> transients at remote boutons. Immediately after gaining whole-cell access, the red channel was used to locate a remote bouton along the same axon. Ca<sup>2+</sup> transients were subsequently recorded at this remote bouton with APs evoked in current-clamp mode every 15–30 s. To describe the diffusion of dyes and endogenous mobile buffers, the mossy fiber axon was approximated by a semi-infinite cylinder. Consequently, the intensity of fluorescence reflecting the increasing dye concentration over time was fit using the following equation (63):

$$F(t) = F_0 \operatorname{erfc}\left(\frac{x}{2\sqrt{Dt}}\right), \quad [8]$$

where F<sub>0</sub> denotes the fluorescence at maximum dye concentration during steady state, x is the distance (constrained to the measured distance between patched and remote bouton in every experiment), D is the diffusion coefficient of the dye, and *erfc* is the complementary error function given as

$$\operatorname{erfc}(z) = \frac{2}{\sqrt{\pi}} \int_z^\infty e^{-y^2} dy. \quad [9]$$

Red and green fluorescence (i.e., 90-ms baseline before AP) was plotted vs. dye-loading time (Fig. 3C) and fit using Eq. 8.

In all experiments, the resulting apparent diffusion coefficients were higher for Atto594 than for Fluo-5F ( $35.4 \pm 7.0$  and  $20.5 \pm 4.0 \mu\text{m}^2\text{s}^{-1}$ , respectively). Therefore, we determined the concentration of the dyes separately from the fit with Eq. 8, referred to as [Atto] and [Fluo] in the following. For each time point of the dye loading, we calculated a corrected green-over-red ratio  $R^*$  as

$$R^* = R \frac{[\text{Atto}]/[\text{Atto}]_{\text{pipette}}}{[\text{Fluo}]/[\text{Fluo}]_{\text{pipette}}}, \quad [10]$$

where  $[\text{Atto}]_{\text{pipette}}$  and  $[\text{Fluo}]_{\text{pipette}}$  are the red and green dye concentrations in the pipette, respectively.  $\kappa_B$  was determined with Eq. 5 using the [Fluo] and  $\text{Ca}^{2+}$  transient amplitude. At the end of dye loading experiments,  $\text{Ca}^{2+}$  transients in remote boutons had a slightly faster decay and higher amplitude than in patched boutons ( $\tau$ :  $494 \pm 55$  vs.  $681 \pm 47$  ms,  $P = 0.02$ ; amplitude:  $24.3 \pm 3.4$  vs.  $19.7 \pm 1.1$  nM,  $P = 0.1$ ;  $n = 26$  and  $57$ , respectively). This difference is consistent with lower dye concentrations in remote compared with patched boutons, as expected from Eq. 8 and the limited time course of these experiments. In our analysis, we did not correct for differences in z-depth between patched and remote boutons, as fluorescence ratios were <20% different up to 100- $\mu\text{m}$  depth measured with sealed pipettes.

**$\text{Ca}^{2+}$  Current Recordings.** In some experiments (Fig. 5 A and B), we pharmacologically isolated presynaptic  $\text{Ca}^{2+}$  currents during cMFB whole-cell patch-clamp recordings as previously described (8).  $\text{Ca}^{2+}$  currents were elicited by step depolarizations of 200- $\mu\text{s}$  duration from  $-80$  to  $0$  mV.  $\text{Ca}^{2+}$  currents were corrected for leak and capacitance currents using the P/4 method. In these experiments, the extracellular solution consisted of (in mM) the following: NaCl 105, KCl 2.5,  $\text{NaH}_2\text{PO}_4$  1.25,  $\text{NaHCO}_3$  25, glucose 25,  $\text{CaCl}_2$  2,  $\text{MgCl}_2$  1, TTX 0.001, 4-AP 5, and TEA 20. The presynaptic patch pipette contained (in mM) the following: CsCl 135, TEA-Cl 20, MgATP 4, NaGTP 0.3,  $\text{Na}_2\text{phosphocreatine}$  5, Hepes 10, and EGTA 0.2.

**Modeling of Spatiotemporal  $\text{Ca}^{2+}$  Diffusion and Buffering.** The model simulated the time course of  $\text{Ca}^{2+}$  influx and buffered diffusion in a cMFB, using a finite-difference scheme (51, 64–66). Previous electrophysiological experiments (8) and our  $\text{Ca}^{2+}$ -imaging measurements constrained key parameters of the model (Table S1). Simulations were implemented in CalC 7.7.4 (67); further evaluations were performed with Wolfram Mathematica 10. All calculations were executed on a MacBook Pro computer with 2.7-GHz Intel Core i7 processor and 16-GB RAM operating on Mac OS X 10.8.

When simulating  $\text{Ca}^{2+}$  dynamics in the whole cMFB (Figs. 6 and 8), we assumed a cylindrical morphology, 1.8  $\mu\text{m}$  in diameter and 24.8  $\mu\text{m}$  in length, to reproduce the  $\text{Ca}^{2+}$  transients recorded with the various dyes (Fig. 6) and the diffusional properties within cMFBs (Fig. 8). Grid size of the model was set to 20 points in radial and longitudinal dimensions (increasing grid size did not change the results). The AP-evoked  $\text{Ca}^{2+}$  current influx at the surface of the cylinder was approximated by a Gaussian of 99- $\mu\text{s}$  FWHM and 543-pA peak amplitude (8). The simulations included fixed endogenous buffers, ATP, gluconate (Table S1), and the following  $\text{Ca}^{2+}$  extrusion pump mechanism, which was implemented with the  $\text{Ca}^{2+}$  flux,  $J$ , defined as

$$J = -\gamma([\text{Ca}^{2+}] - [\text{Ca}^{2+}]_{\text{rest}}) - V_{\text{max}} \left( \frac{[\text{Ca}^{2+}]^n}{[\text{Ca}^{2+}]^n + K_D^n} - \frac{[\text{Ca}^{2+}]_{\text{rest}}^n}{[\text{Ca}^{2+}]_{\text{rest}}^n + K_D^n} \right), \quad [11]$$

where  $\gamma = 0.14 \mu\text{M}\cdot\text{ms}^{-1}$ ,  $V_{\text{max}} = 0.25 \mu\text{M}\cdot\mu\text{m}\cdot\text{ms}^{-1}$ ,  $n = 2.5$ , and  $K_D = 3.7 \mu\text{M}$ .  $J$  has units of  $\mu\text{M}\cdot\mu\text{m}\cdot\text{ms}^{-1} = 10^{-6} \text{mol}\cdot\text{m}^{-2}\cdot\text{s}^{-1}$ . The second nonlinear component of the definition describes the speeding of  $\text{Ca}^{2+}$  extrusion at higher  $[\text{Ca}^{2+}]$ , e.g., during 100-ms depolarization to 0 mV, and is based on previous analyses of  $\text{Ca}^{2+}$  extrusion mechanisms (28). The parameters  $V_{\text{max}}$ ,  $n$ , and  $K_D$  were adjusted to reproduce the measured  $\text{Ca}^{2+}$  transients elicited by single APs and trains of APs (Fig. 6 A and B). The model did not include an axon, but diffusion of  $\text{Ca}^{2+}$  into the mossy fiber axon would be pooled in the implemented extrusion mechanism.

When modeling  $\text{Ca}^{2+}$  dynamics on a fine spatial scale at a single active zone (Fig. 7), we represented the active zone with a rectangular box (65). To reduce simulation time we took advantage of the assumed symmetry with respect to two perpendicular planes and considered only a quarter of this volume comprising three  $\text{Ca}^{2+}$  channels. The x-y dimensions were 0.23  $\mu\text{m}$  (corresponding to half of the distance between neighboring active zones) (54), and the z dimension was 1.0  $\mu\text{m}$ . The active zone model had a spatial grid of  $50 \times 50 \times 30$  points ( $x, y, z$ ), with slight stretching implemented in the corner containing the channels (51). Boundary conditions on all side surfaces were set to be no flux and on the top surface to Dirichlet (boundary value clamped to background  $[\text{Ca}^{2+}]$ ). On the bottom surface ( $\text{Ca}^{2+}$  channel plane), the  $\text{Ca}^{2+}$  extrusion pump (Eq. 11) was added. Parameters used in the simulations are given in Table S1. Binding rates of EGTA were taken from ref. 68, which were estimated at physiological temperature and pH 7.3. The resulting  $K_D$  was 200 nM, which is similar to commonly used parameters estimated at room temperature (69, 70). To analyze unperturbed active zone  $\text{Ca}^{2+}$  signaling, active zone simulations included ATP and fixed and mobile buffers as stated (Fig. 7) without gluconate.

Per active zone, 12 open  $\text{Ca}^{2+}$  channels with a single channel current of 0.15 pA (71) and a duration of 105  $\mu\text{s}$  (8) were assumed. The number of  $\text{Ca}^{2+}$  channels is thus constrained by the measured  $\text{Ca}^{2+}$  influx per AP in cMFBs (macroscopic Gaussian-like  $\text{Ca}^{2+}$  current with half-duration of 99  $\mu\text{s}$ , and peak amplitude of 543 pA) (8), assuming 300 active zones per cMFB (54). The distance between  $\text{Ca}^{2+}$  channels was 30 nm, consistent with freeze-fracture replica labeling (8). Channel open times were fixed for all channels, and single channel open probability was set to 1. Stochastic implementation of an open probability < 1 (71) would result in a larger number of channels per simulated active zone due to the constraint by the measured  $\text{Ca}^{2+}$  influx. A larger number would increase the net distance between open channels, which was addressed in the following sensitivity analysis.

To investigate the sensitivity of simulations on model parameters, we systematically varied the number of open  $\text{Ca}^{2+}$  channels (range, 4–36), single channel conductance (range, 0.05–0.4 pA), distance between  $\text{Ca}^{2+}$  channels (range, 10–60 nm), and the distance of the position where the local  $\text{Ca}^{2+}$  concentration was sampled to the nearest  $\text{Ca}^{2+}$  channel (range, 10–60 nm). Furthermore, the number of x-y grid points (range, 10–80) and CalC accuracy parameter (range,  $10^{-1}$ – $10^{-7}$ ) were varied. As expected from previous studies investigating the impact of  $\text{Ca}^{2+}$  distribution on synaptic release (20, 65, 66, 72–74), the peak local  $[\text{Ca}^{2+}]$  was different when we varied the model parameters (range, 12–122  $\mu\text{M}$ ). However, the main finding of this study—the speeding of active zone  $\text{Ca}^{2+}$  signaling with low  $\kappa_{E,\text{fixed}}$ —was very robust with all tested parameters (fold-change of clearance time for  $\kappa_{E,\text{fixed}}$  of 15 and 100 as indicated in Fig. 7C ranged from 3.2 to 8.9).

**Modeling of the Release Time Course.** To simulate the time course of vesicular release rate at cMFBs, we used the described model of the active zone and included a release sensor at 20-nm distance from the nearest  $\text{Ca}^{2+}$  channel. The release scheme was taken from ref. 75 and was adjusted for physiological temperature and a release probability of 0.3 (76). To test the sensitivity of our findings on the used release scheme, we systematically compared several release schemes as explained in detail in Fig. S6.

**Data Analysis.** Statistical comparisons were performed via two-sided paired or unpaired Student  $t$  tests;  $P < 0.05$  was considered significant. Means are expressed  $\pm$  SEM except where stated.

**ACKNOWLEDGMENTS.** We thank David A. DiGregorio, Jens Eilers, Hartmut Schmidt, Beat Schwaller, and R. Angus Silver for critically reading the manuscript. This work was supported by Heisenberg Program of the German Research Foundation Grant HA 6386/2-2 and 3-2 (to S.H.) and National Science Foundation Grant DMS-0817703 (to V.M.).

- Neher E, Sakaba T (2008) Multiple roles of calcium ions in the regulation of neurotransmitter release. *Neuron* 59(6):861–872.
- Llinás R, Sugimori M, Silver RB (1992) Microdomains of high calcium concentration in a presynaptic terminal. *Science* 256(5057):677–679.
- Schwaller B (2010) Cytosolic  $\text{Ca}^{2+}$  buffers. *Cold Spring Harb Perspect Biol* 2(11):a004051.
- Neher E, Augustine GJ (1992) Calcium gradients and buffers in bovine chromaffin cells. *J Physiol* 450:273–301.
- Eggermann E, Bucurenciu I, Goswami SP, Jonas P (2012) Nanodomain coupling between  $\text{Ca}^{2+}$  channels and sensors of exocytosis at fast mammalian synapses. *Nat Rev Neurosci* 13(1):7–21.
- Rancz EA, et al. (2007) High-fidelity transmission of sensory information by single cerebellar mossy fibre boutons. *Nature* 450(7173):1245–1248.
- Saviane C, Silver RA (2006) Fast vesicle reloading and a large pool sustain high bandwidth transmission at a central synapse. *Nature* 439(7079):983–987.
- Ritzau-Jost A, et al. (2014) Ultrafast action potentials mediate kilohertz signaling at a central synapse. *Neuron* 84(1):152–163.
- Müller M, Felmy F, Schwaller B, Schneggenburger R (2007) Parvalbumin is a mobile presynaptic  $\text{Ca}^{2+}$  buffer in the calyx of Held that accelerates the decay of  $\text{Ca}^{2+}$  and short-term facilitation. *J Neurosci* 27(9):2261–2271.
- Burrone J, Neves G, Gomis A, Cooke A, Lagnado L (2002) Endogenous calcium buffers regulate fast exocytosis in the synaptic terminal of retinal bipolar cells. *Neuron* 33(1):101–112.
- Thomsen LB, Jörntell H, Midtgaard J (2010) Presynaptic calcium signalling in cerebellar mossy fibres. *Front Neural Circuits* 4:1.



12. Beierlein M, Gee KR, Martin VV, Regehr WG (2004) Presynaptic calcium measurements at physiological temperatures using a new class of dextran-conjugated indicators. *J Neurophysiol* 92(1):591–599.
13. Yasuda R, et al. (2004) Imaging calcium concentration dynamics in small neuronal compartments. *Sci STKE* 2004(219):pl5.
14. Helmchen F, Borst JG, Sakmann B (1997) Calcium dynamics associated with a single action potential in a CNS presynaptic terminal. *Biophys J* 72(3):1458–1471.
15. Jackson MB, Redman SJ (2003) Calcium dynamics, buffering, and buffer saturation in the boutons of dentate granule-cell axons in the hilus. *J Neurosci* 23(5):1612–1621.
16. Scott R, Rusakov DA (2006) Main determinants of presynaptic  $\text{Ca}^{2+}$  dynamics at individual mossy fiber-CA3 pyramidal cell synapses. *J Neurosci* 26(26):7071–7081.
17. Neher E (1995) The use of fura-2 for estimating Ca buffers and Ca fluxes. *Neuropharmacology* 34(11):1423–1442.
18. Lee SH, Rosenmund C, Schwaller B, Neher E (2000) Differences in  $\text{Ca}^{2+}$  buffering properties between excitatory and inhibitory hippocampal neurons from the rat. *J Physiol* 525(Pt 2):405–418.
19. Maravall M, Mainen ZF, Sabatini BL, Svoboda K (2000) Estimating intracellular calcium concentrations and buffering without wavelength ratioing. *Biophys J* 78(5):2655–2667.
20. Nakamura Y, et al. (2015) Nanoscale Distribution of Presynaptic  $\text{Ca}^{2+}$  Channels and Its Impact on Vesicular Release during Development. *Neuron* 85(1):145–158.
21. Brenowitz SD, Regehr WG (2007) Reliability and heterogeneity of calcium signaling at single presynaptic boutons of cerebellar granule cells. *J Neurosci* 27(30):7888–7898.
22. Koester HJ, Sakmann B (2000) Calcium dynamics associated with action potentials in single nerve terminals of pyramidal cells in layer 2/3 of the young rat neocortex. *J Physiol* 529(Pt 3):625–646.
23. Lee SH, Schwaller B, Neher E (2000) Kinetics of  $\text{Ca}^{2+}$  binding to parvalbumin in bovine chromaffin cells: Implications for  $[\text{Ca}^{2+}]$  transients of neuronal dendrites. *J Physiol* 525(Pt 2):419–432.
24. Sala F, Hernández-Cruz A (1990) Calcium diffusion modeling in a spherical neuron. Relevance of buffering properties. *Biophys J* 57(2):313–324.
25. Neher E, Taschenberger H (2013) Transients in global  $\text{Ca}^{2+}$  concentration induced by electrical activity in a giant nerve terminal. *J Physiol* 591(Pt 13):3189–3195.
26. Jörntell H, Ekerot CF (2006) Properties of somatosensory synaptic integration in cerebellar granule cells in vivo. *J Neurosci* 26(45):11786–11797.
27. Sargent PB, Saviane C, Nielsen TA, DiGregorio DA, Silver RA (2005) Rapid vesicular release, quantal variability, and spillover contribute to the precision and reliability of transmission at a glomerular synapse. *J Neurosci* 25(36):8173–8187.
28. Kim MH, Korogod N, Schneggenburger R, Ho WK, Lee SH (2005) Interplay between  $\text{Na}^+/\text{Ca}^{2+}$  exchangers and mitochondria in  $\text{Ca}^{2+}$  clearance at the calyx of Held. *J Neurosci* 25(26):6057–6065.
29. Collin T, et al. (2005) Developmental changes in parvalbumin regulate presynaptic  $\text{Ca}^{2+}$  signaling. *J Neurosci* 25(1):96–107.
30. Kaeser PS, Regehr WG (2014) Molecular mechanisms for synchronous, asynchronous, and spontaneous neurotransmitter release. *Annu Rev Physiol* 76:333–363.
31. Neher E (1998) Usefulness and limitations of linear approximations to the understanding of  $\text{Ca}^{++}$  signals. *Cell Calcium* 24(5-6):345–357.
32. Vanselow BK, Keller BU (2000) Calcium dynamics and buffering in oculomotor neurons from mouse that are particularly resistant during amyotrophic lateral sclerosis (ALS)-related motoneurone disease. *J Physiol* 525(Pt 2):433–445.
33. Habets RL, Borst JG (2006) An increase in calcium influx contributes to post-tetanic potentiation at the rat calyx of Held synapse. *J Neurophysiol* 96(6):2868–2876.
34. Xu T, Naraghi M, Kang H, Neher E (1997) Kinetic studies of  $\text{Ca}^{2+}$  binding and  $\text{Ca}^{2+}$  clearance in the cytosol of adrenal chromaffin cells. *Biophys J* 73(1):532–545.
35. Zhou Z, Neher E (1993) Mobile and immobile calcium buffers in bovine adrenal chromaffin cells. *J Physiol* 469:245–273.
36. Helmchen F, Imoto K, Sakmann B (1996)  $\text{Ca}^{2+}$  buffering and action potential-evoked  $\text{Ca}^{2+}$  signaling in dendrites of pyramidal neurons. *Biophys J* 70(2):1069–1081.
37. Matthews EA, Schoch S, Dietrich D (2013) Tuning local calcium availability: Cell-type-specific immobile calcium buffer capacity in hippocampal neurons. *J Neurosci* 33(36):14431–14445.
38. Maeda H, Ellis-Davies GC, Ito K, Miyashita Y, Kasai H (1999) Supralinear  $\text{Ca}^{2+}$  signaling by cooperative and mobile  $\text{Ca}^{2+}$  buffering in Purkinje neurons. *Neuron* 24(4):989–1002.
39. Sabatini BL, Oertner TG, Svoboda K (2002) The life cycle of  $\text{Ca}^{2+}$  ions in dendritic spines. *Neuron* 33(3):439–452.
40. Tank DW, Regehr WG, Delaney KR (1995) A quantitative analysis of presynaptic calcium dynamics that contribute to short-term enhancement. *J Neurosci* 15(12):7940–7952.
41. Babai N, Kochubey O, Keller D, Schneggenburger R (2014) An alien divalent ion reveals a major role for  $\text{Ca}^{2+}$  buffering in controlling slow transmitter release. *J Neurosci* 34(38):12622–12635.
42. Baimbridge KG, Celio MR, Rogers JH (1992) Calcium-binding proteins in the nervous system. *Trends Neurosci* 15(8):303–308.
43. Eggermann E, Jonas P (2012) How the 'slow'  $\text{Ca}^{2+}$  buffer parvalbumin affects transmitter release in nanodomain-coupling regimes. *Nat Neurosci* 15(1):20–22.
44. Faas GC, Schwaller B, Vergara JL, Mody I (2007) Resolving the fast kinetics of cooperative binding:  $\text{Ca}^{2+}$  buffering by calretinin. *PLoS Biol* 5(11):e311.
45. Schwaller B (2009) The continuing disappearance of "pure"  $\text{Ca}^{2+}$  buffers. *Cell Mol Life Sci* 66(2):275–300.
46. Gabso M, Neher E, Spira ME (1997) Low mobility of the  $\text{Ca}^{2+}$  buffers in axons of cultured Aplysia neurons. *Neuron* 18(3):473–481.
47. Vyleta NP, Jonas P (2014) Loose coupling between  $\text{Ca}^{2+}$  channels and release sensors at a plastic hippocampal synapse. *Science* 343(6171):665–670.
48. Edmonds B, Reyes R, Schwaller B, Roberts WM (2000) Calretinin modifies presynaptic calcium signaling in frog saccular hair cells. *Nat Neurosci* 3(8):786–790.
49. Pangrsić T, et al. (2015) EF-hand protein  $\text{Ca}^{2+}$  buffers regulate  $\text{Ca}^{2+}$  influx and exocytosis in sensory hair cells. *Proc Natl Acad Sci USA* 112(9):E1028–E1037.
50. Soler-Llavina GJ, Sabatini BL (2006) Synapse-specific plasticity and compartmentalized signaling in cerebellar stellate cells. *Nat Neurosci* 9(6):798–806.
51. Matveev V, Zucker RS, Sherman A (2004) Facilitation through buffer saturation: Constraints on endogenous buffering properties. *Biophys J* 86(5):2691–2709.
52. Chamberland S, Evstratova A, Tóth K (2014) Interplay between synchronization of multivesicular release and recruitment of additional release sites support short-term facilitation at hippocampal mossy fiber to CA3 pyramidal cells synapses. *J Neurosci* 34(33):11032–11047.
53. Hámori J, Somogyi J (1983) Differentiation of cerebellar mossy fiber synapses in the rat: A quantitative electron microscope study. *J Comp Neurol* 220(4):365–377.
54. Xu-Friedman MA, Regehr WG (2003) Ultrastructural contributions to desensitization at cerebellar mossy fiber to granule cell synapses. *J Neurosci* 23(6):2182–2192.
55. DiGregorio DA, Peskoff A, Vergara JL (1999) Measurement of action potential-induced presynaptic calcium domains at a cultured neuromuscular junction. *J Neurosci* 19(18):7846–7859.
56. Serulle Y, Sugimori M, Llinás RR (2007) Imaging synaptosomal calcium concentration microdomains and vesicle fusion by using total internal reflection fluorescent microscopy. *Proc Natl Acad Sci USA* 104(5):1697–1702.
57. Becherer U, Moser T, Stühmer W, Oheim M (2003) Calcium regulates exocytosis at the level of single vesicles. *Nat Neurosci* 6(8):846–853.
58. Frank T, Khimich D, Neef A, Moser T (2009) Mechanisms contributing to synaptic  $\text{Ca}^{2+}$  signals and their heterogeneity in hair cells. *Proc Natl Acad Sci USA* 106(11):4483–4488.
59. Svoboda K (2004) Do spines and dendrites distribute dye evenly? *Trends Neurosci* 27(8):445–446.
60. Schneggenburger R (2005)  $\text{Ca}^{2+}$  Uncaging in Nerve Terminals. *Imaging in Neuroscience and Development*, eds Yuste R, Konnerth A (Cold Spring Harbor Laboratory Press, Cold Spring Harbor, NY), pp 415–419.
61. Woehler A, Lin KH, Neher E (2014) Calcium-buffering effects of gluconate and nucleotides, as determined by a novel fluorimetric titration method. *J Physiol* 592(Pt 22):4863–4875.
62. Aponte Y, Bischofberger J, Jonas P (2008) Efficient  $\text{Ca}^{2+}$  buffering in fast-spiking basket cells of rat hippocampus. *J Physiol* 586(8):2061–2075.
63. Koch C (1999) *Biophysics of Computation Information Processing in Single Neurons* (Oxford Univ Press, New York).
64. Pan B, Zucker RS (2009) A general model of synaptic transmission and short-term plasticity. *Neuron* 62(4):539–554.
65. Meinrenken CJ, Borst JGG, Sakmann B (2002) Calcium secretion coupling at calyx of Held governed by nonuniform channel-vesicle topography. *J Neurosci* 22(5):1648–1667.
66. Schmidt H, et al. (2013) Nanodomain coupling at an excitatory cortical synapse. *Curr Biol* 23(3):244–249.
67. Matveev V, Sherman A, Zucker RS (2002) New and corrected simulations of synaptic facilitation. *Biophys J* 83(3):1368–1373.
68. Smith PD, Liesegang GW, Berger RL, Czerlinski G, Podolsky RJ (1984) A stopped-flow investigation of calcium ion binding by ethylene glycol bis(beta-aminoethyl ether)-N, N'-tetraacetic acid. *Anal Biochem* 143(1):188–195.
69. Naraghi M, Neher E (1997) Linearized buffered  $\text{Ca}^{2+}$  diffusion in microdomains and its implications for calculation of  $[\text{Ca}^{2+}]$  at the mouth of a calcium channel. *J Neurosci* 17(18):6961–6973.
70. Nägerl UV, Novo D, Mody I, Vergara JL (2000) Binding kinetics of calbindin-D(28k) determined by flash photolysis of caged  $\text{Ca}^{2+}$ . *Biophys J* 79(6):3009–3018.
71. Sheng J, et al. (2012) Calcium-channel number critically influences synaptic strength and plasticity at the active zone. *Nat Neurosci* 15(7):998–1006.
72. Ermolyuk YS, et al. (2012) Independent regulation of basal neurotransmitter release efficacy by variable  $\text{Ca}^{2+}$  influx and bouton size at small central synapses. *PLoS Biol* 10(9):e1001396.
73. Holderith N, et al. (2012) Release probability of hippocampal glutamatergic terminals scales with the size of the active zone. *Nat Neurosci* 15(7):988–997.
74. Scimemi A, Diamond JS (2012) The number and organization of  $\text{Ca}^{2+}$  channels in the active zone shapes neurotransmitter release from Schaffer collateral synapses. *J Neurosci* 32(50):18157–18176.
75. Wang LY, Neher E, Taschenberger H (2008) Synaptic vesicles in mature calyx of Held synapses sense higher nanodomain calcium concentrations during action potential-evoked glutamate release. *J Neurosci* 28(53):14450–14458.
76. Hallermann S, et al. (2010) Bassoon speeds vesicle reloading at a central excitatory synapse. *Neuron* 68(4):710–723.



### **3.3 Delvendahl et al. 2015 Front. Cell. Neurosci. 9, 93.**

Seite 38–45

# Dendritic patch-clamp recordings from cerebellar granule cells demonstrate electrotonic compactness

Igor Delvendahl\*, Isabelle Straub and Stefan Hallermann\*

Medical Faculty, Carl-Ludwig Institute for Physiology, University of Leipzig, Leipzig, Germany

## OPEN ACCESS

### Edited by:

Christian D. Wilms,  
University College London, UK

### Reviewed by:

Arnd Roth,  
University College London, UK  
Lisa Mapelli,  
University of Pavia, Italy

### \*Correspondence:

Igor Delvendahl and Stefan  
Hallermann, Medical Faculty,  
Carl-Ludwig-Institute for Physiology,  
University of Leipzig, Liebigstr. 27  
04103 Leipzig, Germany  
igor.delvendahl@  
medizin.uni-leipzig.de;  
hallermann@medizin.uni-leipzig.de

**Received:** 13 October 2014

**Accepted:** 28 February 2015

**Published:** 19 March 2015

### Citation:

Delvendahl I,  
Straub I and Hallermann S (2015)  
Dendritic patch-clamp recordings  
from cerebellar granule cells  
demonstrate electrotonic  
compactness.  
*Front. Cell. Neurosci.* 9:93.  
doi: 10.3389/fncel.2015.00093

Cerebellar granule cells (GCs), the smallest neurons in the brain, have on average four short dendrites that receive high-frequency mossy fiber inputs conveying sensory information. The short length of the dendrites suggests that GCs are electrotonically compact allowing unfiltered integration of dendritic inputs. The small average diameter of the dendrites ( $\sim 0.7 \mu\text{m}$ ), however, argues for dendritic filtering. Previous studies based on somatic recordings and modeling indicated that GCs are electrotonically extremely compact. Here, we performed patch-clamp recordings from GC dendrites in acute brain slices of mice to directly analyze the electrotonic properties of GCs. Strikingly, the input resistance did not differ significantly between dendrites and somata of GCs. Furthermore, spontaneous excitatory postsynaptic potentials (EPSP) were similar in amplitude at dendritic and somatic recording sites. From the dendritic and somatic input resistances we determined parameters characterizing the electrotonic compactness of GCs. These data directly demonstrate that cerebellar GCs are electrotonically compact and thus ideally suited for efficient high-frequency information transfer.

**Keywords:** granule cell, dendrites, cerebellum, patch-clamp techniques, electrophysiology

## Introduction

Synaptic information transfer is strongly determined by the electrotonic properties of the postsynaptic neuron and the location of the synapse within the neuron. Dendrites receiving synaptic input provide the backbone for the computation performed by neurons (Magee, 2000; Abbott and Regehr, 2004; Gullledge et al., 2005; London and Häusser, 2005; Spruston, 2008). The morphology and passive properties of dendrites critically influence the processing of synaptic inputs (Jack et al., 1983; Mainen and Sejnowski, 1996; Segev and London, 2000; Schaefer et al., 2003; Abrahamsson et al., 2012). Thus, knowledge about the electrical properties of dendrites is crucial for our understanding of information transfer and computation in the central nervous system.

Cerebellar granule cells (GCs) are the most numerous neurons in the brain (Williams and Herrup, 1988) and compose the majority of the input layer of the cerebellar cortex (Billings et al., 2014). GCs have small somata and, on average, four short dendrites (Palkovits et al., 1972; Palay and Chan-Palay, 1974). The dendrites end with claw-like shaped digits (DiGregorio et al., 2007), which receive excitatory mossy fiber input in cerebellar glomeruli (D'Angelo et al., 1990; Silver et al., 1992). A glomerulus is formed

by a single presynaptic mossy fiber bouton, Golgi cell axons, and dendrites of more than 10 GCs (Jakab and Hámori, 1988; Billings et al., 2014; Ritzau-Jost et al., 2014). GCs integrate the broad-bandwidth sensory information conveyed by mossy fiber inputs, transforming it into higher dimensional, sparser code (Marr, 1969; Billings et al., 2014). Thus, the anatomical structure of the GC layer is optimal for pattern separation (Olshausen and Field, 2004), which is important for network functions such as adaptive filtering (Fujita, 1982; Dean et al., 2010) and associative learning (D'Angelo and De Zeeuw, 2009).

Regarding the electrical properties of cerebellar GCs, previous studies based on somatic recordings and modeling indicated that these small neurons are electrotonically compact (Silver et al., 1992; D'Angelo et al., 1993; Gabbiani et al., 1994), thus affording good somatic voltage-clamp. Consequently, GC soma and dendrites are generally assumed to form a single electrical compartment, thereby acting as a point neuron (Billings et al., 2014). In recent years, direct patch-clamp recordings from dendrites have significantly advanced our understanding of many neurons' electrical properties and their signaling (see e.g., Stuart and Sakmann, 1994; Nevian et al., 2007; Hu et al., 2010). The electrotonic properties of the small GC dendrites, however, have not been directly determined. In particular, passive membrane properties of GC dendrites such as the input resistance and their relation to somatic values remain unclear. Furthermore, model predictions critically depend on the diameter of dendrites, which is difficult to measure. Here, we establish whole-cell patch-clamp recordings from GC dendrites to directly determine their electrotonic properties. We compare the input resistance and measure spontaneous excitatory postsynaptic potentials (EPSP) at dendritic and somatic recording sites. Our experimental findings provide direct evidence for the electrotonic compactness of GCs.

## Materials and Methods

### Electrophysiology

Cerebellar slices were prepared from mature ( $P37 \pm 3$ , range P22–P98) CD-1 or C57BL/6 mice of either sex. Animals were bred in the animal facility of the Medical Faculty of the University of Leipzig, and treated in accordance with the German Protection of Animals Act (TierSchG §4 Abs. 3) and with the guidelines for the welfare of experimental animals issued by the European Communities Council Directive of 24. November 1986 (86/609/EEC). The local authorities approved the experiments (Landesdirektion Leipzig, registration number T86/13). Mice were housed in a 12 h light/dark cycle with food and water ad libitum. Animals were lightly anesthetized with isoflurane (Baxter, Deerfield, IL) before being killed by rapid decapitation. The cerebellar vermis was quickly removed and mounted in a chamber filled with chilled extracellular solution. Parasagittal 300- $\mu\text{m}$  slices were cut using a Leica VT1200 microtome (Leica Microsystems, Wetzlar, Germany), transferred to an incubation chamber at  $\sim 35^\circ\text{C}$  for 30 min and subsequently stored at room temperature. Artificial cerebrospinal fluid (ACSF) was used for slice cutting, storage, and experiments.

ACSF contained (in mM): 125 NaCl, 25  $\text{NaHCO}_3$ , 2.5 KCl, 1.25  $\text{NaH}_2\text{PO}_4$ , 2  $\text{CaCl}_2$ , 1  $\text{MgCl}_2$ , 20 Glucose ( $\sim 310$  mOsm, pH 7.3 when bubbled with Carbogen (5%  $\text{O}_2/95\%$   $\text{CO}_2$ )). Patch pipettes were pulled from borosilicate glass (Science Products, Hofheim, Germany) using a DMZ Puller (Zeitz-Instruments, Martinsried, Germany). Patch pipettes had open-tip resistances of 9–14  $\text{M}\Omega$  or 14–18  $\text{M}\Omega$  for somatic and dendritic recordings, respectively. The intracellular solution contained (in mM): 150 K-gluconate, 10 NaCl, 10 K-HEPES, 3 Mg-ATP, 0.3 Na-GTP (300–305 mOsm, pH adjusted to 7.3 with KOH). In addition, the intracellular solution contained 10–20  $\mu\text{M}$  of the fluorescence dye Atto594. Experiments were performed at  $35\text{--}37^\circ\text{C}$  and slices were continuously superfused with ACSF. Atto594 was obtained from Atto-Tec (Atto-Tec, Siegen, Germany); all other chemicals were purchased from Sigma-Aldrich (St. Louis, MO).

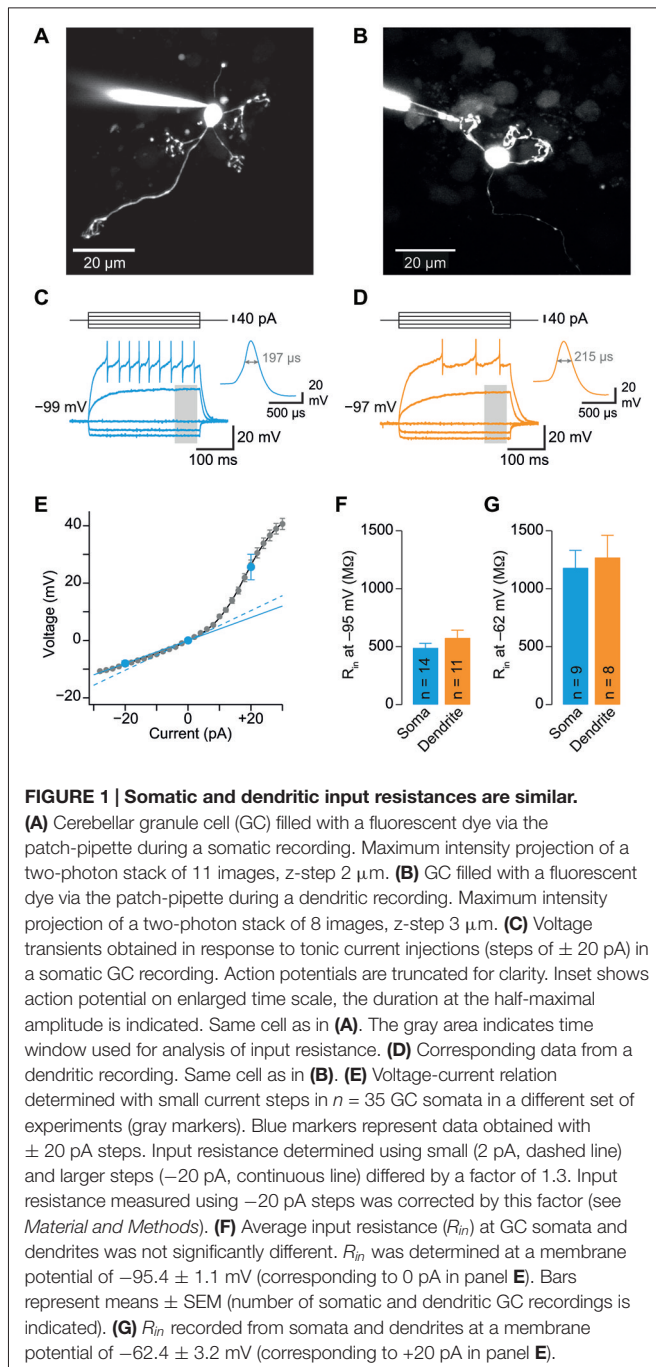
Cerebellar GCs were visualized with oblique infrared illumination and were identified as previously described (Silver et al., 1996). For dendritic recordings, putative cerebellar glomeruli were approached with patch-pipettes. In 12 out of >700 attempts, a whole-cell recording could be established at a GC dendrite. Dendritic recording sites were confirmed by two-photon imaging of the GC filled with Atto594 via the dendrite (Figure 1B). Patch-clamp recordings were made using a HEKA EPC10/2 USB amplifier (HEKA Elektronik, Lambrecht/Pfalz, Germany). Data were sampled at 200 kHz. Measurements were corrected for a liquid junction potential of +13 mV. Series resistance ranged from 20–57  $\text{M}\Omega$  for somatic recordings (mean  $36.6 \pm 2.4$   $\text{M}\Omega$ ), and from 42–155  $\text{M}\Omega$  for recordings from GC dendrites (mean  $88.7 \pm 16.9$   $\text{M}\Omega$ ).

### Two-photon Imaging

We used a Femto2D laser-scanning microscope (Femtonics, Budapest, Hungary) for imaging. Two-photon excitation was performed with a MaiTai femtosecond pulsed Ti:Sapphire laser (SpectraPhysics, Santa Clara, CA) tuned to 810 nm. Both reflected and transmitted fluorescence were collected by the imaging setup with a 60 $\times$  water-immersion objective (Olympus, NA 1.0) and an oil-immersion condenser (Olympus, NA 1.4), respectively. Imaging data were acquired and processed using MES software (Femtonics). Stacks of two-photon images covering 20–50  $\mu\text{m}$  in  $z$ -dimension were obtained. Diameters of GC dendrites and somata were measured as full-width at half-maximum of intensity line profiles made perpendicular to the dendrite or soma, respectively, in maximum  $z$ -projections of image stacks. Dendrite length was measured as  $xyz$ -distance in image stacks using MES software.

### Data Analysis

Input resistance ( $R_{in}$ ) was calculated from voltage deflections in response to tonic current injection ( $-20$  pA, duration 300 ms). Voltage was calculated as mean over 60 ms at steady-state. In a separate set of experiments, the subthreshold current-voltage relationship was determined with small current steps ( $\pm 2$  pA) in order to characterize the dependence of  $R_{in}$  on the amplitude of current injection. As previously reported (D'Angelo et al.,



1995; Cathala et al., 2003), GCs exhibited outward and inward rectification (**Figure 1E**). Consequently, the data obtained with  $-20$  pA current steps were corrected for by using the slope at 0 pA of a sum of a sigmoid and a linear function fit to the data, resulting in a correction factor of 1.3 (**Figure 1E**). Spontaneous EPSP were detected with a template matching routine implemented in NeuroMatic software.<sup>1</sup> For analysis of 20–80% rise times and decay time constants of EPSPs, data were filtered to avoid distortions of the kinetics measurements

<sup>1</sup><http://www.neuromatic.thinkrandom.com>

by noise. Statistical analysis was performed using unpaired or paired  $t$ -tests. Level of statistical significance was set at  $p < 0.05$ . Data are expressed as mean  $\pm$  SEM except where stated.

## Modeling

To determine the electrotonic properties of GCs from the somatic and dendritic input resistance, the following approach was used: GCs were represented by a spherical soma with radius,  $a_{\text{soma}}$ , an axon with radius,  $a_{\text{axon}}$ , and four cylindrical dendrites with radius,  $a_{\text{dend}}$  (**Figure 3A**). Dendritic claws were not included as additional compartments, because their diameter does not exceed the diameter of the parent dendrite (Jakab and Hámori, 1988; DiGregorio et al., 2002). The resulting somatic input conductance,  $g_{\text{somatic}}$ , is:

$$g_{\text{somatic}} = g_{\text{soma}} + 4g_{\text{dendrite}} + g_{\text{axon}} \quad (1)$$

where  $g_{\text{soma}}$ ,  $g_{\text{axon}}$ , and  $g_{\text{dendrite}}$  are the input conductance of an isolated soma, isolated axon, and a single isolated dendrite, respectively.  $g_{\text{soma}}$  is calculated as:

$$g_{\text{soma}} = \frac{1}{R_m} 4\pi a_{\text{soma}}^2 \quad (2)$$

where  $R_m$  is the specific membrane resistance.  $g_{\text{dendrite}}$  is calculated as the input conductance of a finite cable (Rall, 1969; Jack et al., 1983):

$$g_{\text{dendrite}} = \frac{\tanh L}{r_a \lambda} \quad (3)$$

where  $L$  is the electrotonic length of the dendrites,  $r_a$  is the intracellular resistance to axial flow of current along the cylinder, and  $\lambda$  is the membrane length constant defined as:

$$L = \frac{l}{\lambda} \quad (4)$$

where  $l$  is the length of the dendrite,

$$r_a = \frac{R_i}{\pi a_{\text{dend}}^2} \quad (5)$$

where  $R_i$  is the intracellular resistivity, and

$$\lambda = \sqrt{R_m a_{\text{dend}} / 2R_i} \quad (6)$$

$g_{\text{axon}}$  is calculated as the input conductance of a finite cable, accordingly.

First,  $R_m$  was calculated to obtain the measured somatic input resistance as a function of dendrite diameter ( $= 2a_{\text{dend}}$ ; **Figure 3B**) by numerically solving equation (1) for  $R_m$  (using the FindRoot function of Mathematica). Note, that the three remaining parameters were measured ( $a_{\text{soma}}$  and  $l$ ) or taken from the literature ( $R_i$ , Silver et al., 1992; Gabbiani et al., 1994; Cathala et al., 2003). In addition, two parameters describing the electrotonic compactness of neurons were plotted as a function of dendritic diameter: The above defined electrotonic length of the dendrites,  $L$ , and the dendrite-to-soma conductance ratio,  $\rho$  (also referred to as

dendritic dominance), defined as (Rall, 1969; Jack et al., 1983):

$$\rho = \frac{4g_{\text{dend}}}{g_{\text{soma}}} \quad (7)$$

Finally, the predicted dendritic input resistance was calculated using the NEURON simulation environment (Carnevale and Hines, 2006). A multi-compartment cylinder ( $n_{\text{seg}} = 20$ ) with radius  $a_{\text{soma}}$  and length  $2a_{\text{soma}}$  represented the soma; the axon was represented by a multi-compartment cylinder ( $n_{\text{seg}} = 20$ ) with radius  $a_{\text{axon}} = 0.09 \mu\text{m}$  (Sultan, 2000) and length  $300 \mu\text{m}$ . Increasing the length of the axon had marginal impact on the results. Four cylinders with radius  $a_{\text{dend}}$  and length  $l$  represented the dendrites (see **Table 1**;  $n_{\text{seg}} = 20$ ). Membrane capacitance ( $C_m$ ) was  $0.9 \mu\text{F cm}^{-2}$ . For each dendritic diameter,  $R_m$  of the NEURON model was set to a value ensuring the correct somatic input resistance. Current injection at the soma resulted in voltage deflections at the soma consistent with the calculated somatic input resistance. Current injection at the tip of one dendrite resulted in voltage deflections at the tip of the dendrite from which the dendritic input resistance was calculated.

## Results

### Somatic and Dendritic Input Resistances are Similar

To investigate the electrotonic properties of cerebellar GCs, we performed direct patch-clamp recordings from GC somata and dendrites (**Figures 1A,B**). For dendritic recordings, putative cerebellar glomeruli containing mossy fiber boutons and dendrites of GCs were approached with patch pipettes. After establishing the whole-cell configuration, GCs were unequivocally identified by the following two criteria: (1) In contrast to presynaptic mossy fiber terminals, which fire a single action potential upon current injection (Rancz et al., 2007;

Ritzau-Jost et al., 2014), GCs display distinctive repetitive firing (Cathala et al., 2003); and (2) The dendritic recording site was verified by including a fluorescence dye (Atto594) in the patch pipette and using two-photon imaging (**Figure 1B**). Interestingly, in 5 out of 12 GCs the axon originated from the dendrite (Thome et al., 2014). In all our experiments, the dendritic recording site was located at the distal part of the dendrites with an average distance from the soma of  $20.7 \pm 2.9 \mu\text{m}$  ( $n = 11$ ; range:  $11\text{--}42 \mu\text{m}$ ; **Table 1**). Thus, our data show that direct patch-clamp recordings from the small dendrites of cerebellar GCs are feasible.

We compared the input resistance ( $R_{in}$ ) of somatic and dendritic recordings to investigate the electrotonic compactness of GCs. Analysis of the spatial distribution of  $R_{in}$  alone is necessary, but not sufficient to make conclusions on electrical compactness of neuronal structures. In our case, however, the length of dendrites is known, which allows investigating the electrical compactness of GCs with additional knowledge of  $R_{in}$ . We determined  $R_{in}$  in current-clamp mode using 300-ms long hyperpolarizing current steps of  $-20 \text{ pA}$  (**Figures 1C,D**). Because  $R_{in}$  depends on the amount of current injection (D'Angelo et al., 1995; Cathala et al., 2003), we also determined the voltage-current relation in a separate set of GC somatic recordings using smaller ( $\pm 2 \text{ pA}$ ) current steps. These data were fit with the sum of a sigmoid and a linear function. From this fit,  $R_{in}$  was determined as the slope at  $0 \text{ pA}$ , which was 1.3-fold higher than  $R_{in}$  calculated from  $-20 \text{ pA}$  step current injections (**Figure 1E**, blue lines). Therefore,  $R_{in}$  values measured in somatic and dendritic recordings using  $-20 \text{ pA}$  current injection were corrected accordingly (cf. *Material and Methods*). Interestingly,  $R_{in}$  was not significantly different at dendritic and somatic recording sites (soma:  $0.49 \pm 0.04 \text{ G}\Omega$ ; dendrite:  $0.58 \pm 0.07 \text{ G}\Omega$ ;  $p = 0.24$ , unpaired  $t$ -test; **Figure 1F**; **Table 1**). Also,  $R_{in}$  in our somatic measurements was comparable to values previously reported for P39 mice (Cathala et al., 2003) and adult cats (Jörntell and Ekerot, 2006), but lower than previously determined in young rats (D'Angelo et al., 1993, 1995; Silver et al., 1996; Prestori et al., 2013). Cerebellar GCs show pronounced inward rectification ((D'Angelo et al., 1995; Cathala et al., 2003), cf. **Figures 1C,D,F**), which could impact the  $R_{in}$  measurements with hyperpolarizing current steps. When analyzing  $R_{in}$  with depolarizing current steps of  $+20 \text{ pA}$ , we obtained higher values, which were again similar in somatic and dendritic recordings (soma:  $1.18 \pm 0.15 \text{ G}\Omega$ ; dendrite:  $1.27 \pm 0.19 \text{ G}\Omega$ , **Figure 1G**; **Table 1**). These data directly demonstrate that the distal part of the dendrites of GCs has similar  $R_{in}$  compared to the soma. Furthermore, the membrane time constant ( $\tau_m$ ) determined with hyperpolarizing current injections was comparable for somatic and dendritic recordings (soma:  $1.4 \pm 0.12 \text{ ms}$ , dendrite:  $1.63 \pm 0.17 \text{ ms}$ ;  $p = 0.25$ , unpaired  $t$ -test).

**TABLE 1 | Parameters of GCs.**

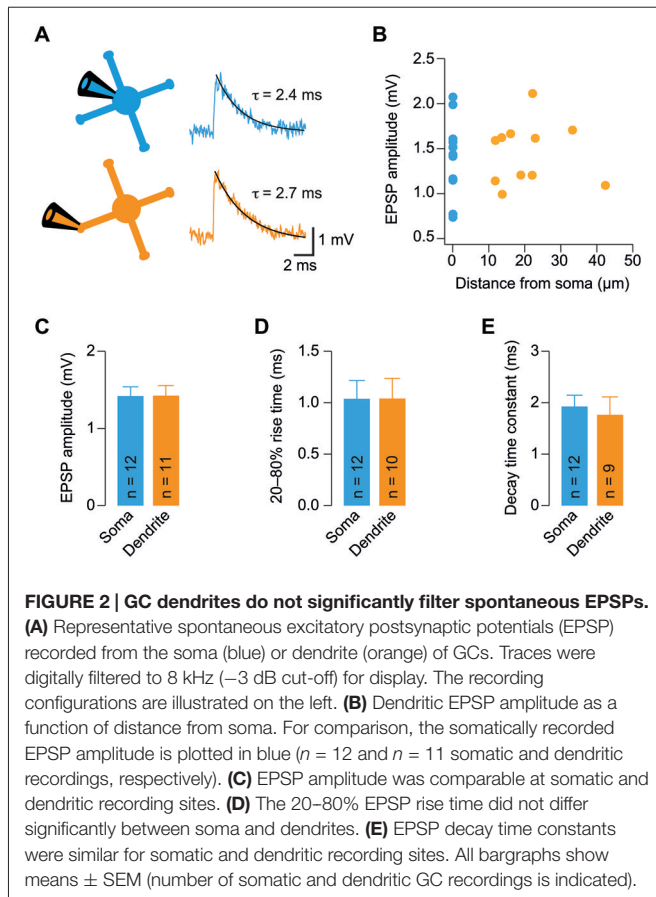
Parameter	Value	Method
Somatic $R_{in}$ at $-95 \text{ mV}$ ( $\text{M}\Omega$ )	$492 \pm 37$ ( $n = 14$ )	patch-clamp recording
Dendritic $R_{in}$ at $-95 \text{ mV}$ ( $\text{M}\Omega$ )	$578 \pm 65$ ( $n = 11$ )	patch-clamp recording
Somatic $R_{in}$ at $-62 \text{ mV}$ ( $\text{M}\Omega$ )	$1182 \pm 150$ ( $n = 9$ )	patch-clamp recording
Dendritic $R_{in}$ at $-62 \text{ mV}$ ( $\text{M}\Omega$ )	$1273 \pm 189$ ( $n = 8$ )	patch-clamp recording
Soma diameter ( $\mu\text{m}$ )	$5.9 \pm 0.3$ ( $n = 11$ )	two-photon imaging
Dendrite length ( $\mu\text{m}$ )	$20.7 \pm 2.9$ ( $n = 11$ )	two-photon imaging
Dendrite diameter ( $\mu\text{m}$ )	$0.69 \pm 0.3$ ( $n = 10$ )	two-photon imaging
Dendrite diameter ( $\mu\text{m}$ )	$0.52$ ( $0.40\text{--}1.02$ )	<b>Figure 3C</b>
$R_m$ ( $\text{k}\Omega\text{cm}^2$ )	$1.42$ ( $1.25\text{--}2.12$ )	<b>Figure 3C</b>
$\rho$	$1.23$ ( $0.93\text{--}2.43$ )	<b>Figure 3C</b>
$L$	$0.15$ ( $0.09\text{--}0.19$ )	<b>Figure 3C</b>

Summary of determined GC parameters (mean  $\pm$  SEM, or mean with 16–84% confidence interval in brackets). The input resistance ( $R_{in}$ ) was obtained with somatic or direct dendritic patch-clamp recordings. The diameter of the soma and the length of the dendrites were measured from stacks of two-photon images. The diameter of the dendrites, the specific membrane resistance ( $R_m$ ), the dendrite-to-soma conductance ratio ( $\rho$ ) and the electrotonic length of the dendrites ( $L$ ) were determined in **Figure 3C**.

### GC Dendrites do not Significantly Filter Spontaneous EPSPs

The similar  $R_{in}$  of soma and dendrites suggests that GCs are electrotonically compact. To further investigate this hypothesis, we measured spontaneous EPSPs in GC somata and dendrites.





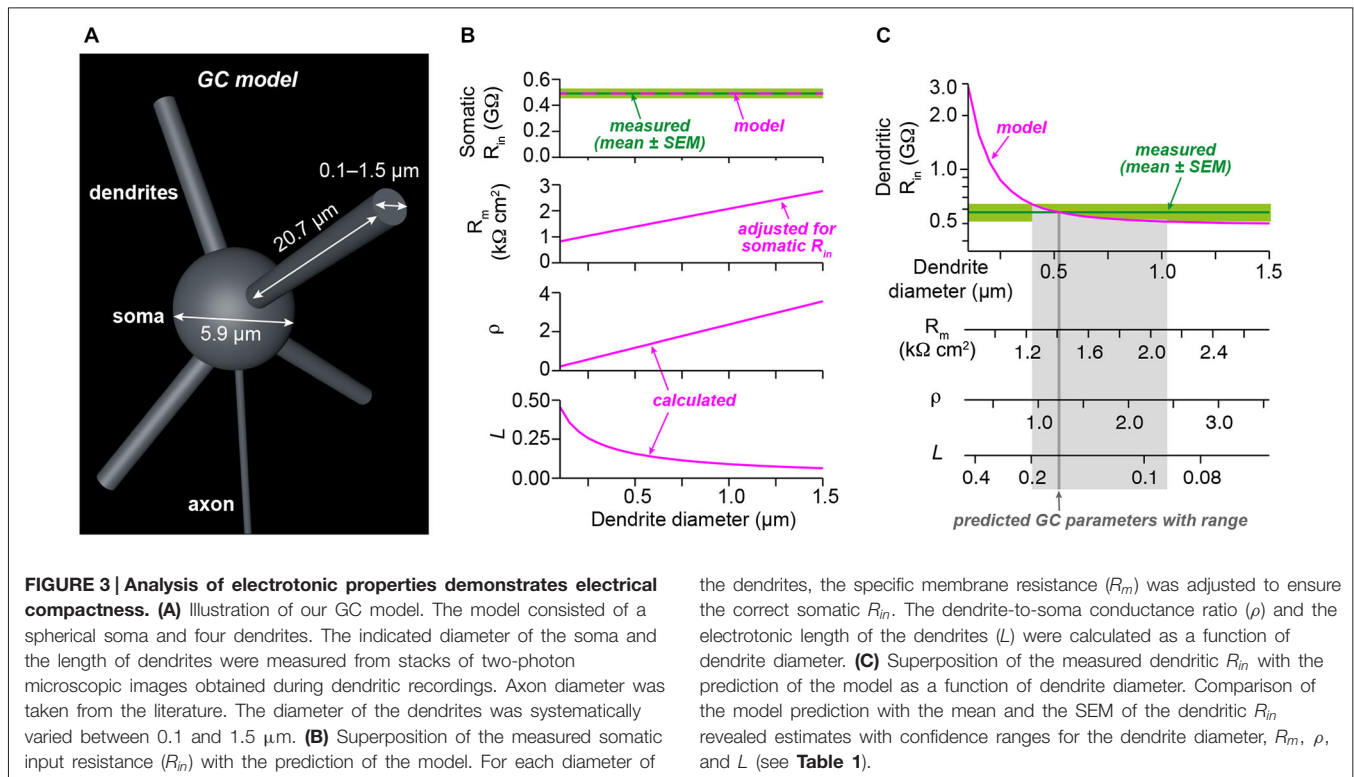
We observed spontaneous EPSPs (Figure 2A) at a mean frequency of  $0.85 \pm 0.16$  Hz and  $1.19 \pm 0.22$  Hz in somatic and dendritic recordings, respectively, consistent with previous reports (Cathala et al., 2003; Hallermann et al., 2010). The amplitude of spontaneous EPSPs of GCs did not display a strong dependence on distance of dendritic recording sites from the soma (Figure 2B). Accordingly, the mean amplitude of spontaneous EPSPs was not significantly different between somatic and dendritic recording sites ( $p = 0.98$ , unpaired  $t$ -test; Figure 2C). In addition, the rise times and decay time constants of spontaneous EPSPs were comparable at the two distinct recording sites (20–80% rise time:  $1.04 \pm 0.18$  ms vs.  $1.04 \pm 0.19$  ms,  $n = 12$  and  $10$ ,  $p = 0.99$ ; decay time constant:  $1.9 \pm 0.2$  ms vs.  $1.8 \pm 0.4$  ms,  $n = 12$  and  $9$ ,  $p = 0.68$ ; for somatic and dendritic recordings, respectively, unpaired  $t$ -tests; Figures 2D,E). When recording from a dendrite, some EPSPs will be locally generated and the rest originate from the remaining three dendrites. However, we did not observe an increased heterogeneity of the EPSP amplitude during the dendritic recordings (dendritic vs. somatic coefficient of variation, CV = mean/SD: 50.4% vs. 61.4%) and the variability of kinetic parameters was comparable (20–80% rise time dendritic vs. somatic CV: 111.4% vs. 91.8%; decay time constant dendritic vs. somatic CV: 93.4% vs. 76.8%). These results indicate that dendrites do not filter EPSPs in GCs to a large extent.

## Analysis of Electrotonic Properties Demonstrates Electrical Compactness

We next determined the electrotonic properties of GCs by analyzing the measured somatic and dendritic input resistance using analytical calculations and numerical modeling implemented in NEURON (Carnevale and Hines, 2006). GCs were modeled by a spherical soma with a cylindrical axon and four cylindrical dendrites (Figure 3A). The somatic input resistance of this simplified GC can be calculated analytically (Equation 1, *Material and Methods*) and depends on the diameter of the soma, the length and diameter of the axon and dendrites, the intracellular resistivity, and the specific membrane resistance. These values were determined as described in the following: The soma diameter and dendrite length were measured from image stacks of GCs filled with Atto594 during dendritic recordings. In these experiments, the mean GC soma diameter was  $5.9 \mu\text{m}$  and the mean length of GC dendrites, which were recorded from, was  $20.7 \mu\text{m}$  (Table 1). The intracellular resistivity is similar across cell types and was set at previously estimated values from cerebellar GCs ( $100 \Omega\text{cm}$ ; Silver et al., 1992; Gabbiani et al., 1994; Cathala et al., 2003). The axon diameter was taken from the literature ( $0.18 \mu\text{m}$ , Sultan, 2000) and its length was set at  $300 \mu\text{m}$ . The two remaining parameters—the diameter of the dendrites and the membrane resistance—are more difficult to measure. Since the diameter of GC dendrites is not exactly known and has a strong influence on the input resistance, we systematically varied the diameter of the dendrites in our GC model. We set the specific membrane resistance ( $R_m$ ) at a value that ensured that the model predicted our measured somatic  $R_{in}$  of  $492 \text{ M}\Omega$  for each dendrite diameter (Figure 3B, upper two graphs; cf. *Material and Methods*). We then calculated two parameters describing the electrotonic properties of GCs: the dendrite-to-soma conductance ratio,  $\rho$  (also referred to as dendritic dominance), and the electrotonic length of the dendrites,  $L$  (Rall, 1969).  $\rho$  increased with dendrite diameter (Figure 3B), corresponding to a larger contribution of the dendrites to  $R_{in}$ . Also,  $L$  decreased with increasing dendrite diameter (Figure 3B), corresponding to increased electrotonic compactness and thus a convergence to a single compartment (which would have  $L = 0$ ).

Based on these results, the measured dendritic  $R_{in}$  was used to determine the average properties of our GCs. Therefore, we first determined the dendritic  $R_{in}$  in our model as a function of dendrite diameter (Figure 3C, top graph; see *Material and Methods*). Comparison with the measured dendritic  $R_{in}$  of  $578.1 \pm 64.9 \text{ M}\Omega$  revealed that our GCs are best characterized by a dendritic diameter of  $0.52 \mu\text{m}$ . In our two-photon images, the patched GC dendrites had an average diameter of  $0.69 \pm 0.03 \mu\text{m}$  ( $n = 11$ , range  $0.5\text{--}0.8 \mu\text{m}$ ). Taking into account the limited spatial resolution of two-photon microscopy, these values seem consistent. According to the relations shown in Figure 3B, the comparison of the model prediction and the measured dendritic  $R_{in}$  revealed an  $R_m$  of  $1.4 \text{ k}\Omega\text{cm}^2$ ,  $\rho$  of  $1.23$ , and  $L$  of  $0.15$  (Figure 3C; see Table 1). These results and in particular the small electrotonic length of the dendrites demonstrate that GCs are electrotonically very compact.





We also used the measured membrane time constant as independent constraint in our simulations. To this end, we compared the measured membrane time constant with the one predicted by the model resulting in a graph comparable to **Figure 3C** (data not shown). This analysis yielded a dendrite diameter estimate of 0.69  $\mu\text{m}$ ,  $R_m$  of 1.7  $\text{k}\Omega\text{cm}^2$ ,  $\rho$  of 1.64, and  $L$  of 0.12. These values are very similar to the approach based on  $R_{in}$ , providing independent support for our conclusion of electronics compactness of GCs.

As described above, our measurements of  $R_{in}$  might be influenced by the inward rectification present in GCs (cf. **Figure 1**). We therefore repeated the simulations as in **Figures 3B,C** with the higher  $R_{in}$  values obtained from +20 pA current steps (cf. **Figure 1G**). The resulting estimates were dendrite diameter 0.52  $\mu\text{m}$ ,  $R_m = 3.7 \text{ k}\Omega\text{cm}^2$ ,  $\rho = 1.23$ , and  $L = 0.10$ , again indicating that GCs can be considered as electrotonically very compact.

## Discussion

In this study, we established dendritic patch-clamp recordings from GC dendrites, which have a thin diameter of  $\sim 0.7 \mu\text{m}$  (Eccles et al., 1967). To the best of our knowledge, these are the thinnest dendrites recorded from. Dendritic recordings have been performed at other thin dendrites, such as the basal dendrites of layer 5 pyramidal neurons with a diameter of  $\sim 1.9 \mu\text{m}$  (Nevian et al., 2007), or dendrites of hippocampal basket cells with a diameter of  $\sim 1.4 \mu\text{m}$

(Hu et al., 2010; Nörenberg et al., 2010). We exploited this technique to directly investigate the passive electrical properties of GCs.

## Electrical Compactness of Cerebellar CGs

Previous studies using somatic recordings in rats indicated that GCs are electrotonically very compact (Silver et al., 1992; D'Angelo et al., 1993). In these two studies, the values for the dendrite-to-soma conductance ratio ( $\rho$ ) were 0.98 and  $\leq 0.5$  (upper boundary), respectively. The electrotonic length of the dendrites ( $L$ ) was determined as 0.05 and 0.04. These figures are slightly smaller than our estimates in mice of 1.23 for  $\rho$  and 0.15 for  $L$  (**Figure 3**; **Table 1**). Furthermore, the specific membrane resistance  $R_m$  was previously estimated as 16  $\text{k}\Omega\text{cm}^2$  (Silver et al., 1992), whereas our estimate was 1.4  $\text{k}\Omega\text{cm}^2$ . Species and recording temperature differences could contribute to these discrepancies and may also explain why in our experiments at physiological temperature (35–37°C),  $R_{in}$  was lower than previous estimates (D'Angelo et al., 1993, 1995; Brickley et al., 2001). In addition, the developmental state of the animals could be a reason, because pronounced changes in the morphological properties of GC and their membrane properties during development have previously been described (Cathala et al., 2003). For example,  $R_m$  was decreased from 9.2  $\text{k}\Omega\text{cm}^2$  in P8 to 2.6  $\text{k}\Omega\text{cm}^2$  in P39 mice (Cathala et al., 2003). Note, that our mice had an average age of P37, but previous studies used rats of age P10–P22 (Silver et al., 1992; D'Angelo et al., 1993). Nevertheless, the compactness of GCs was confirmed when using higher  $R_{in}$  values for our analyses (see *Results*). Thus,

our dendritic recordings strongly support the previous studies analyzing the electrotonic compactness of GCs. Furthermore, the low  $R_m$  of cerebellar GCs will contribute to a fast time course of EPSPs and facilitate rapid action potential initiation (Nörenberg et al., 2010). Consistent with the spatially uniform  $R_{in}$  and electrotonic compactness, spontaneous EPSPs recorded at the soma and the dendrites were similar (Figure 2). Thus, our data indicate that cerebellar GCs are electrotonically extremely compact.

## Functional Implications

The electrotonic compactness allows GCs to rapidly and precisely integrate the fast EPSCs originating from mossy fiber activation (Silver et al., 1992; Cathala et al., 2005; Sargent et al., 2005) and to process high-frequency inputs (Saviane and Silver, 2006; Rancz et al., 2007; Ritzau-Jost et al., 2014). Furthermore, their compactness enables GCs to compare mossy fiber inputs independent of the distance of the synaptic site from the soma. Some less compact neurons with longer dendrites receive stronger inputs at distal parts of the dendrites (Magee and Cook,

2000) or express dendritic hyperpolarization-activated currents (Williams and Stuart, 2000) to counterbalance dendritic filtering of EPSPs. On the other hand, dendritic filtering might have the advantage to encode the spatial information of synaptic inputs (Rall, 1964). For GCs, however, this would not be of any benefit, because these neurons receive excitatory inputs only at the end of their dendrites. Furthermore, electrotonic compactness likely represents an important factor for the relay function of cerebellar GCs (Chadderton et al., 2004), which efficiently signal to postsynaptic stellate and Purkinje cells (Crowley et al., 2007; Valera et al., 2012), and thereby contribute to rapid cerebellar signaling (Blot and Barbour, 2014; Chen et al., 2014).

## Conclusion

In summary, our dendritic patch-clamp recordings demonstrate that dendrites of cerebellar GCs have a low dendritic dominance and short electrotonic length. Thus, GCs are electrotonically very compact, which seems ideally suited to rapidly process the high-frequency inputs arriving in the cerebellar cortex.

## References

- Abbott, L. F., and Regehr, W. G. (2004). Synaptic computation. *Nature* 431, 796–803. doi: 10.1038/nature03010
- Abrahamsson, T., Cathala, L., Matsui, K., Shigemoto, R., and DiGregorio, D. A. (2012). Thin dendrites of cerebellar interneurons confer sublinear synaptic integration and a gradient of short-term plasticity. *Neuron* 73, 1159–1172. doi: 10.1016/j.neuron.2012.01.027
- Billings, G., Piasini, E., Lorincz, A., Nusser, Z., and Silver, R. A. (2014). Network structure within the cerebellar input layer enables lossless sparse encoding. *Neuron* 83, 960–974. doi: 10.1016/j.neuron.2014.07.020
- Blot, A., and Barbour, B. (2014). Ultra-rapid axon-axon ephaptic inhibition of cerebellar Purkinje cells by the pinceau. *Nat. Neurosci.* 17, 289–295. doi: 10.1038/nn.3624
- Brickley, S. G., Revilla, V., Cull-Candy, S. G., Wisden, W., and Farrant, M. (2001). Adaptive regulation of neuronal excitability by a voltage-independent potassium conductance. *Nature* 409, 88–92. doi: 10.1038/35051086
- Carnevale, N. T., and Hines, M. L. (2006). *The NEURON Book*. Cambridge: Cambridge University Press.
- Cathala, L., Brickley, S., Cull-Candy, S., and Farrant, M. (2003). Maturation of EPSCs and intrinsic membrane properties enhances precision at a cerebellar synapse. *J. Neurosci.* 23, 6074–6085.
- Cathala, L., Holderith, N. B., Nusser, Z., DiGregorio, D. A., and Cull-Candy, S. G. (2005). Changes in synaptic structure underlie the developmental speeding of AMPA receptor-mediated EPSCs. *Nat. Neurosci.* 8, 1310–1318. doi: 10.1038/nn1534
- Chadderton, P., Margrie, T. W., and Häusser, M. (2004). Integration of quanta in cerebellar granule cells during sensory processing. *Nature* 428, 856–860. doi: 10.1038/nature02442
- Chen, C. H., Fremont, R., Arteaga-Bracho, E. E., and Khodakhah, K. (2014). Short latency cerebellar modulation of the basal ganglia. *Nat. Neurosci.* 17, 1767–1775. doi: 10.1038/nn.3868
- Crowley, J. J., Carter, A. G., and Regehr, W. G. (2007). Fast vesicle replenishment and rapid recovery from desensitization at a single synaptic release site. *J. Neurosci.* 27, 5448–5460. doi: 10.1523/jneurosci.1186-07.2007
- D'Angelo, E., De Filippi, G., Rossi, P., and Taglietti, V. (1995). Synaptic excitation of individual rat cerebellar granule cells *in situ*: evidence for the role of NMDA receptors. *J. Physiol.* 484, 397–413. doi: 10.1113/jphysiol.1995.sp020673
- D'Angelo, E., and De Zeeuw, C. I. (2009). Timing and plasticity in the cerebellum: focus on the granular layer. *Trends Neurosci.* 32, 30–40. doi: 10.1016/j.tins.2008.09.007
- D'Angelo, E., Rossi, P., and Garthwaite, J. (1990). Dual-component NMDA receptor currents at a single central synapse. *Nature* 346, 467–470. doi: 10.1038/346467a0
- D'Angelo, E., Rossi, P., and Taglietti, V. (1993). Different proportions of N-methyl-D-aspartate and non-N-methyl-D-aspartate receptor currents at the mossy fibre-granule cell synapse of developing rat cerebellum. *Neuroscience* 53, 121–130. doi: 10.1016/0306-4522(93)90290-v
- Dean, P., Porrill, J., Ekerot, C. F., and Jörntell, H. (2010). The cerebellar microcircuit as an adaptive filter: experimental and computational evidence. *Nat. Rev. Neurosci.* 11, 30–43. doi: 10.1038/nrn2756
- DiGregorio, D. A., Nusser, Z., and Silver, R. A. (2002). Spillover of glutamate onto synaptic AMPA receptors enhances fast transmission at a cerebellar synapse. *Neuron* 35, 521–533. doi: 10.1016/s0896-6273(02)00787-0
- DiGregorio, D. A., Rothman, J. S., Nielsen, T. A., and Silver, R. A. (2007). Desensitization properties of AMPA receptors at the cerebellar mossy fiber granule cell synapse. *J. Neurosci.* 27, 8344–8357. doi: 10.1523/jneurosci.2399-07.2007
- Eccles, J. C., Ito, M., and Szentagothai, J. (1967). *The Cerebellum as a Neuronal Machine*. New York: Springer Verlag.
- Fujita, M. (1982). Adaptive filter model of the cerebellum. *Biol. Cybern.* 45, 195–206. doi: 10.1007/bf00336192
- Gabbiani, F., Midtgaard, J., and Knöpfel, T. (1994). Synaptic integration in a model of cerebellar granule cells. *J. Neurophysiol.* 72, 999–1009.
- Gulledge, A. T., Kampa, B. M., and Stuart, G. J. (2005). Synaptic integration in dendritic trees. *J. Neurobiol.* 64, 75–90. doi: 10.1002/neu.20144
- Hallermann, S., Fejtova, A., Schmidt, H., Weyhersmüller, A., Silver, R. A., Gundelfinger, E. D., et al. (2010). Bassoon speeds vesicle reloading at a central excitatory synapse. *Neuron* 68, 710–723. doi: 10.1016/j.neuron.2010.10.026
- Hu, H., Martina, M., and Jonas, P. (2010). Dendritic mechanisms underlying rapid synaptic activation of fast-spiking hippocampal interneurons. *Science* 327, 52–58. doi: 10.1126/science.1177876
- Jack, J. J. B., Noble, D., and Tsien, R. W. (1983). *Electric Current Flow in Excitable Cells*. Oxford: Clarendon Press.
- Jakab, R. L., and Hátori, J. (1988). Quantitative morphology and synaptology of cerebellar glomeruli in the rat. *Anat. Embryol. (Berl)* 179, 81–88. doi: 10.1007/bf00305102
- Jörntell, H., and Ekerot, C. F. (2006). Properties of somatosensory synaptic integration in cerebellar granule cells *in vivo*. *J. Neurosci.* 26, 11786–11797. doi: 10.1523/jneurosci.2939-06.2006
- London, M., and Häusser, M. (2005). Dendritic computation. *Annu. Rev. Neurosci.* 28, 503–532. doi: 10.1146/annurev.neuro.28.061604.135703

- Magee, J. C. (2000). Dendritic integration of excitatory synaptic input. *Nat. Rev. Neurosci.* 1, 181–190. doi: 10.1038/35044552
- Magee, J. C., and Cook, E. P. (2000). Somatic EPSP amplitude is independent of synapse location in hippocampal pyramidal neurons. *Nat. Neurosci.* 3, 895–903. doi: 10.1038/78800
- Mainen, Z. F., and Sejnowski, T. J. (1996). Influence of dendritic structure on firing pattern in model neocortical neurons. *Nature* 382, 363–366. doi: 10.1038/382363a0
- Marr, D. (1969). A theory of cerebellar cortex. *J. Physiol.* 202, 437–470. doi: 10.1113/jphysiol.1969.sp008820
- Nevian, T., Larkum, M. E., Polsky, A., and Schiller, J. (2007). Properties of basal dendrites of layer 5 pyramidal neurons: a direct patch-clamp recording study. *Nat. Neurosci.* 10, 206–214. doi: 10.1038/nn1826
- Nörenberg, A., Hu, H., Vida, I., Bartos, M., and Jonas, P. (2010). Distinct nonuniform cable properties optimize rapid and efficient activation of fast-spiking GABAergic interneurons. *Proc. Natl. Acad. Sci. U S A* 107, 894–899. doi: 10.1073/pnas.0910716107
- Olshausen, B. A., and Field, D. J. (2004). Sparse coding of sensory inputs. *Curr. Opin. Neurobiol.* 14, 481–487. doi: 10.1016/j.conb.2004.07.007
- Palay, S. L., and Chan-Palay, V. (1974). *Cerebellar Cortex: Cytology and Organization*. Berlin; Heidelberg: Springer.
- Palkovits, M., Magyar, P., and Szentágothai, J. (1972). Quantitative histological analysis of the cerebellar cortex in the cat. IV. Mossy fiber-Purkinje cell numerical transfer. *Brain Res.* 45, 15–29. doi: 10.1016/0006-8993(72)90213-2
- Prestori, F., Bonardi, C., Mapelli, L., Lombardo, P., Goselink, R., De Stefano, M. E., et al. (2013). Gating of long-term potentiation by nicotinic acetylcholine receptors at the cerebellum input stage. *PLoS One* 8:e64828. doi: 10.1371/journal.pone.0064828
- Rall, W. (1964). “Theoretical significance of dendritic trees for neuronal input-output relations,” in *Neural Theory and Modeling*, ed E. Reiss (Stanford, CA: Stanford University Press), 73–97.
- Rall, W. (1969). Time constants and electrotonic length of membrane cylinders and neurons. *Biophys. J.* 9, 1483–1508. doi: 10.1016/s0006-3495(69)86467-2
- Rancz, E. A., Ishikawa, T., Duguid, I., Chadderton, P., Mahon, S., and Häusser, M. (2007). High-fidelity transmission of sensory information by single cerebellar mossy fibre boutons. *Nature* 450, 1245–1248. doi: 10.1038/nature05995
- Ritzau-Jost, A., Delvendahl, I., Rings, A., Byczkiewicz, N., Harada, H., Shigemoto, R., et al. (2014). Ultrafast action potentials mediate kilohertz signaling at a central synapse. *Neuron* 84, 152–163. doi: 10.1016/j.neuron.2014.08.036
- Sargent, P. B., Saviane, C., Nielsen, T. A., DiGregorio, D. A., and Silver, R. A. (2005). Rapid vesicular release, quantal variability and spillover contribute to the precision and reliability of transmission at a glomerular synapse. *J. Neurosci.* 25, 8173–8187. doi: 10.1523/jneurosci.2051-05.2005
- Saviane, C., and Silver, R. A. (2006). Fast vesicle reloading and a large pool sustain high bandwidth transmission at a central synapse. *Nature* 439, 983–987. doi: 10.1038/nature04509
- Schaefer, A. T., Larkum, M. E., Sakmann, B., and Roth, A. (2003). Coincidence detection in pyramidal neurons is tuned by their dendritic branching pattern. *J. Neurophysiol.* 89, 3143–3154. doi: 10.1152/jn.00046.2003
- Segev, I., and London, M. (2000). Untangling dendrites with quantitative models. *Science* 290, 744–750. doi: 10.1126/science.290.5492.744
- Silver, R. A., Cull-Candy, S. G., and Takahashi, T. (1996). Non-NMDA glutamate receptor occupancy and open probability at a rat cerebellar synapse with single and multiple release sites. *J. Physiol.* 494, 231–250. doi: 10.1113/jphysiol.1996.sp021487
- Silver, R. A., Traynelis, S. F., and Cull-Candy, S. G. (1992). Rapid-time-course miniature and evoked excitatory currents at cerebellar synapses *in situ*. *Nature* 355, 163–166. doi: 10.1038/355163a0
- Spruston, N. (2008). Pyramidal neurons: dendritic structure and synaptic integration. *Nat. Rev. Neurosci.* 9, 206–221. doi: 10.1038/nrn2286
- Stuart, G. J., and Sakmann, B. (1994). Active propagation of somatic action potentials into neocortical pyramidal cell dendrites. *Nature* 367, 69–72. doi: 10.1038/367069a0
- Sultan, F. (2000). Exploring a critical parameter of timing in the mouse cerebellar microcircuitry: the parallel fiber diameter. *Neurosci. Lett.* 280, 41–44. doi: 10.1016/s0304-3940(99)00984-2
- Thome, C., Kelly, T., Yanez, A., Schultz, C., Engelhardt, M., Cambridge, S. B., et al. (2014). Axon-carrying dendrites convey privileged synaptic input in hippocampal neurons. *Neuron* 83, 1418–1430. doi: 10.1016/j.neuron.2014.08.013
- Valera, A. M., Doussau, F., Poulain, B., Barbour, B., and Isopé, P. (2012). Adaptation of granule cell to Purkinje cell synapses to high-frequency transmission. *J. Neurosci.* 32, 3267–3280. doi: 10.1523/JNEUROSCI.3175-11.2012
- Williams, R. W., and Herrup, K. (1988). The control of neuron number. *Annu. Rev. Neurosci.* 11, 423–453. doi: 10.1146/annurev.neuro.11.1.423
- Williams, S. R., and Stuart, G. J. (2000). Site independence of EPSP time course is mediated by dendritic  $I_h$  in neocortical pyramidal neurons. *J. Neurophysiol.* 83, 3177–3182.

**Conflict of Interest Statement:** The authors declare that the research was conducted in the absence of any commercial or financial relationships that could be construed as a potential conflict of interest.

Copyright © 2015 Delvendahl, Straub and Hallermann. This is an open-access article distributed under the terms of the Creative Commons Attribution License (CC BY). The use, distribution and reproduction in other forums is permitted, provided the original author(s) or licensor are credited and that the original publication in this journal is cited, in accordance with accepted academic practice. No use, distribution or reproduction is permitted which does not comply with these terms.

### **3.4 Delvendahl et al. 2016 Neuron 90, 492–498.**

Seite 47–53

# Fast, Temperature-Sensitive and Clathrin-Independent Endocytosis at Central Synapses

Igor Delvendahl,<sup>1,\*</sup> Nicholas P. Vyleta,<sup>2</sup> Henrike von Gersdorff,<sup>2</sup> and Stefan Hallermann<sup>1,\*</sup>

<sup>1</sup>Carl-Ludwig-Institute for Physiology, Medical Faculty, University of Leipzig, Liebigstrasse 27, 04103 Leipzig, Germany

<sup>2</sup>The Vollum Institute, Oregon Health & Science University, Portland, OR 97239, USA

\*Correspondence: igor.delvendahl@medizin.uni-leipzig.de (I.D.), hallermann@medizin.uni-leipzig.de (S.H.)

<http://dx.doi.org/10.1016/j.neuron.2016.03.013>

## SUMMARY

The fusion of neurotransmitter-filled vesicles during synaptic transmission is balanced by endocytotic membrane retrieval. Despite extensive research, the speed and mechanisms of synaptic vesicle endocytosis have remained controversial. Here, we establish low-noise time-resolved membrane capacitance measurements that allow monitoring changes in surface membrane area elicited by single action potentials and stronger stimuli with high-temporal resolution at physiological temperature in individual bona-fide mature central synapses. We show that single action potentials trigger very rapid endocytosis, retrieving presynaptic membrane with a time constant of 470 ms. This fast endocytosis is independent of clathrin but mediated by dynamin and actin. In contrast, stronger stimuli evoke a slower mode of endocytosis that is clathrin, dynamin, and actin dependent. Furthermore, the speed of endocytosis is highly temperature dependent with a  $Q_{10}$  of  $\sim 3.5$ . These results demonstrate that distinct molecular modes of endocytosis with markedly different kinetics operate at central synapses.

## INTRODUCTION

Synaptic communication in the nervous system relies on the release of synaptic vesicles from nerve terminals. Because vesicle fusion increases presynaptic plasma membrane, a balance between endocytosis of fused membrane and vesicle release is required to maintain synaptic function over time (Südhof, 2004). However, the speed and mechanisms of endocytosis remain controversial, mainly due to technical limitations. Separate modes of endocytosis have been distinguished according to their speed or underlying mechanism. The use of electron microscopy to study synaptic vesicle endocytosis (Heuser and Reese, 1973) has recently provided evidence for an ultrafast endocytosis time course (Watanabe et al., 2013) but only allows investigating “snapshots” at a single time point after stimulation in any one cell. Fluorescence imaging of synaptic vesicle endocytosis can observe

endocytosis over time in single synapses (Balaji et al., 2008; Hua et al., 2011; Klingauf et al., 1998; Leitz and Kavalali, 2011; Ryan et al., 1996) but has mostly been restricted to neuronal cultures and features relatively low temporal resolution, which is often limited by the speed of vesicle re-acidification. Measurements of membrane capacitance ( $C_m$ ) on the other hand allow time-resolved investigation of endocytosis in brain slices with high temporal resolution (Lou et al., 2008; Sun et al., 2002; von Gersdorff and Matthews, 1994; Smith et al., 2008) but usually require strong stimuli to achieve sufficient signal-to-noise ratio. Moreover,  $C_m$  measurements at physiological temperature are complicated by the heating bath perfusion, which causes large artifacts in  $C_m$  measurements due to bath level fluctuations. Most previous  $C_m$  measurements were therefore performed at room temperature without continuous bath perfusion. To overcome these limitations, we established low-noise whole-cell presynaptic  $C_m$  measurements at physiological temperature at both mature cerebellar and hippocampal mossy fiber boutons, two functionally very different central excitatory synaptic terminals allowing direct presynaptic patch-clamp recordings (Delvendahl et al., 2013; Ritzau-Jost et al., 2014; Vyleta and Jonas, 2014). With these technical advancements, we were able to investigate the mechanisms and kinetics of endocytosis following single action potentials (APs), short trains of APs, or stronger voltage-clamp depolarizations at physiological temperature in mature central synapses.

## RESULTS

### Ultrafast Single-AP-Evoked Endocytosis

We first used presynaptic patch-clamp recordings and  $C_m$  measurements in cerebellar mossy fiber boutons (cMFBs) to investigate the endocytosis time course. With optimized recording conditions using quartz-glass pipettes (Dudel et al., 2000; Hallermann et al., 2005), we resolved  $C_m$  changes associated with single APs at mammalian physiological temperature (36°C). A recorded AP waveform voltage command with half-duration of 129  $\mu$ s elicited a  $Ca^{2+}$  current with half-duration of  $112 \pm 4 \mu$ s ( $n = 34$  cMFBs), consistent with previous results (Ritzau-Jost et al., 2014), and a transient  $C_m$  increase that decayed rapidly within the first second (Figure 1A). However, some  $C_m$  transients may be unrelated to exo- and endocytosis (Wu et al., 2005; Yamashita et al., 2005). We therefore specifically blocked exocytosis with tetanustoxin light chain (TeNT-LC), which inhibits



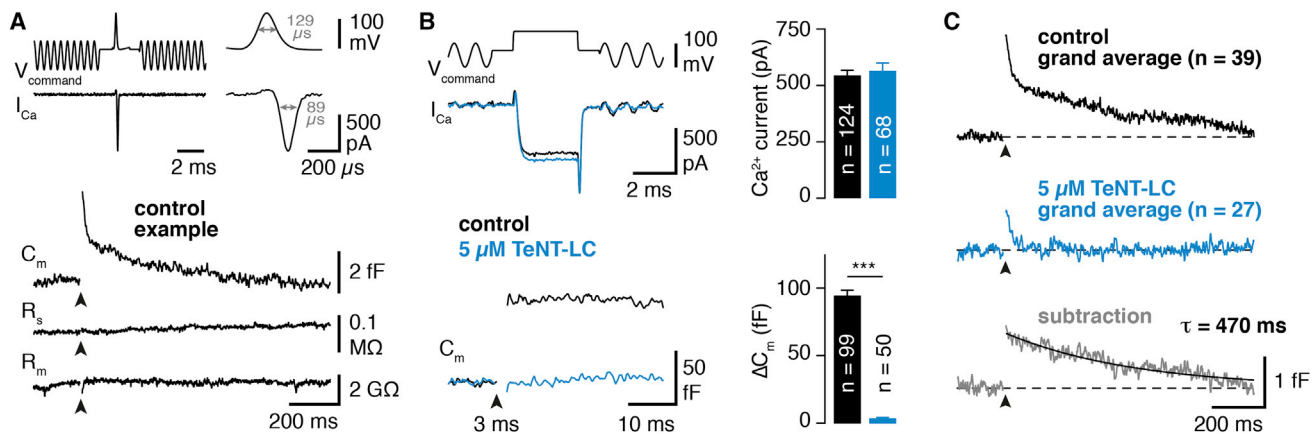


**Figure 1. Ultrafast Single-AP-Evoked Endocytosis**

(A) Top: voltage command ( $V_{\text{command}}$ ) used for AP-evoked capacitance recordings in cMFBs. The AP waveform was recorded in a previous experiment with axonal stimulation. An example of a resulting  $\text{Ca}^{2+}$  current ( $I_{\text{Ca}}$ ) is depicted below. On the right,  $V_{\text{command}}$  and  $I_{\text{Ca}}$  are shown on an expanded timescale and half-durations are indicated. Middle: example single-AP-evoked  $C_m$  trace (average of 40 consecutive sweeps). Bottom: corresponding series and membrane resistance ( $R_s$  and  $R_m$ , respectively).

(B) TeNT-LC effectively blocks synaptic vesicle exocytosis in cMFBs. Top: voltage protocol with 3-ms depolarization from  $-80$  mV to  $0$  mV. Middle: pharmacologically isolated  $\text{Ca}^{2+}$  current immediately after break-in (control, black) and after 3:00 min of whole-cell recording ( $5 \mu\text{M}$  TeNT-LC, blue). Bottom: corresponding  $C_m$  traces. Right: average data of  $\text{Ca}^{2+}$  current amplitudes and  $C_m$  increase ( $\Delta C_m$ ) elicited with 3-ms depolarizations for control (black) and  $5 \mu\text{M}$  TeNT-LC (blue;  $n$  represents number of cMFBs). Data are represented as mean  $\pm$  SEM.

(C) Grand average of AP-evoked  $C_m$  responses (black,  $n$  represents number of cMFBs). Blocking synaptic vesicle exocytosis with  $5 \mu\text{M}$  TeNT-LC (blue) revealed a transient  $C_m$  increase not related to exocytosis. Subtraction (gray) shows the time course of endocytosis following a single AP. See also Figure S1.

synaptic vesicle fusion by cleaving synaptobrevin (Figures 1B and S1E–S1G). For single APs, a small and rapidly decaying  $C_m$  component remained with TeNT-LC (Figure 1C). This  $C_m$  component did not change over time and after repeated stimulation (Figure S1G), indicating that the transient  $C_m$  increase is not caused by exocytosis of vesicles with pre-assembled SNARE-complexes (Hayashi et al., 1994) but reflects non-exocytosis  $C_m$  changes (Yamashita et al., 2005). Subtraction of the  $C_m$  trace with TeNT-LC from control revealed that a single AP leads to a  $C_m$  increase of  $1.3 \pm 0.2$  fF ( $n = 39$  cMFBs), corresponding to exocytosis of  $18 \pm 2$  synaptic vesicles (assuming a single vesicle capacitance of  $70$  aF; Hallermann et al., 2003). Exocytosis was followed by a rapid  $C_m$  decay with time constant of  $470 \pm 70$  ms ( $n = 39$ ; Figure 1C). Thus, endocytosis evoked by single APs is ultrafast at cMFBs, consistent with recent results at cultured hippocampal synapses using flash-and-freeze electron microscopy methods (Watanabe et al., 2013).

### Highly Temperature-Sensitive Endocytosis at Hippocampal and Cerebellar Mossy Fiber Synapses

AP firing in cMFBs can reach very high frequencies (Ritzau-Jost et al., 2014), and very fast endocytosis may constitute an adaptation to this firing behavior. To address whether the observed fast endocytosis is specific to cMFBs or a general property of central synapses, we analyzed  $C_m$  changes in hippocampal mossy fiber boutons (hMFBs), which operate at lower frequencies and have very different functional properties, such as a broader AP-half-duration, facilitation of excitatory postsynaptic currents, and prominent long-term potentiation (Delvendahl et al., 2013). At hMFBs, a train of ten 1-ms depolarizations delivered at  $50$  Hz resulted in an increase in  $C_m$ , which was

followed by a very rapid  $C_m$  decay with a fast time constant of  $1.2 \pm 0.4$  s ( $n = 8$  hMFBs, Figure 2A). We next analyzed the temperature dependence of endocytosis in hMFBs and cMFBs, because (1) previous studies suggested that ultrafast endocytosis requires physiological temperatures (Watanabe et al., 2013), and because (2) the comparison of the temperature dependence of endocytosis at hMFBs and cMFBs allows testing whether these two central synapses use similar endocytotic mechanisms. The speed of  $C_m$  decay following  $50$  Hz trains was highly temperature dependent at hMFBs, being much faster at  $36^\circ\text{C}$  than at  $30^\circ\text{C}$  or at room temperature (Figures 2A–2C). As in the calyx of Held, the time course of endocytosis follows a double exponential at high temperatures (Renden and von Gersdorff, 2007). The resulting  $Q_{10}$  temperature coefficient of the amplitude-weighted time constant of the  $C_m$  decay in hMFBs was  $3.3 \pm 1.9$  (bootstrap SEM, corresponding to a 16%–84% confidence interval; Figure 2D), which is higher than previously reported (Balaji et al., 2008; Fernández-Alfonso and Ryan, 2004; Granseth and Lagnado, 2008). We also analyzed the temperature dependence of endocytosis at cMFBs. Comparison of the  $C_m$  decay in response to 3-ms depolarizations at  $23^\circ\text{C}$  and  $36^\circ\text{C}$  in cMFBs (Figure S2A) revealed a  $Q_{10}$  temperature coefficient of  $3.8 \pm 1.3$  (bootstrap SEM; Figure 2D). The strong overlap of the 16%–84% confidence intervals indicates that the  $Q_{10}$  of endocytosis is similar in hMFBs and cMFBs. We also find that exocytosis and  $\text{Ca}^{2+}$  currents are highly temperature dependent (Figure S2). These results show that endocytosis is very fast at cMFBs and hMFBs with very similar temperature sensitivity, suggesting that similar mechanisms operate at these central synapses. We therefore focus on cMFBs from now on to gain insights into the molecular machinery mediating fast endocytosis.

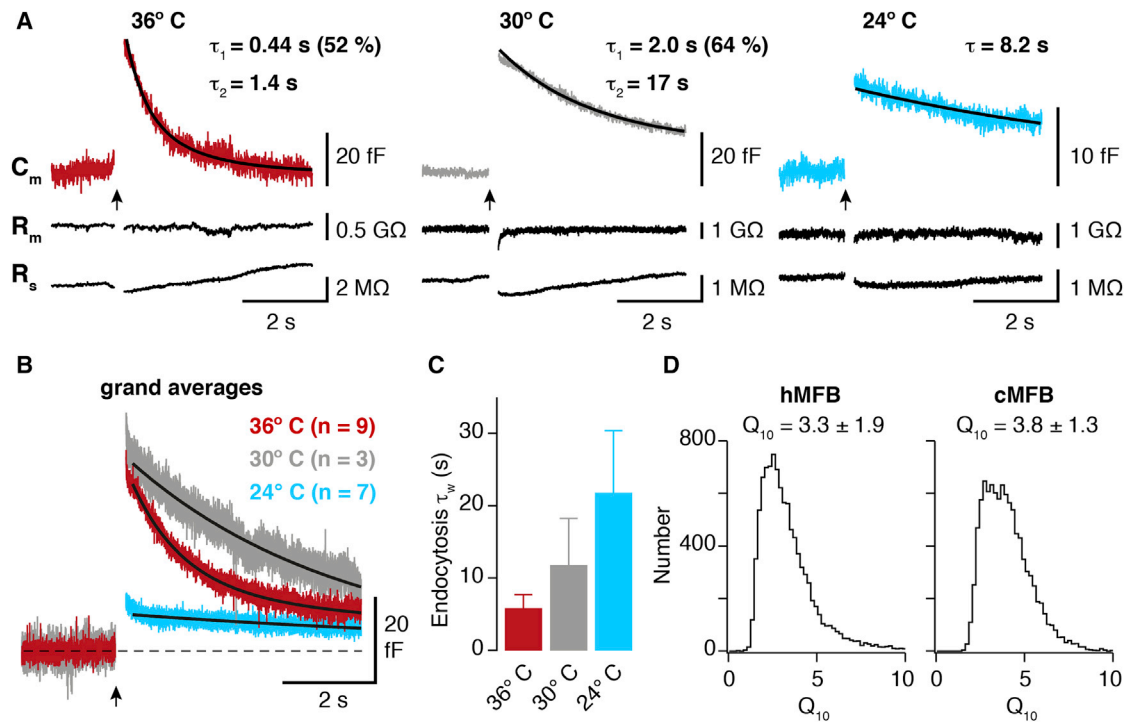


**Figure 2. Highly Temperature-Sensitive Endocytosis at Hippocampal and Cerebellar Mossy Fiber Synapses**

(A) Example traces of  $C_m$  recordings in hMFBs evoked by a train of ten stimuli (1-ms depolarizations to +20 mV) delivered at 50 Hz (arrow) at 36°C (red), 30°C (gray), and 24°C (blue). Lower traces represent corresponding membrane and series resistance ( $R_m$  and  $R_s$ , respectively).

(B) Grand average  $C_m$  traces recorded at 36°C, 30°C, and 24°C (color code as in A; n represents number of hMFBs). The decay of the grand average traces was best fit with the sum of two exponentials with time constants of 1.1 s (67%) and 11.3 s for 36°C, the sum of two exponentials with time constants of 2.3 s (43%) and 7.4 s for 30°C, and a single exponential function with time constant of 10.7 s for 24°C.

(C) Average amplitude-weighted time constant ( $\tau_w$ ) of the exponential fits to the  $C_m$  decay for the three temperatures. Data are represented as mean  $\pm$  SEM, n is given in (B).

(D) Left: histogram of  $Q_{10}$  values by bootstrap analysis of endocytosis time constants obtained in hMFBs based on  $\tau_w$  data shown in (C). Right: corresponding histogram of  $Q_{10}$  values by bootstrap analysis of endocytosis time constants obtained in cMFBs using 3-ms depolarizations at 23°C and 36°C (cf. Figure S2A). See also Figure S2.

### Clathrin-Independent Single-AP-Evoked Endocytosis

We applied inhibitors of proteins involved in important molecular pathways mediating endocytosis and studied endocytosis following single APs in cMFBs. AP-evoked fast endocytosis was not affected by the clathrin inhibitor pitstop 2 (control: endocytosis  $\tau = 470 \pm 70$  ms,  $n = 39$ ; pitstop 2:  $\tau = 490 \pm 80$  ms,  $n = 32$ ;  $p = 0.92$ ; Figures 3A and 3B), indicating that fast endocytosis is clathrin-independent. In contrast, the dynamin-inhibitor dynasore and the actin polymerization inhibitor latrunculin A blocked endocytosis evoked by single APs almost completely (both  $p < 0.0001$ ; Figures 3A and 3B). The endocytosis inhibitors had no effect on amplitude or kinetics of presynaptic  $Ca^{2+}$  currents (Figure S3). These data suggest that fast AP-evoked endocytosis in cMFBs is clathrin-independent but mediated by dynamin and actin, consistent with findings at calf chromaffin cells and cultured mouse hippocampal synapses (Artalejo et al., 1995; Watanabe et al., 2013, 2014).

### Distinct Molecular Modes of Endocytosis

Our approach allows comparing the speed and molecular mechanism of endocytosis evoked by single APs and by stronger

stimuli in a single bouton. Trains of 20 APs at a frequency of 300 Hz elicited presynaptic  $Ca^{2+}$  currents with amplitude facilitation at cMFBs (Figure 4A; Ritzau-Jost et al., 2014). Such AP trains evoked a  $C_m$  increase that was blocked by TeNT-LC (Figure 4B). The  $C_m$  decay following AP train stimulation was not affected by the presence of pitstop 2 but strongly prolonged by application of dynasore or latrunculin A (Figure 4B). The resulting time constants of endocytosis were  $920 \pm 190$  ms for control ( $n = 18$ ),  $1,000 \pm 160$  ms for pitstop 2 ( $n = 29$ ;  $p = 0.92$ ), and  $\sim 6$  s for dynasore and latrunculin A ( $n = 24$  and 23), with comparable amplitude of the  $C_m$  increase under all conditions (Figures 4E and 4F). Thus, trains of APs at high-frequency result in endocytosis that is slower than that for single APs (cf. Figure 1), consistent with previous findings (Sun et al., 2002), but both stimuli trigger endocytosis operating with similar molecular mechanisms.

We next examined whether even stronger stimuli such as prolonged depolarizations (Figures 4C and 4D) entail endocytosis with time course similar to that for single APs or trains of APs. The amount of exocytosis was not reduced by endocytosis inhibitors for short durations of depolarizations, but significantly

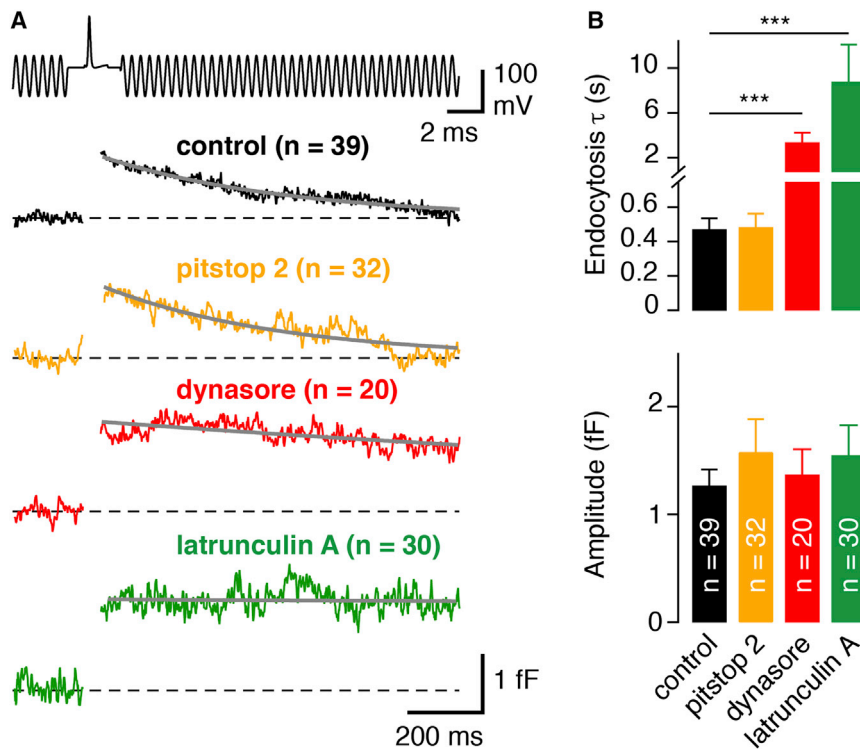


**Figure 3. Clathrin-Independent Single-AP-Evoked Endocytosis**

(A) Top: voltage command used for AP-evoked  $C_m$  recordings in cMFBs. Bottom: grand averages of AP-evoked  $C_m$  responses (n represents number of cMFBs) for control (black), application of a clathrin-inhibitor (pitstop 2, 25  $\mu$ M; orange), a dynamin-inhibitor (dynasore, 100  $\mu$ M; red), and an actin-inhibitor (latrunculin A, 25  $\mu$ M; green). Gray solid lines are exponential fits to the  $C_m$  decay.

(B) Average time constants of endocytosis and amplitudes of AP-evoked  $\Delta C_m$  with endocytosis inhibitors (color code as in A). The speed of endocytosis was unaltered by pitstop 2 ( $p = 0.92$ ) but significantly slowed by dynasore and latrunculin A ( $p < 0.001$ ). Data are represented as mean  $\pm$  SEM. See also Figure S3.

reduced by latrunculin A for 30 ms pulses (Figure 4E), consistent with previous findings (Hosoi et al., 2009; Lee et al., 2012; Rizzoli and Betz, 2005; Sankaranarayanan et al., 2003). TeNT-LC blocked synaptic vesicle exocytosis for all types of stimuli as expected (Figures 4E and S1E–S1G; Sakaba et al., 2005). To directly compare the kinetics of endocytosis, we focused on the initial  $C_m$  decay within 2 s after the stimulus. The biexponential  $C_m$  decay of 1–30 ms depolarizations is analyzed in Figure S4. Pitstop 2, dynasore, and latrunculin A markedly slowed endocytosis following depolarizing pulses, demonstrating that slow endocytosis is clathrin, dynamin, and actin dependent (Figure 4D). These findings demonstrate that two distinct modes of endocytosis occur at presynaptic terminals that are likely to be triggered depending on the type of stimulus. Indeed, endocytosis was still faster for AP train stimuli (50 APs) than for short depolarizations when both stimuli produced similar  $\Delta C_m$  (Figures S4C and S4D). These data indicate that actin and dynamin are required for all modes of endocytosis, whereas clathrin is not required for a rapid mode of endocytosis elicited by single APs or short AP trains (Figure 4F).

## DISCUSSION

Using presynaptic  $C_m$  measurements, we here demonstrate that endocytosis following single APs at physiological temperature is very fast and clathrin-independent. Endocytosis evoked by strong stimuli, however, is slower and requires clathrin. Our study extends previous findings by (1) determining the speed and mechanisms of endocytosis for single APs in mature synapses in brain slices, thoroughly addressing potential  $C_m$  artifacts, by (2) quantifying the temperature coefficient of endocytosis in

with recent flash-and-freeze findings, where endocytotic structures were observed from 50 ms until  $\sim 1$  s after the stimulus (Watanabe et al., 2013, 2014). The 470-ms time constant of AP-evoked endocytosis is consistent with these recent electron microscopic findings, because initial endocytotic structures (i.e., shallow and deep pits) are not detected with  $C_m$  measurements. Previous studies of fast endocytosis using  $C_m$  measurements have been confounded by  $C_m$  artifacts (Wu et al., 2005; Yamashita et al., 2005). Here, we were able to distinguish exo- and endocytosis from transient  $C_m$  artifacts (Figure 1; Yamashita et al., 2005). The slowing of endocytosis kinetics with increasing AP number (cf. Figures 1, 4, and S4) is consistent with previous findings (Sun et al., 2002). The observed fast endocytosis following single APs is also comparable to the speed of endocytosis in cone photoreceptor cells (Van Hook and Thoreson, 2012).

In contrast to the fast endocytosis observed here with presynaptic  $C_m$  measurements (see also Sun et al., 2002; Van Hook and Thoreson, 2012; Watanabe et al., 2013), fluorescence imaging techniques usually reveal slower endocytosis rates (e.g., Balaji et al., 2008; Kononenko et al., 2013; but see Leitz and Kavalali, 2014). One possible explanation is provided by the strong impact of both temperature (Figure 2) and stimulation strength (Figure 4F) on endocytosis kinetics. We determined a very high temperature coefficient of endocytosis that might be caused by the strong temperature dependence of dynamin GTPase activity ( $Q_{10}$  of 5.7; Leonard et al., 2005). Taking the high temperature dependence into account, our results using square depolarizing pulses are compatible with endocytosis time constants of 10–40 s obtained with fluorescence imaging at room temperature (Balaji et al., 2008; Granseth et al., 2006; Hua et al., 2011;

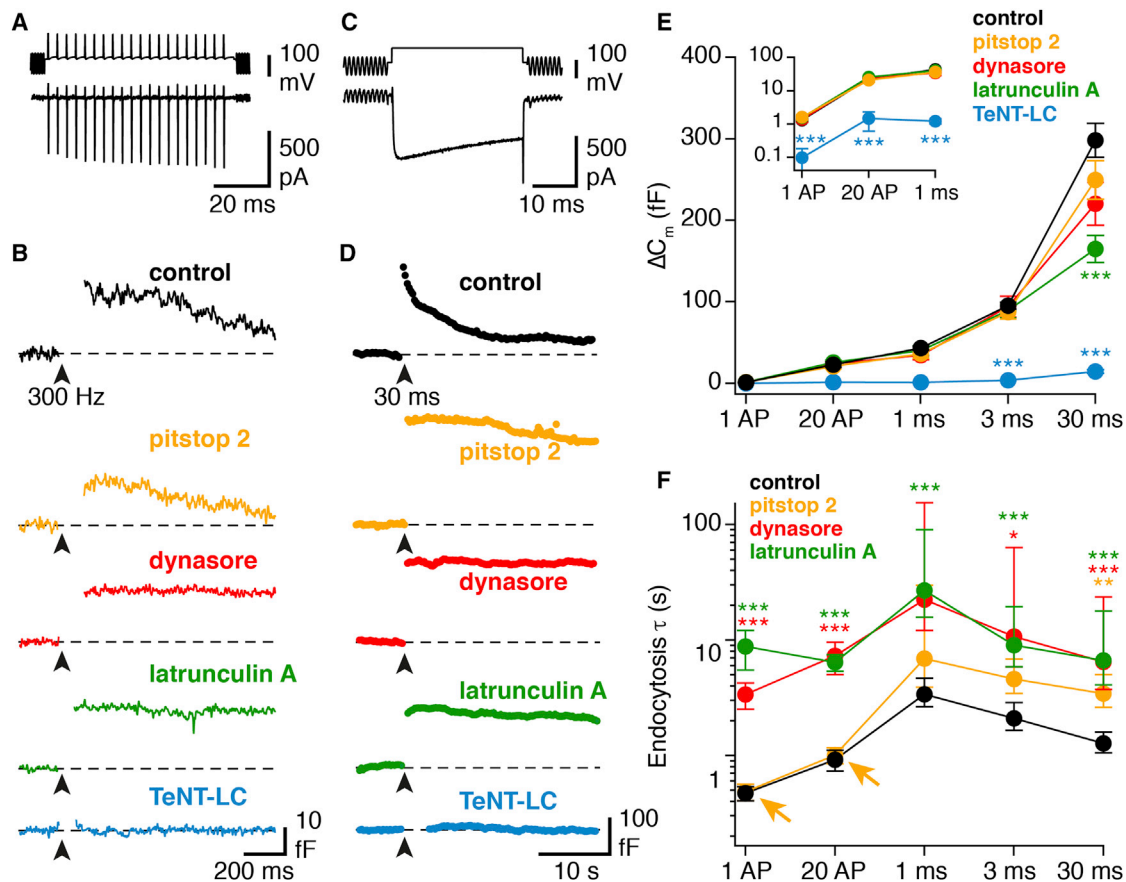


#### Figure 4. Distinct Molecular Modes of Endocytosis

(A) Top: voltage command of 20 APs at a frequency of 300 Hz for  $C_m$  recordings in cMFBs. Bottom: corresponding  $Ca^{2+}$  currents with slight amplitude facilitation.

(B) Example  $C_m$  traces following 20 APs at 300 Hz for control (black), application of a clathrin-inhibitor (pitstop 2, 25  $\mu$ M; orange), a dynamin-inhibitor (dynasore, 100  $\mu$ M; red), an actin-inhibitor (latrunculin A, 25  $\mu$ M; green), and with TeNT-LC (5  $\mu$ M, blue).

(C) Top: 30-ms voltage step from  $-80$  mV to 0 mV. Bottom: corresponding  $Ca^{2+}$  current.

(D) Example  $C_m$  traces following a 30-ms depolarization as shown in (C).

(E) Summary of the effect of endocytosis inhibitors on exocytosis evoked by different stimuli recorded in cMFBs (color code as in B and D). The endocytosis inhibitors dynasore, latrunculin A, and pitstop 2 had no effect on exocytosis evoked by weaker stimuli (1 AP, 20 APs, 1 ms, and 3 ms), whereas TeNT-LC completely blocked synaptic vesicle exocytosis. For 30-ms step pulses, exocytosis was reduced by latrunculin A. Inset: enlargement of the first three stimulus types on a logarithmic scale.

(F) Summary of the effect of endocytosis inhibitors on time constants of endocytosis evoked by different stimuli. The clathrin inhibitor (pitstop 2, orange) had no effect on fast endocytosis evoked by single APs and AP trains (arrows) but stronger impact on endocytosis evoked by depolarizations of 1, 3, or 30 ms duration. In contrast, a dynamin-inhibitor (dynasore, red) and an actin-inhibitor (latrunculin A, green) reduced the speed of endocytosis evoked by all tested stimuli. Throughout the figure, data are represented as mean  $\pm$  SEM and asterisks indicate significance level with Kruskal-Wallis tests and post hoc Mann-Whitney U tests both with Bonferroni-Holm correction. Asymmetric error bars for 1–30 ms depolarizations represent the inverse of the SEM boundaries of the rate constants (see Supplemental Experimental Procedures). See also Figures S3 and S4.

Kononenko et al., 2013; Ryan et al., 1996). Furthermore,  $C_m$  measurements report endocytosis of presynaptic membrane in contrast to some fluorescence imaging techniques based on tagged vesicular proteins that measure protein endocytosis. It is thus possible that the endocytosis of some synaptic vesicle proteins has a slower speed and relies on different mechanisms than membrane retrieval (Kononenko and Haucke, 2015). However, we also note that whole-cell recordings may disrupt normal intracellular function via the dialysis of mobile proteins and changes in membrane tension (Heidelberger et al., 2002; Hull and von Gersdorff, 2004).

We found that two modes of endocytosis with distinct underlying mechanisms can be evoked in central synapses in acute brain slices, similar to findings in cultured hippocampal neurons (Kononenko et al., 2014). Our data indicate that fast endocytosis following single APs or short AP trains is independent of clathrin, consistent with previous work (Artalejo et al., 1995; Kononenko et al., 2014; Van Hook and Thoreson, 2012; Watanabe et al., 2014). Moreover, actin and dynamin inhibitors suggest that the molecular mechanism of fast endocytosis involves actin as well as dynamin (Artalejo et al., 1995; Watanabe et al., 2013). The slower endocytosis evoked by voltage steps, on the other



hand, requires clathrin in addition to actin and dynamin. Why is endocytosis slower for AP trains or brief depolarizations than for single APs? The membrane area that can be retrieved in an ultrafast manner may be limited according to the concept of a “readily retrievable pool” of vesicles (Hua et al., 2011) and stronger stimuli might exhaust this fast endocytosis capacity (Thomas et al., 1994). However, the gradual slowing of a monophasic decay observed here and in previous studies using  $C_m$  measurements (Renden and von Gersdorff, 2007; Sun et al., 2002; Yamashita et al., 2005) is inconsistent with a fast exhaustible mechanism, which would predict varying contributions of two components with constant kinetics. Additional mechanisms must therefore operate at central synapses (Alabi and Tsien, 2013; Cousin, 2015). Indeed,  $Ca^{2+}$  was shown to trigger both exo- and endocytosis (Wu et al., 2009; Yamashita et al., 2010), and the amount of  $Ca^{2+}$  influx seems to influence the time course of endocytosis (Balaji et al., 2008; Leitz and Kavalali, 2011; Sanakaranarayanan and Ryan, 2001; von Gersdorff and Matthews, 1994). Furthermore, trains of 50 APs mimicking the  $\Delta C_m$  of 1-ms pulse depolarizations resulted in faster endocytosis than 1-ms pulse depolarizations (Figures S4C and S4D). This finding indicates that the spatiotemporal  $Ca^{2+}$  signal also regulates the speed of endocytosis independent of the amount of exocytosis (Hosoi et al., 2009; Kononenko et al., 2014; Midorikawa et al., 2014; Yamashita et al., 2010).

Our mechanistic conclusions are based on pharmacological inhibitors and are thus limited by potential off-target effects (Park et al., 2013; Willox et al., 2014). We also note that we tested only a single pharmacological inhibitor per endocytosis protein. However, the mechanistically important finding that fast endocytosis is clathrin-independent is unlikely to be confounded by off-target effects because pitstop 2 had no effect on rapid endocytosis. If anything, off-target effects would erroneously increase the impact of pitstop 2. In addition, pitstop 2 did not impact presynaptic  $Ca^{2+}$  currents (Figure S3). The similar effects of latrunculin A and dynasore argue for a dynamin and actin dependence, although we cannot exclude that other forms of endocytosis are also inhibited by these drugs (Park et al., 2013).

In summary, our data demonstrate that the speed of endocytotic membrane retrieval following physiological stimuli is very fast in central synapses. The direct comparison of single APs and stronger stimuli revealed two molecularly distinct modes of endocytosis with markedly different speed. In combination with our findings of a strong temperature dependence of endocytosis kinetics, our results explain why previous studies performed at room temperature, with stronger stimuli, or with lower temporal resolution were unable to detect fast endocytosis. Thus, our data indicate that fast, clathrin-independent endocytosis is an essential feature underlying the function of mature central synapses.

## EXPERIMENTAL PROCEDURES

Methods are described in detail in the Supplemental Experimental Procedures. Presynaptic  $C_m$  measurements were performed essentially as described previously at cMFBS of 35- to 55-day-old C57BL/6 mice (Ritzau-Jost et al., 2014) and at hMFBS of 22- to 30-day-old rats (Hallermann et al.,

2003). All experiments were performed at 35°C–37°C unless otherwise stated. For low-noise  $C_m$  measurements, quartz glass pipettes were used (Dudel et al., 2000).

## SUPPLEMENTAL INFORMATION

Supplemental Information includes Supplemental Experimental Procedures and four figures and can be found with this article online at <http://dx.doi.org/10.1016/j.neuron.2016.03.013>.

## AUTHOR CONTRIBUTIONS

I.D. and N.P.V. performed experiments; I.D., N.P.V., H.v.G., and S.H. conceived experiments and wrote the manuscript.

## ACKNOWLEDGMENTS

We thank T. Sakaba and E. Neher for kindly providing tetanus toxin light chain. This work was supported by the Heisenberg Program of the German Research Foundation (Grant HA 6386/2-2 and 3-2) to S.H., and a Leibniz-Visiting Scientist program and NIDCD grant (DC012938) to H.v.G.

Received: December 24, 2015

Revised: February 29, 2016

Accepted: March 15, 2016

Published: April 14, 2016

## REFERENCES

- Alabi, A.A., and Tsien, R.W. (2013). Perspectives on kiss-and-run: role in exocytosis, endocytosis, and neurotransmission. *Annu. Rev. Physiol.* **75**, 393–422.
- Artalejo, C.R., Henley, J.R., McNiven, M.A., and Palfrey, H.C. (1995). Rapid endocytosis coupled to exocytosis in adrenal chromaffin cells involves  $Ca^{2+}$ , GTP, and dynamin but not clathrin. *Proc. Natl. Acad. Sci. USA* **92**, 8328–8332.
- Balaji, J., Armbruster, M., and Ryan, T.A. (2008). Calcium control of endocytic capacity at a CNS synapse. *J. Neurosci.* **28**, 6742–6749.
- Cousin, M.A. (2015). Synaptic Vesicle Endocytosis and Endosomal Recycling in Central Nerve Terminals: Discrete Trafficking Routes? *Neuroscientist* **21**, 413–423.
- Delvendahl, I., Weyhersmüller, A., Ritzau-Jost, A., and Hallermann, S. (2013). Hippocampal and cerebellar mossy fibre boutons - same name, different function. *J. Physiol.* **591**, 3179–3188.
- Dudel, J., Hallermann, S., and Heckmann, M. (2000). Quartz glass pipette puller operating with a regulated oxy-hydrogen burner. *Pflügers Arch.* **441**, 175–180.
- Fernández-Alfonso, T., and Ryan, T.A. (2004). The kinetics of synaptic vesicle pool depletion at CNS synaptic terminals. *Neuron* **41**, 943–953.
- Granseth, B., and Lagnado, L. (2008). The role of endocytosis in regulating the strength of hippocampal synapses. *J. Physiol.* **586**, 5969–5982.
- Granseth, B., Odermatt, B., Royle, S.J., and Lagnado, L. (2006). Clathrin-mediated endocytosis is the dominant mechanism of vesicle retrieval at hippocampal synapses. *Neuron* **51**, 773–786.
- Hallermann, S., Pawlu, C., Jonas, P., and Heckmann, M. (2003). A large pool of releasable vesicles in a cortical glutamatergic synapse. *Proc. Natl. Acad. Sci. USA* **100**, 8975–8980.
- Hallermann, S., Heckmann, S., Dudel, J., and Heckmann, M. (2005). Short openings in high resolution single channel recordings of mouse nicotinic receptors. *J. Physiol.* **563**, 645–662.
- Hayashi, T., McMahon, H., Yamasaki, S., Binz, T., Hata, Y., Südhof, T.C., and Niemann, H. (1994). Synaptic vesicle membrane fusion complex: action of clostridial neurotoxins on assembly. *EMBO J.* **13**, 5051–5061.
- Heidelberger, R., Zhou, Z.Y., and Matthews, G. (2002). Multiple components of membrane retrieval in synaptic terminals revealed by changes in hydrostatic pressure. *J. Neurophysiol.* **88**, 2509–2517.



- Heuser, J.E., and Reese, T.S. (1973). Evidence for recycling of synaptic vesicle membrane during transmitter release at the frog neuromuscular junction. *J. Cell Biol.* *57*, 315–344.
- Hosoi, N., Holt, M., and Sakaba, T. (2009). Calcium dependence of exo- and endocytotic coupling at a glutamatergic synapse. *Neuron* *63*, 216–229.
- Hua, Y., Sinha, R., Thiel, C.S., Schmidt, R., Hüve, J., Martens, H., Hell, S.W., Egner, A., and Klingauf, J. (2011). A readily retrievable pool of synaptic vesicles. *Nat. Neurosci.* *14*, 833–839.
- Hull, C., and von Gersdorff, H. (2004). Fast endocytosis is inhibited by GABA-mediated chloride influx at a presynaptic terminal. *Neuron* *44*, 469–482.
- Klingauf, J., Kavalali, E.T., and Tsien, R.W. (1998). Kinetics and regulation of fast endocytosis at hippocampal synapses. *Nature* *394*, 581–585.
- Kononenko, N.L., and Haucke, V. (2015). Molecular mechanisms of presynaptic membrane retrieval and synaptic vesicle reformation. *Neuron* *85*, 484–496.
- Kononenko, N.L., Diril, M.K., Puchkov, D., Kintscher, M., Koo, S.J., Pfuhl, G., Winter, Y., Wienisch, M., Klingauf, J., Breustedt, J., et al. (2013). Compromised fidelity of endocytic synaptic vesicle protein sorting in the absence of stonin 2. *Proc. Natl. Acad. Sci. USA* *110*, E526–E535.
- Kononenko, N.L., Puchkov, D., Classen, G.A., Walter, A.M., Pechstein, A., Sawade, L., Kaempf, N., Trimbuch, T., Lorenz, D., Rosenmund, C., et al. (2014). Clathrin/AP-2 mediate synaptic vesicle reformation from endosome-like vacuoles but are not essential for membrane retrieval at central synapses. *Neuron* *82*, 981–988.
- Lee, J.S., Ho, W.K., and Lee, S.H. (2012). Actin-dependent rapid recruitment of reluctant synaptic vesicles into a fast-releasing vesicle pool. *Proc. Natl. Acad. Sci. USA* *109*, E765–E774.
- Leitz, J., and Kavalali, E.T. (2011).  $Ca^{2+}$  influx slows single synaptic vesicle endocytosis. *J. Neurosci.* *31*, 16318–16326.
- Leitz, J., and Kavalali, E.T. (2014). Fast retrieval and autonomous regulation of single spontaneously recycling synaptic vesicles. *eLife* *3*, e03658.
- Leonard, M., Song, B.D., Ramachandran, R., and Schmid, S.L. (2005). Robust colorimetric assays for dynamin's basal and stimulated GTPase activities. *Methods Enzymol.* *404*, 490–503.
- Lou, X., Paradise, S., Ferguson, S.M., and De Camilli, P. (2008). Selective saturation of slow endocytosis at a giant glutamatergic central synapse lacking dynamin 1. *Proc. Natl. Acad. Sci. USA* *105*, 17555–17560.
- Midorikawa, M., Okamoto, Y., and Sakaba, T. (2014). Developmental changes in  $Ca^{2+}$  channel subtypes regulating endocytosis at the calyx of Held. *J. Physiol.* *592*, 3495–3510.
- Park, R.J., Shen, H., Liu, L., Liu, X., Ferguson, S.M., and De Camilli, P. (2013). Dynamin triple knockout cells reveal off target effects of commonly used dynamin inhibitors. *J. Cell Sci.* *126*, 5305–5312.
- Renden, R., and von Gersdorff, H. (2007). Synaptic vesicle endocytosis at a CNS nerve terminal: faster kinetics at physiological temperatures and increased endocytotic capacity during maturation. *J. Neurophysiol.* *98*, 3349–3359.
- Ritzau-Jost, A., Delvendahl, I., Rings, A., Byczkowicz, N., Harada, H., Shigemoto, R., Hirrlinger, J., Eilers, J., and Hallermann, S. (2014). Ultrafast action potentials mediate kilohertz signaling at a central synapse. *Neuron* *84*, 152–163.
- Rizzoli, S.O., and Betz, W.J. (2005). Synaptic vesicle pools. *Nat. Rev. Neurosci.* *6*, 57–69.
- Ryan, T.A., Smith, S.J., and Reuter, H. (1996). The timing of synaptic vesicle endocytosis. *Proc. Natl. Acad. Sci. USA* *93*, 5567–5571.
- Sakaba, T., Stein, A., Jahn, R., and Neher, E. (2005). Distinct kinetic changes in neurotransmitter release after SNARE protein cleavage. *Science* *309*, 491–494.
- Sankaranarayanan, S., and Ryan, T.A. (2001). Calcium accelerates endocytosis of vSNAREs at hippocampal synapses. *Nat. Neurosci.* *4*, 129–136.
- Sankaranarayanan, S., Atluri, P.P., and Ryan, T.A. (2003). Actin has a molecular scaffolding, not propulsive, role in presynaptic function. *Nat. Neurosci.* *6*, 127–135.
- Smith, S.M., Renden, R., and von Gersdorff, H. (2008). Synaptic vesicle endocytosis: fast and slow modes of membrane retrieval. *Trends Neurosci.* *31*, 559–568.
- Südhof, T.C. (2004). The synaptic vesicle cycle. *Annu. Rev. Neurosci.* *27*, 509–547.
- Sun, J.Y., Wu, X.S., and Wu, L.G. (2002). Single and multiple vesicle fusion induce different rates of endocytosis at a central synapse. *Nature* *417*, 555–559.
- Thomas, P., Lee, A.K., Wong, J.G., and Almers, W. (1994). A triggered mechanism retrieves membrane in seconds after  $Ca^{2+}$ -stimulated exocytosis in single pituitary cells. *J. Cell Biol.* *124*, 667–675.
- Van Hook, M.J., and Thoreson, W.B. (2012). Rapid synaptic vesicle endocytosis in cone photoreceptors of salamander retina. *J. Neurosci.* *32*, 18112–18123.
- von Gersdorff, H., and Matthews, G. (1994). Inhibition of endocytosis by elevated internal calcium in a synaptic terminal. *Nature* *370*, 652–655.
- Vyleta, N.P., and Jonas, P. (2014). Loose coupling between  $Ca^{2+}$  channels and release sensors at a plastic hippocampal synapse. *Science* *343*, 665–670.
- Watanabe, S., Rost, B.R., Camacho-Pérez, M., Davis, M.W., Söhl-Kielczynski, B., Rosenmund, C., and Jorgensen, E.M. (2013). Ultrafast endocytosis at mouse hippocampal synapses. *Nature* *504*, 242–247.
- Watanabe, S., Trimbuch, T., Camacho-Pérez, M., Rost, B.R., Brokowski, B., Söhl-Kielczynski, B., Felies, A., Davis, M.W., Rosenmund, C., and Jorgensen, E.M. (2014). Clathrin regenerates synaptic vesicles from endosomes. *Nature* *515*, 228–233.
- Willox, A.K., Sahraoui, Y.M., and Royle, S.J. (2014). Non-specificity of Pitstop 2 in clathrin-mediated endocytosis. *Biol. Open* *3*, 326–331.
- Wu, W., Xu, J., Wu, X.S., and Wu, L.G. (2005). Activity-dependent acceleration of endocytosis at a central synapse. *J. Neurosci.* *25*, 11676–11683.
- Wu, X.S., McNeil, B.D., Xu, J., Fan, J., Xue, L., Melicoff, E., Adachi, R., Bai, L., and Wu, L.G. (2009).  $Ca^{2+}$  and calmodulin initiate all forms of endocytosis during depolarization at a nerve terminal. *Nat. Neurosci.* *12*, 1003–1010.
- Yamashita, T., Hige, T., and Takahashi, T. (2005). Vesicle endocytosis requires dynamin-dependent GTP hydrolysis at a fast CNS synapse. *Science* *307*, 124–127.
- Yamashita, T., Eguchi, K., Saitoh, N., von Gersdorff, H., and Takahashi, T. (2010). Developmental shift to a mechanism of synaptic vesicle endocytosis requiring nanodomain  $Ca^{2+}$ . *Nat. Neurosci.* *13*, 838–844.

## 4 Diskussion und Ausblick

In der vorliegenden Arbeit konnten verschiedene fundamentale Mechanismen aufgeschlüsselt werden, die eine synaptische Übertragung an einer zentralen Synapse mit einer Frequenz im Kilohertz-Bereich ermöglichen. Durch die Etablierung und Anwendung hochauflösender elektrophysiologischer und optischer Messmethoden auf subzellulärer Ebene war es möglich, hochfrequente Übertragung im Detail zu analysieren. Im Folgenden werden die gewonnenen Erkenntnisse dargestellt und ihre Bedeutung für das Verständnis neuronaler Signalverarbeitung diskutiert.

### 4.1 Die Mechanismen hochfrequenter synaptischer Übertragung

An der zerebellären Moosfaser-Körnerzell-Synapse wurden *in vivo* bereits hohe Aktionspotenzialfrequenzen und eine zuverlässige synaptische Übertragung beschrieben (Rancz et al., 2007). Mit der Kombination von prä- und postsynaptischen Patch-Clamp Ableitungen im akuten Hirnschnittpräparat wurde nun nachgewiesen, dass diese Synapse Informationen mit Frequenzen von bis zu 1 kHz auf die postsynaptische Zelle übertragen kann (Ritzau-Jost et al., 2014). Außerdem konnten präsynaptisch Aktionspotenzialfrequenzen von bis zu 1,6 kHz gemessen werden (Ritzau-Jost et al., 2014). Die Mechanismen, welche dieser außergewöhnlich schnellen Signalübertragung zugrunde liegen, wurden in mehreren Arbeiten untersucht.

Verschiedene funktionelle Spezialisierungen der präsynaptischen MFB erlauben eine schnelle Abfolge von Aktionspotenzialen (Kapitel 3.1). Zum einen haben die präsynaptischen Aktionspotenziale eine Dauer von nur etwa 100  $\mu$ s (Ritzau-Jost et al., 2014). Diese Dauer ist kürzer als bei allen bisher gemessenen Aktionspotenzialen in Nervenzellen. Eine detaillierte Analyse der Ionenströme an MFB mit Hilfe von Ableitungen in der *Outside-Out* Konfiguration ergab, dass die Na<sup>+</sup>- und K<sup>+</sup>-Ströme während eines Aktionspotenzials an dieser präsynaptischen

Nervenendigung von besonders kurzer Dauer sind. Der  $K^+$ -Strom an MFB wird durch Kanäle des  $K_v1$ - und  $K_v3$ -Subtyps vermittelt und die  $Na^+$ -Kanäle sind durch eine schnelle Inaktivierung charakterisiert. Aus diesen Eigenschaften der präsynaptischen Ionenkanäle resultiert auch eine geringe Überlagerung von  $Na^+$ - und  $K^+$ -Strom (Ritzau-Jost et al., 2014). Üblicherweise gehen kürzere Aktionspotenziale mit einer größeren Überlagerung von  $Na^+$ - und  $K^+$ -Strom einher, weshalb die metabolische Effizienz mit der Aktionspotenzialdauer sinkt (Carter und Bean, 2009, 2011). Die geringe Überlagerung und damit relativ hohe metabolische Effizienz in MFB ist daher erstaunlich. Eine weitere Besonderheit der Aktionspotenziale in MFB ist, dass sie trotz ihrer kurzen Dauer sehr effektiv präsynaptische  $Ca^{2+}$ -Kanäle öffnen können (Ritzau-Jost et al., 2014; Sabatini und Regehr, 1996).

Die  $Ca^{2+}$ -Ionen, die während eines Aktionspotenzial in eine präsynaptische Nervenendigung einströmen, werden im Allgemeinen schnell von endogenen  $Ca^{2+}$ -Puffern gebunden (Schwaller, 2010). Die  $Ca^{2+}$ -Bindungskapazität und Affinität der endogenen Puffer bestimmen daher entscheidend die Dynamik der intrazellulären  $Ca^{2+}$ -Signale. Um diese Eigenschaften der präsynaptischen  $Ca^{2+}$ -Pufferung und ihre Bedeutung für synaptische Übertragung besser zu verstehen, wurden quantitative  $Ca^{2+}$ -Konzentrationsmessungen mit Zwei-Photonenmikroskopie an MFB etabliert (Delvendahl et al., 2015a). Die Messungen von durch einzelne Aktionspotenziale ausgelösten  $Ca^{2+}$ -Signalen ergaben, dass die  $Ca^{2+}$ -Bindungskapazität der immobilen Pufferfraktion in MFB vergleichsweise gering ist (Kapitel 3.2), was eine sehr schnelle Abnahme der  $Ca^{2+}$ -Konzentration an der aktiven Zone zur Folge hat (Delvendahl et al., 2015a). Dies bedingt eine hohe zeitliche und räumliche Präzision der lokalen  $Ca^{2+}$ -Signale an der aktiven Zone und kann die hochgradig synchrone Freisetzung von Vesikeln an MFB erklären. Außerdem trägt ein mobiler endogener  $Ca^{2+}$ -Puffer mit langsamer Kinetik dazu bei, eine Aufsummierung von  $Ca^{2+}$ -Ionen während repetitiver Aktionspotenziale zu verringern, und unterstützt damit die hochfrequente Signalübertragung (Delvendahl et al., 2015a). Ein weiterer Faktor, der eine schnelle und dennoch synchrone Vesikelfreisetzung vermittelt, ist die geringe

Distanz zwischen  $\text{Ca}^{2+}$ -Kanälen und Vesikeln, die am MFB auf nur etwa 20 nm geschätzt wird (Delvendahl et al., 2015a; Ritzau-Jost et al., 2014).

Um eine Neurotransmitterfreisetzung mit hoher Frequenz aufrecht zu erhalten, kann ein MFB auf einen Vorrat von insgesamt etwa 200.000 Vesikeln zurückgreifen (Jakab und Hátori, 1988). Die Anzahl an unmittelbar freisetzbaren Vesikeln pro synaptische Verbindung beträgt ca. 5–10, wovon jedes Vesikel aus einem Vorrat von etwa 300 freisetzbaren Vesikeln nachgeladen werden kann (Hallermann et al., 2010; Saviane und Silver, 2006). Die Rate dieser Vesikelrekrutierung ist sehr schnell und konnte in direkten Messungen auf  $30 \text{ s}^{-1}$  geschätzt werden (Ritzau-Jost et al., 2014). Die schnelle Vesikelrekrutierung an MFB unterstützt somit eine hochfrequente Transmitterfreisetzung.

Nach der Fusion synaptischer Vesikel wird die vergrößerte Membranfläche durch Endozytose wieder reduziert und es werden neue Vesikel gebildet. Die Geschwindigkeit dieses Prozesses wird bisher kontrovers diskutiert (Kononenko und Haucke, 2015; Watanabe et al., 2013; Wu et al., 2014). In neuronalen Zellkulturen wurde mittels elektronenmikroskopischen Techniken („Flash-and-Freeze“) ein extrem schneller Zeitverlauf der Endozytose bei physiologischer Temperatur gezeigt (Watanabe et al., 2013), ohne jedoch diesen Prozess detailliert über die Zeit beobachten zu können. Die zerebelläre Moosfaser-Körnerzell-Synapse bietet die Möglichkeit, zeitlich hochaufgelöste Messungen der präsynaptischen Membrankapazität ( $C_m$ ) durchzuführen und dadurch detaillierte Erkenntnisse über Exo- und Endozytose zu gewinnen. Mit optimierten Messbedingungen gelang es am MFB, die Endozytose nach einzelnen Aktionspotenzialen zu untersuchen und zu quantifizieren (Kapitel 3.4). Dabei zeigte sich, dass an dieser Synapse der Zeitverlauf der Endozytose nach einem einzelnen Aktionspotenzial sehr schnell ist; die Membrankapazität zeigte eine Abnahme mit einer Zeitkonstante von etwa 500 ms (Delvendahl et al., 2016). Um herauszufinden, welche molekularen Mechanismen dieser schnellen Form der Endozytose zu Grunde liegen, wurden mehrere Proteine pharmakologisch inhibiert, die an Präsynapsen eine Membraneinstülpung und –abschnürung vermitteln können. Die sehr schnelle Endozytose an MFB wurde durch einen Inhibitor der GTPase Dynamin und eine Inhibition der Polymerisation von Actin

deutlich verlangsamt (Delvendahl et al., 2016). Eine pharmakologische Blockierung von Clathrin hatte dagegen keinen Einfluss auf den Zeitverlauf der Endozytose nach einem Aktionspotenzial (Delvendahl et al., 2016). Die schnelle Endozytose an MFB benötigt demnach Dynamin und polymerisiertes Actin, ist jedoch unabhängig von einer Wirkung von Clathrin. Eine Abfolge von Aktionspotenzialen mit 300 Hz führte zu einer Verlangsamung der Endozytose, was darauf hindeutet, dass ein hohes Maß an neuronaler Aktivität zusätzliche Formen der Endozytose mit möglicherweise unterschiedlichen molekularen Mechanismen benötigt.

Neben den in dieser Arbeit hauptsächlich untersuchten präsynaptischen Mechanismen sind auch die Eigenschaften der postsynaptischen Körnerzellen für eine hochfrequente Signalübertragung an der Moosfaser-Körnerzell-Synapse von Bedeutung. Zum einen haben die exzitatorischen postsynaptischen Ströme (EPSC) eine besonders schnelle Kinetik (Silver et al., 1992), was durch die GluA2 und GluA4 Untereinheiten der Glutamatrezeptoren vom AMPA-Typ an Körnerzellen vermittelt wird (Cathala et al., 2005). Diese AMPA-Rezeptoren desensibilisieren langsam und zeigen auch eine schnelle Erholung von einer Desensibilisierung (DiGregorio et al., 2007). Diese relative Beständigkeit gegen Desensibilisierung unterstützt eine hochfrequente Übertragung, unter der es zu einer Ansammlung von Glutamat im synaptischen Spalt kommt. Außerdem kann es zu einer überlaufenden Wirkung des Glutamats von eng benachbarten Freisetzungstellen kommen („Spillover“). Diese Spillover-Ströme haben eine geringe Variabilität und vergrößern den Ladungstransfer unter repetitiver synaptischer Aktivität, wodurch sich die Zuverlässigkeit der Übertragung erhöht (DiGregorio et al., 2002).

Auch die anatomische Struktur der Moosfaser-Körnerzell-Synapse trägt zur hochfrequenten synaptischen Übertragung bei. Die Synapse hat eine kompakte Ultrastruktur mit mehreren Kontaktstellen pro Dendrit einer Körnerzelle (Cathala et al., 2005), wodurch der Zeitverlauf der EPSC beschleunigt wird. Außerdem ist die Anatomie der Körnerzellen optimal für eine schnelle Integration hochfrequenter Informationen. Das kleine Soma und die kurzen Dendriten



machen Körnerzellen elektrotonisch äußerst kompakt, wobei sich Soma und Dendriten wie ein einziges elektrisches Kompartiment verhalten (D'Angelo et al., 1993; Silver et al., 1992). Die Etablierung von dendritischen Ableitungen an Körnerzellen (Kapitel 3.3) ermöglichte, direkt nachzuweisen, dass postsynaptische Potenziale aufgrund der elektrotonischen Eigenschaften der Dendriten nur einer sehr geringen Filterung unterworfen sind (Delvendahl et al., 2015b). Die kompakten elektrotonischen Eigenschaften von Körnerzellen sind demnach optimal geeignet, um synaptische Eingänge effizient zu integrieren.

Diese prä- und postsynaptischen Charakteristika ermöglichen gemeinsam die außergewöhnlich schnelle und hochfrequente Signalübertragung mit hoher Genauigkeit an der zerebellären Moosfaser-Körnerzell-Synapse (Abbildung 4). Die hier dargestellten Arbeiten leisten dabei einen wesentlichen Beitrag zum Verständnis der Mechanismen hochfrequenter Signalübertragung.

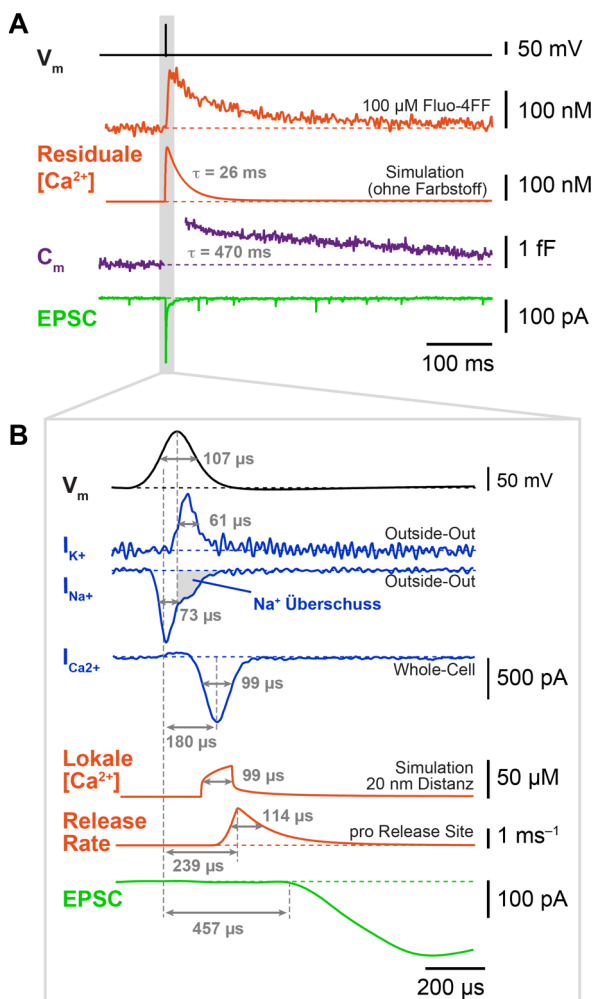


#### Abb. 4: Mechanismen schneller Übertragung an der Moosfaser-Körnerzell-Synapse

(A) Ein präsynaptisches Aktionspotential ( $V_m$ , schwarz) führt zu einer Erhöhung der residualen  $Ca^{2+}$ -Konzentration (orange), welche mit einer Zeitkonstante von ca. 26 ms wieder abfällt (Simulation). Die Zeitkonstante der Endozytose beträgt ca. 470 ms, gemessen über die Änderungen der Membrankapazität ( $C_m$ , violett). Die  $Ca^{2+}$ -vermittelte Freisetzung von Vesikeln führt zu einem exzitatorischen postsynaptischen Strom in der Körnerzelle (EPSC, grün).

(B) Detaillierter Zeitablauf der synaptischen Übertragung. Schwarz: Präsynaptisches Aktionspotential; Blau: Zugehörige, pharmakologisch isolierte, präsynaptische Ionenströme ( $Na^+$ ,  $K^+$ ,  $Ca^{2+}$ ); Orange: Lokale  $Ca^{2+}$ -Konzentration und Freisetzungsrates synaptischer Vesikel; Grün: Postsynaptischer Strom. Die extrem kurzen Aktionspotenziale, schnellen Ionenkanäle, eine geringe  $Ca^{2+}$ -Pufferung und eine enge Kopplungsdistanz führen zu einer Verzögerung in der synaptischen Übertragung von lediglich ca. 450  $\mu$ s.

Abbildung modifiziert nach Ritzau-Jost et al. (2014), Delvendahl et al. (2015a) und Delvendahl et al. (2016).

## 4.2 Bedeutung hochfrequenter Signalübertragung für neuronale Signalverarbeitung

Frühere *in vivo* Arbeiten konnten mit Hilfe extrazellulärer Ableitungen bei Affen und Katzen demonstrieren, dass Moosfaseraxone ratenkodierte Informationen von kontinuierlichen sensorischen Variablen übermitteln (Abbildung 5; van Kan et al., 1993; Garwicz et al., 1998). Zum Beispiel ist die Änderung eines Gelenkwinkels mit einer Änderung der Feuerfrequenz von Moosfasern verbunden, die dabei typischerweise im Bereich von 10–200 Hz feuern (van Kan et al., 1993). Spätere Ableitungen von Körnerzellen in anästhesierten Mäusen zeigten in Übereinstimmung, dass vestibuläre Informationen wie beispielsweise die Rotationsgeschwindigkeit, von Moosfasern mittels kontinuierlicher Ratenkodierung mit einem hochgradig linearen Verhältnis zwischen Geschwindigkeit und Ladungstransfer übermittelt wird (Arenz et al., 2008). Im Gegensatz dazu zeigen Moosfasern, die Informationen über diskrete sensorische Ereignisse vermitteln, ein anderes Feuerverhalten (Garwicz et al., 1998; Rancz et al., 2007). So besteht die sensorische Antwort auf einen Luftstoß als Stimulation aus kurzen Signalfolgen mit einer Frequenz von bis zu einem Kilohertz (Rancz et al., 2007). Direkte Ableitungen von MFB in Mäusen während Lokomotion weisen zusätzlich darauf hin, dass manche Moosfasern von einem spärlichen Feuerverhalten zu einer dichten Gangkodierung unter Bewegung wechseln können (Powell et al., 2015). Wie diese Informationen auf Körnerzellen übertragen werden, wurde ebenfalls *in vivo* untersucht. Körnerzellen haben nur eine geringe spontane Aktivität im Bereich von weniger als einem Hertz (Chadderton et al., 2004), können aber während sensorischer Stimulation kurze Signalfolgen mit Frequenzen bis in den Kilohertz-Bereich feuern (Chadderton et al., 2004; Jörntell und Ekerot, 2006; Powell et al., 2015; Rancz et al., 2007). Um Aktionspotenziale in Körnerzellen auszulösen, ist eine Summierung von exzitatorischen postsynaptischen Potenzialen notwendig (Chadderton et al., 2004), was durch Spillover-Ströme unterstützt wird (Powell et al., 2015). Sowohl Moosfasern als auch Körnerzellen weisen demnach *in vivo* verschiedene Aktivitätsmuster auf, insbesondere auch hochfrequenten Feuerraten bis in den Kilohertz-Bereich.

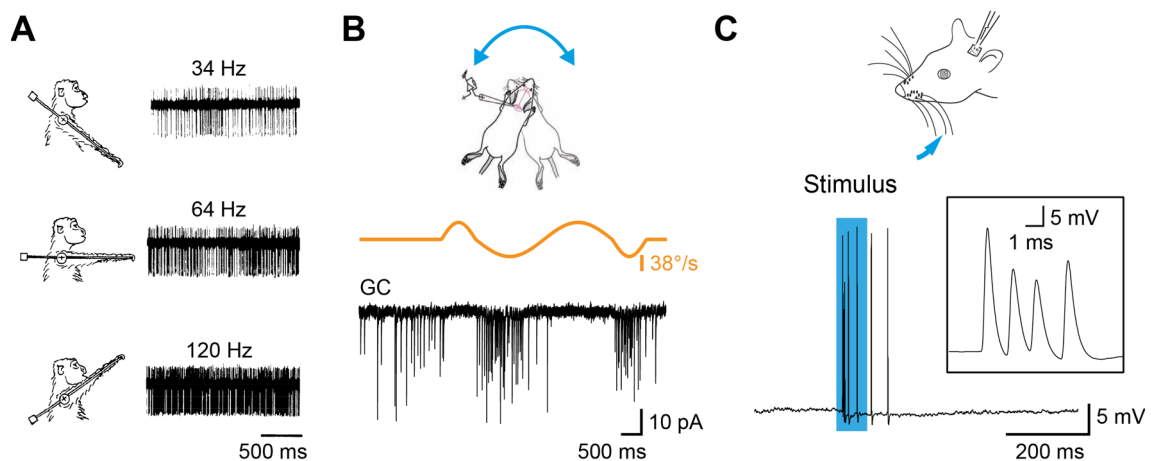


**Abb. 5: Sensorische Signalübertragung durch zerebelläre Moosfasern**

(A) Änderungen des Gelenkwinkels spiegeln sich in der Feuerfrequenz von Moosfasern im Bereich von ca. 10–200 Hz wider. Extrazelluläre Ableitung in wachen Affen, modifiziert nach van Kan et al. (1993). (B) Das Feuerverhalten von Moosfasern (schwarz, gemessen als EPSC in Körnerzellen) kodiert linear die Rotationsgeschwindigkeit in anästhesierten Mäusen (orange). Modifiziert nach Arenz et al. (2008). (C) Stimulation mittels eines Luftstoßes führt zu einer messbaren Antwort in MFB, welche die sensorische Information als kurze, hochfrequente Signalfolge weiterleitet. Die ersten Aktionspotenziale während des Stimulus sind rechts vergrößert dargestellt. Präsynaptische *in vivo* Ableitung in anästhesierten Ratten, modifiziert nach Rancz et al. (2007).

Aus einer Netzwerkperspektive besteht die Hauptfunktion der Moosfaser-Körnerzell-Synapse darin, sensorische Informationen und Efferenzkopien auf Körnerzellen zu übertragen. Diese Aufgabe erscheint besonders herausfordernd, nicht nur aufgrund der Vielzahl an neuronalen Signalen, die eine hohe Bandbreite abdecken, sondern auch wegen der extrem großen Zahl an Körnerzellen, die weit über die Hälfte aller Neurone im menschlichen Gehirn ausmachen (Williams und Herrup, 1988). Man geht davon aus, dass Körnerzellen Muster in Moosfaser-Eingängen erkennen (Marr, 1969), was in einer spärlicheren, höher-dimensionalen Kodierung im Vergleich zu Moosfasern resultiert (Billings et al., 2014). Die zeitliche Präzision und Zuverlässigkeit der Moosfaser-Körnerzell-Synapse ist von hoher Bedeutung für die zuverlässige Detektierung schneller Signale innerhalb eines bestimmten Zeitfensters (D'Angelo und De Zeeuw, 2009), für adaptive Filterung (Dean et al., 2010;

Jörntell und Ekerot, 2006) und für einen Abgleich von motorischer Kopie und sensorischer Information (Kennedy et al., 2014). Unabhängig von der diversen und teilweise kontroversen Funktion des zerebellären Kortex, vermittelt die Moosfaser-Körnerzell-Synapse sensorische Signale mit einer erstaunlichen Bandbreite an die numerisch größte Population von Neuronen in unserem Gehirn.

### **4.3 Übertragbarkeit auf andere Synapsen**

Die zerebelläre Moosfaser-Körnerzell-Synapse ist mit Sicherheit für ihre Funktion innerhalb des zerebellären Kortex spezialisiert. Um die Frage nach einer Übertragbarkeit der hier an der Moosfaser-Körnerzell-Synapse gewonnenen Erkenntnisse zu beantworten, ist ein Vergleich mit anderen Synapsen notwendig. Eine detaillierte elektrophysiologische Charakterisierung der synaptischen Übertragung wurde vor allem an der Held'schen Calyx durchgeführt, einer großen, kelchartigen Synapse im auditorischen Hirnstamm (Borst und Soria van Hove, 2012). Diese Synapse ist für die Übertragung afferenter Information aus der Cochlea zuständig und spielt eine wichtige Rolle bei der Lokalisation von Geräuschen. Die Calyx-Synapse zeigt ebenfalls eine Übertragung mit hohen Frequenzen im Bereich von einigen 100 Hz. Viele Parameter der synaptischen Übertragung wurden inzwischen sowohl an der Calyx als auch am MFB bestimmt (Tabelle 1). Die beiden Synapsen unterscheiden sich in einigen funktionellen Parametern, wobei die MFB-Synapse eine kürzere Aktionspotenzialdauer, eine höhere Wahrscheinlichkeit der Vesikelfreisetzung (Release Probability) und eine größere Anzahl an freisetzbaren Vesikeln aufweist. Manche dieser funktionellen Unterschiede zwischen MFB- und Calyx-Synapse können durch die offensichtlichen Unterschiede in der Anatomie der zwei Synapsen erklärt werden: MFB sind kleiner und haben weniger und kleinere aktive Zonen. Zusätzlich übertragen die aktiven Zonen eines MFB auf 10–100 postsynaptische Zellen, wohingegen die Held'sche Calyx alle ihre aktiven Zonen nutzt, um mit einem

postsynaptischen Neuron zu kommunizieren. Diese anatomischen Rahmenbedingungen könnten der Grund dafür sein, dass MFB eine höhere Release Probability, einen kleineren Pool an freisetzbaren Vesikeln sowie eine schnelle Nachladerate der Vesikel benutzen müssen (Hallermann und Silver, 2013).

Andere Unterschiede zwischen den zwei gut charakterisierten Synapsen mögen jedoch nur apparent sein. Verschiedenheiten in den Messbedingungen in Studien an den jeweiligen Synapsen könnten für abweichende Werte bei den gemessenen Parametern verantwortlich sein. So wurden die hier zusammengefassten Arbeiten am MFB alle an adulten Tieren durchgeführt, während die meisten Arbeiten an der Held'schen Calyx junge, unreife Tiere verwendeten. Patch-Clamp Ableitungen von adulten Calyx-Synapsen werden durch morphologische Veränderungen in der Entwicklung erschwert, da die präsynaptische Nervenendigung eine komplexe, finger-ähnliche Struktur annimmt (Wang et al. (2008) gelangen Ableitungen von Calyx-Synapsen bei 19 Tage alten Tieren). Außerdem wurden Untersuchungen am MFB der letzten Zeit bei physiologischen Temperaturen durchgeführt, während viele der Studien ihre Messungen an der Held'schen Calyx bei Raumtemperatur ausführten (Leão et al. (2005) zum Beispiel machten jedoch Messungen bei physiologischer Temperatur).

Sowohl der Entwicklungsstatus der Synapse als auch die Temperatur haben einen großen Einfluss auf die Geschwindigkeit der gemessenen Parameter (Nakamura et al., 2015; Renden und von Gersdorff, 2007; Wang et al., 2008). So ist beispielsweise die Dauer der Aktionspotenziale bei halbmaximaler Amplitude von ca.  $100 \mu\text{s}$  in MFB (Ritzau-Jost et al., 2014) deutlich schneller als vorhergegangene Messungen an der Calyx-Synapse, aber auf Basis von Studien unterschiedlicher Entwicklungszustände bei physiologischer Temperatur wurde eine ähnlich kurze Aktionspotenzialdauer für die Held'sche Calyx postuliert (Taschenberger und von Gersdorff, 2000). Demnach könnten die Unterschiede zwischen MFB und Calyx in zum Beispiel der Aktionspotenzialdauer lediglich apparent sein.



**Tabelle 1: Präsynaptische Parameter von MFB und Held'scher Calyx Synapse**

Parameter	Einheit	MFB	Held'sche Calyx	Referenzen
Membrankapazität ( $C_m$ )	pF	3–4	20–25	(Borst und Sakmann, 1998; Delvendahl et al., 2016; Rancz et al., 2007; Ritzau-Jost et al., 2014)
Anzahl an aktiven Zonen		150–300	500–700	(Kim et al., 2013; Sätzler et al., 2002; Taschenberger et al., 2002; Xu-Friedman und Regehr, 2003)
Größe der aktiven Zonen	$\mu\text{m}^2$	0.04	0.07–0.1	(Sätzler et al., 2002; Xu-Friedman und Regehr, 2003)
Konnektivität		1:10–1:100	1:1	(Eccles et al., 1967; Hoffpauir et al., 2006; Jakob und Hámori, 1988; Ritzau-Jost et al., 2014)
Dauer des AP bei halber Amplitude	$\mu\text{s}$	~110	200–500	(Ritzau-Jost et al., 2014; Taschenberger und von Gersdorff, 2000)
Metabolische Effizienz des AP		~1.8	Kein $\text{Na}^+$ -Strom	(Leão et al., 2005; Ritzau-Jost et al., 2014)
EPSC Amplitude	pA	30–100	2.000–10.000	(Sargent et al., 2005; Saviane und Silver, 2006; Scheuss et al., 2002; Silver et al., 1992; Wang et al., 2008)
Release Probability ( $p_r$ )		0.4–0.6	0.05–0.1	(Hallermann et al., 2010; Hosoi et al., 2007; Sargent et al., 2005; Saviane und Silver, 2006; Schneggenburger und Neher, 2000)
$\text{Ca}^{2+}$ -Kanal-Vesikel Kopplungs-Distanz	nm	~20	>20–30	(Delvendahl et al., 2015a; Fedchyshyn und Wang, 2005; Nakamura et al., 2015; Ritzau-Jost et al., 2014)
Freisetzbarer Pool (RRP) pro post-synaptischer Zelle		5–10	700–5.000	(Hallermann et al., 2010; Saviane und Silver, 2006; Taschenberger et al., 2002; Taschenberger et al., 2005; Wang et al., 2008)
RRP Auffüllungsrate	$\text{ms}^{-1}$	30–80	3–11	(Kushmerick et al., 2006; Ritzau-Jost et al., 2014; Saviane und Silver, 2006)
Quantal Size (q)	pA	12–17	24–150	(Hallermann et al., 2010; Sargent et al., 2005; Saviane und Silver, 2006; Scheuss et al., 2002; Wang et al., 2008)
Quantal Content (QC)		3–6	40–50	(Hallermann et al., 2010; Sargent et al., 2005; Saviane und Silver, 2006; Taschenberger et al., 2005)
Exozytose-Effizienz	$\text{fF pC}^{-1}$	~65	~45	(Delvendahl et al., 2016; Taschenberger et al., 2002)
$\text{Ca}^{2+}$ -Stromdichte	$\text{pA pF}^{-1}$	~145	~70	(Delvendahl et al., 2016; Han et al., 2015)
Residuale $[\text{Ca}^{2+}]$ , Amplitude, AP	nM	~220	~500	(Delvendahl et al., 2015a; Helmchen et al., 1997)
Residuale $[\text{Ca}^{2+}]$ , Zeitkonstante, AP	ms	~25	~45	(Delvendahl et al., 2015a; Helmchen et al., 1997)
$\kappa_E$ , immobilierter Puffer		~15	~45	(Delvendahl et al., 2015a; Helmchen et al., 1997)
$\kappa_E$ , mobiler Puffer		$\cong 100 \mu\text{M}$ EGTA	$\cong 100 \mu\text{M}$ EGTA	(Delvendahl et al., 2015a; Müller et al., 2007)

Abkürzungen: AP, Aktionspotenzial;  $C_m$ , Zellmembrankapazität;  $\kappa_E$ ,  $\text{Ca}^{2+}$ -Bindungs-Ratio;  $[\text{Ca}^{2+}]$ ,  $\text{Ca}^{2+}$ -Konzentration; EGTA, Ethylenglycol-bis(aminoethylether)-N,N,N',N'-tetraessigsäure; EPSC, exzitatorischer postsynaptischer Strom; MFB, Moosfaserbouton;  $p_r$ , Freisetzungswahrscheinlichkeit; RRP, Release-Ready Pool.

Insgesamt lässt sich sagen, dass mehrere anatomische und funktionelle Unterschiede zwischen zerebellärer Moosfaser-Körnerzell-Synapse und Held'scher Calyx existieren. Viele funktionelle Parameter sind jedoch höchstwahrscheinlich ähnlicher, als es ein einfacher Vergleich der Literaturwerte impliziert. Die relative Ähnlichkeit vieler synaptischer Messgrößen bei diesen zwei hochfrequenten Synapsen legt es zudem nahe, dass die beschriebenen Mechanismen der synaptischen Übertragung mit hohen Frequenzen ein generelles Prinzip darstellen, das von vielen Synapsen genutzt werden könnte. Viele der in den hier zusammengefassten Studien gemessenen Parameter wurden bereits an der Held'schen Calyx bestimmt. Die gründliche elektrophysiologische Charakterisierung der Moosfaser-Körnerzell-Synapse erlaubt zum einen den direkten Vergleich zweier hochfrequenter Synapsen und kann damit wichtige Erkenntnisse über generelle Mechanismen synaptischer Übertragung mit hohen Frequenzen liefern. Zum anderen ist die Moosfaser-Körnerzell-Synapse durch einen hohen Grad an Divergenz gekennzeichnet, besitzt wenige aktive Zonen pro postsynaptischer Zelle und erfüllt höchstwahrscheinlich eine komplexere Funktion innerhalb des neuronalen Netzwerks, so dass Erkenntnisse von dieser Synapse zum besseren Verständnis synaptischer Übertragung in neuronalen Netzwerken beitragen können.

#### **4.4 Zusammenfassung und Ausblick**

Die hochfrequente Signalübertragung spielt eine bedeutende Rolle an vielen Stellen im Zentralnervensystem. Generell steigt die Geschwindigkeit der Informationsverarbeitung durch höhere Frequenzen von Aktionspotenzialen und synaptischer Übertragung. Außerdem erhöht die Möglichkeit höhere Aktionspotenzialfrequenzen zu nutzen, die Bandbreite an kodierbarer Information in einem ratenkodierenden System. Die schnellste bis dato beschriebene Signalübertragung an zentralen Synapsen findet an der zerebellären Moosfaser-Körnerzell-Synapse statt. Mehrere mechanistische Spezialisierungen

ermöglichen dort eine präzise und schnelle Übertragung von Informationen mit sehr hohen Raten. Diese Spezialisierungen umfassen extrem schnelle Aktionspotenziale, eine geringe endogene  $\text{Ca}^{2+}$ -Pufferung, eine enge Kopplung zwischen  $\text{Ca}^{2+}$ -Kanälen und Vesikeln, eine schnelle Vesikelnachladung aus einem großen Pool freisetzbarer Vesikel, sehr schnelle Endozytose und schnelle postsynaptische Glutamatrezeptoren.

Da außerdem prä- und postsynaptische Ableitungen an der Moosfaser-Körnerzell-Synapse *in vivo* möglich sind, konnten bis zum heutigen Zeitpunkt bereits viele wichtige Informationen über die Funktion dieser Synapse bei sensorischer Signalverarbeitung gewonnen werden. Damit ist die zerebelläre Moosfaser-Körnerzell-Synapse ein ideales Modell zur Untersuchung hochfrequenter Signalübertragung und ihrer Bedeutung für neuronale Informationsverarbeitung. Die hier dargestellten Studien mit hochauflösenden elektrophysiologischen und optischen Methoden konnten wichtige Mechanismen beschreiben, die für eine schnelle und zuverlässige synaptische Übertragung verantwortlich sind.

Zukünftige Studien werden unser Verständnis von hochfrequenter Signalübertragung noch erweitern. So ist zum jetzigen Zeitpunkt unklar, welche Spezialisierungen auf ultrastruktureller Ebene für eine hochfrequente Signalübertragung verantwortlich sind. In diesem Zusammenhang könnten hochauflösende Mikroskopietechniken (Ehmann et al., 2014; Nanguneri et al., 2012) die Struktur-Funktionsbeziehung hochfrequenter Synapsen aufschlüsseln. Die Anwendung genetischer Methoden (Kalinovsky et al., 2011) könnte dabei helfen, die molekularen Grundlagen synaptischer Übertragung weiter aufzuklären, während schnelle 3D-Bildgebungsverfahren (Fernández-Alfonso et al., 2014; Katona et al., 2012) eine Untersuchung hochfrequenter Signalübertragung in neuronalen Netzwerken ermöglichen sollten. Zuletzt sind präsynaptische Ableitung in sich bewegenden Mäusen (Powell et al., 2015) geeignet, um hochfrequente Signalübertragung zum Beispiel während der Orientierung in *Virtual-Reality* Umgebungen (Schmidt-Hieber und Häusser, 2013) zu untersuchen. Zukünftige Studien mit Anwendung unter anderem der

genannten Methoden haben daher die Möglichkeit, die Mechanismen hochfrequenter Signalübertragung und deren Bedeutung innerhalb neuronaler Netzwerke weiter zu beleuchten.

## 5 Literaturverzeichnis

- Adrian, E.D., und Bronk, D.W. (1929). The discharge of impulses in motor nerve fibres: Part II. The frequency of discharge in reflex and voluntary contractions. *J. Physiol.* *67*, 119–151.
- Adrian, E.D., und Zotterman, Y. (1926). The impulses produced by sensory nerve-endings: Part II. The response of a Single End-Organ. *J. Physiol.* *61*, 151–171.
- Arenz, A., Silver, R.A., Schaefer, A.T., und Margrie, T.W. (2008). The contribution of single synapses to sensory representation in vivo. *Science* *321*, 977–980.
- Bale, M.R., Campagner, D., Erskine, A., und Petersen, R.S. (2015). Microsecond-scale timing precision in rodent trigeminal primary afferents. *J. Neurosci.* *35*, 5935–5940.
- Billings, G., Piasini, E., Lorincz, A., Nusser, Z., und Silver, R.A. (2014). Network structure within the cerebellar input layer enables lossless sparse encoding. *Neuron* *83*, 960–974.
- Blosa, M., Sonntag, M., Jager, C., Weigel, S., Seeger, J., Frischknecht, R., Seidenbecher, C.I., Matthews, R.T., Arendt, T., Rübtsamen, R., und Morawski, M. (2015). The extracellular matrix molecule brevican is an integral component of the machinery mediating fast synaptic transmission at the calyx of Held. *J. Physiol.* *593*, 4341–4360.
- Borst, J.G., und Sakmann, B. (1998). Calcium current during a single action potential in a large presynaptic terminal of the rat brainstem. *J. Physiol.* *506*, 143–157.
- Borst, J.G., und Soria van Hoeve, J. (2012). The calyx of Held synapse: from model synapse to auditory relay. *Annu. Rev. Physiol.* *74*, 199–224.
- Carter, B.C., und Bean, B.P. (2009). Sodium entry during action potentials of mammalian neurons: incomplete inactivation and reduced metabolic efficiency in fast-spiking neurons. *Neuron* *64*, 898–909.
- Carter, B.C., und Bean, B.P. (2011). Incomplete inactivation and rapid recovery of voltage-dependent sodium channels during high-frequency firing in cerebellar Purkinje neurons. *J. Neurophysiol.* *105*, 860–871.
- Cathala, L., Brickley, S., Cull-Candy, S., und Farrant, M. (2003). Maturation of EPSCs and intrinsic membrane properties enhances precision at a cerebellar synapse. *J. Neurosci.* *23*, 6074–6085.
- Cathala, L., Holderith, N.B., Nusser, Z., DiGregorio, D.A., und Cull-Candy, S.G. (2005). Changes in synaptic structure underlie the developmental speeding of AMPA receptor-mediated EPSCs. *Nat. Neurosci.* *8*, 1310–1318.
- Chabrol, F.P., Arenz, A., Wiechert, M.T., Margrie, T.W., und DiGregorio, D.A. (2015). Synaptic diversity enables temporal coding of coincident multisensory inputs in single neurons. *Nat. Neurosci.* *18*, 718–727.



- Chadderton, P., Margrie, T.W., und Häusser, M. (2004). Integration of quanta in cerebellar granule cells during sensory processing. *Nature* *428*, 856–860.
- D'Angelo, E., und De Zeeuw, C.I. (2009). Timing and plasticity in the cerebellum: focus on the granular layer. *Trends Neurosci.* *32*, 30–40.
- D'Angelo, E., Rossi, P., und Taglietti, V. (1993). Different proportions of N-methyl-D-aspartate and non-N-methyl-D-aspartate receptor currents at the mossy fibre-granule cell synapse of developing rat cerebellum. *Neuroscience* *53*, 121–130.
- Dean, P., Porrill, J., Ekerot, C.F., und Jörntell, H. (2010). The cerebellar microcircuit as an adaptive filter: experimental and computational evidence. *Nat. Rev. Neurosci.* *11*, 30–43.
- Delvendahl, I., Jablonski, L., Baade, C., Matveev, V., Neher, E., und Hallermann, S. (2015a). Reduced endogenous  $\text{Ca}^{2+}$  buffering speeds active zone  $\text{Ca}^{2+}$  signaling. *Proc. Natl. Acad. Sci. USA* *112*, E3075–3084.
- Delvendahl, I., Straub, I., und Hallermann, S. (2015b). Dendritic patch-clamp recordings from cerebellar granule cells demonstrate electrotonic compactness. *Front. Cell. Neurosci.* *9*, 93.
- Delvendahl, I., Vyleta, N.P., von Gersdorff, H., und Hallermann, S. (2016). Fast, Temperature-Sensitive and Clathrin-Independent Endocytosis at Central Synapses. *Neuron* *90*, 492–498.
- DiGregorio, D.A., Nusser, Z., und Silver, R.A. (2002). Spillover of glutamate onto synaptic AMPA receptors enhances fast transmission at a cerebellar synapse. *Neuron* *35*, 521–533.
- DiGregorio, D.A., Rothman, J.S., Nielsen, T.A., und Silver, R.A. (2007). Desensitization properties of AMPA receptors at the cerebellar mossy fiber granule cell synapse. *J. Neurosci.* *27*, 8344–8357.
- Eccles, J.C., Ito, M., und Szentagothai, J. (1967). *The Cerebellum as a Neuronal Machine* (New York: Springer Verlag).
- Ehmann, N., van de Linde, S., Alon, A., Ljaschenko, D., Keung, X.Z., Holm, T., Rings, A., DiAntonio, A., Hallermann, S., Ashery, U., *et al.* (2014). Quantitative super-resolution imaging of Bruchpilot distinguishes active zone states. *Nat. Commun.* *5*, 4650.
- Fedchyshyn, M.J., und Wang, L.Y. (2005). Developmental transformation of the release modality at the calyx of Held synapse. *J. Neurosci.* *25*, 4131–4140.
- Fernández-Alfonso, T., Nadella, K.M., Iacaruso, M.F., Pichler, B., Roš, H., Kirkby, P.A., und Silver, R.A. (2014). Monitoring synaptic and neuronal activity in 3D with synthetic and genetic indicators using a compact acousto-optic lens two-photon microscope. *J. Neurosci. Methods* *222*, 69–81.
- Garwicz, M., Jörntell, H., und Ekerot, C.F. (1998). Cutaneous receptive fields and topography of mossy fibres and climbing fibres projecting to cat cerebellar C3 zone. *J. Physiol.* *512*, 277–293.

- Geiger, J.R.P., und Jonas, P. (2000). Dynamic control of presynaptic  $\text{Ca}^{2+}$  inflow by fast-inactivating  $\text{K}^+$  channels in hippocampal mossy fiber boutons. *Neuron* 28, 927–939.
- Hallermann, S., Fejtova, A., Schmidt, H., Weyhersmüller, A., Silver, R.A., Gundelfinger, E.D., und Eilers, J. (2010). Bassoon speeds vesicle reloading at a central excitatory synapse. *Neuron* 68, 710–723.
- Hallermann, S., und Silver, R.A. (2013). Sustaining rapid vesicular release at active zones: potential roles for vesicle tethering. *Trends Neurosci.* 36, 185–194.
- Han, Y.Y., Babai, N., Kaeser, P., Sudhof, T.C., und Schneggenburger, R. (2015). RIM1 and RIM2 redundantly determine  $\text{Ca}^{2+}$  channel density and readily releasable pool size at a large hindbrain synapse. *J. Neurophysiol.* 113, 255–263.
- Harris, K.D. (2005). Neural signatures of cell assembly organization. *Nat. Rev. Neurosci.* 6, 399–407.
- Helmchen, F., Borst, J.G., und Sakmann, B. (1997). Calcium dynamics associated with a single action potential in a CNS presynaptic terminal. *Biophys. J.* 72, 1458–1471.
- Heuser, J.E., und Reese, T.S. (1973). Evidence for recycling of synaptic vesicle membrane during transmitter release at the frog neuromuscular junction. *J. Cell Biol.* 57, 315–344.
- Hoffpauir, B.K., Grimes, J.L., Mathers, P.H., und Spirou, G.A. (2006). Synaptogenesis of the calyx of Held: rapid onset of function and one-to-one morphological innervation. *J. Neurosci.* 26, 5511–5523.
- Hosoi, N., Sakaba, T., und Neher, E. (2007). Quantitative analysis of calcium-dependent vesicle recruitment and its functional role at the calyx of Held synapse. *J. Neurosci.* 27, 14286–14298.
- Hua, Y., Sinha, R., Thiel, C.S., Schmidt, R., Huve, J., Martens, H., Hell, S.W., Egner, A., und Klingauf, J. (2011). A readily retrievable pool of synaptic vesicles. *Nat. Neurosci.* 14, 833–839.
- Jakab, R.L., und Hátori, J. (1988). Quantitative morphology and synaptology of cerebellar glomeruli in the rat. *Anat. Embryol.* 179, 81–88.
- Jörntell, H., und Ekerot, C.F. (2006). Properties of somatosensory synaptic integration in cerebellar granule cells in vivo. *J. Neurosci.* 26, 11786–11797.
- Kalinovsky, A., Boukhtouche, F., Blazeski, R., Bornmann, C., Suzuki, N., Mason, C.A., und Scheiffele, P. (2011). Development of axon-target specificity of ponto-cerebellar afferents. *PLoS Biol.* 9, e1001013.
- Katona, G., Szalay, G., Maák, P., Kaszás, A., Veress, M., Hillier, D., Chiovini, B., Vizi, E.S., Roska, B., und Rózsa, B. (2012). Fast two-photon in vivo imaging with three-dimensional random-access scanning in large tissue volumes. *Nat. Methods* 9, 201–208.

- Kennedy, A., Wayne, G., Kaifosh, P., Alvina, K., Abbott, L.F., und Sawtell, N.B. (2014). A temporal basis for predicting the sensory consequences of motor commands in an electric fish. *Nat. Neurosci.* *17*, 416–422.
- Kim, H.W., Kim, N., Kim, K.W., und Rhyu, I.J. (2013). Three-dimensional imaging of cerebellar mossy fiber rosettes by ion-abrasion scanning electron microscopy. *Microsc. Microanal.* *19 Suppl 5*, 172–177.
- Kononenko, N.L., und Haucke, V. (2015). Molecular mechanisms of presynaptic membrane retrieval and synaptic vesicle reformation. *Neuron* *85*, 484–496.
- Kononenko, N.L., Puchkov, D., Classen, G.A., Walter, A.M., Pechstein, A., Sawade, L., Kaempf, N., Trimbuch, T., Lorenz, D., Rosenmund, C., *et al.* (2014). Clathrin/AP-2 mediate synaptic vesicle reformation from endosome-like vacuoles but are not essential for membrane retrieval at central synapses. *Neuron* *82*, 981–988.
- Kumar, A., Rotter, S., und Aertsen, A. (2010). Spiking activity propagation in neuronal networks: reconciling different perspectives on neural coding. *Nat. Rev. Neurosci.* *11*, 615–627.
- Kushmerick, C., Renden, R., und von Gersdorff, H. (2006). Physiological temperatures reduce the rate of vesicle pool depletion and short-term depression via an acceleration of vesicle recruitment. *J. Neurosci.* *26*, 1366–1377.
- Leão, R.M., Kushmerick, C., Pinaud, R., Renden, R., Li, G.L., Taschenberger, H., Spirou, G., Levinson, S.R., und von Gersdorff, H. (2005). Presynaptic Na<sup>+</sup> channels: locus, development, and recovery from inactivation at a high-fidelity synapse. *J. Neurosci.* *25*, 3724–3738.
- Livet, J., Weissman, T.A., Kang, H., Draft, R.W., Lu, J., Bennis, R.A., Sanes, J.R., und Lichtman, J.W. (2007). Transgenic strategies for combinatorial expression of fluorescent proteins in the nervous system. *Nature* *450*, 56–62.
- London, M., Roth, A., Beeren, L., Häusser, M., und Latham, P.E. (2010). Sensitivity to perturbations in vivo implies high noise and suggests rate coding in cortex. *Nature* *466*, 123–127.
- Lou, X., Paradise, S., Ferguson, S.M., und De Camilli, P. (2008). Selective saturation of slow endocytosis at a giant glutamatergic central synapse lacking dynamin 1. *Proc. Natl. Acad. Sci. USA* *105*, 17555–17560.
- Marr, D. (1969). A theory of cerebellar cortex. *J. Physiol.* *202*, 437–470.
- Müller, M., Felmy, F., Schwaller, B., und Schneggenburger, R. (2007). Parvalbumin is a mobile presynaptic Ca<sup>2+</sup> buffer in the calyx of held that accelerates the decay of Ca<sup>2+</sup> and short-term facilitation. *J. Neurosci.* *27*, 2261–2271.
- Nakamura, Y., Harada, H., Kamasawa, N., Matsui, K., Rothman, J.S., Shigemoto, R., Silver, R.A., DiGregorio, D.A., und Takahashi, T. (2015). Nanoscale Distribution of Presynaptic Ca<sup>2+</sup> Channels and Its Impact on Vesicular Release during Development. *Neuron* *85*, 145–158.

- Nanguneri, S., Flottmann, B., Horstmann, H., Heilemann, M., und Kuner, T. (2012). Three-dimensional, tomographic super-resolution fluorescence imaging of serially sectioned thick samples. *PloS one* 7, e38098.
- Neher, E., und Sakaba, T. (2008). Multiple roles of calcium ions in the regulation of neurotransmitter release. *Neuron* 59, 861–872.
- Powell, K., Mathy, A., Duguid, I., und Häusser, M. (2015). Synaptic representation of locomotion in single cerebellar granule cells. *Elife* 4, e07290.
- Rancz, E.A., Ishikawa, T., Duguid, I., Chadderton, P., Mahon, S., und Häusser, M. (2007). High-fidelity transmission of sensory information by single cerebellar mossy fibre boutons. *Nature* 450, 1245–1248.
- Renden, R., und von Gersdorff, H. (2007). Synaptic vesicle endocytosis at a CNS nerve terminal: faster kinetics at physiological temperatures and increased endocytotic capacity during maturation. *J. Neurophysiol.* 98, 3349–3359.
- Rieke, F., Warland, D., de Ruyter van Steveninck, R., und Bialek, W. (1997). *Spikes: Exploring the Neural Code* (Cambridge MA: The MIT Press).
- Ritzau-Jost, A., Delvendahl, I., Rings, A., Byczkiewicz, N., Harada, H., Shigemoto, R., Hirrlinger, J., Eilers, J., und Hallermann, S. (2014). Ultrafast action potentials mediate kilohertz signaling at a central synapse. *Neuron* 84, 152–163.
- Rollenhagen, A., Satzler, K., Rodriguez, E.P., Jonas, P., Frotscher, M., und Lübke, J.H. (2007). Structural determinants of transmission at large hippocampal mossy fiber synapses. *J. Neurosci.* 27, 10434–10444.
- Ryan, T.A., Smith, S.J., und Reuter, H. (1996). The timing of synaptic vesicle endocytosis. *Proc. Natl. Acad. Sci. USA* 93, 5567–5571.
- Sabatini, B.L., und Regehr, W.G. (1996). Timing of neurotransmission at fast synapses in the mammalian brain. *Nature* 384, 170–172.
- Sargent, P.B., Saviane, C., Nielsen, T.A., DiGregorio, D.A., und Silver, R.A. (2005). Rapid vesicular release, quantal variability, and spillover contribute to the precision and reliability of transmission at a glomerular synapse. *J. Neurosci.* 25, 8173–8187.
- Sätzler, K., Söhl, L.F., Bollmann, J.H., Borst, J.G., Frotscher, M., Sakmann, B., und Lübke, J.H. (2002). Three-dimensional reconstruction of a calyx of Held and its postsynaptic principal neuron in the medial nucleus of the trapezoid body. *J. Neurosci.* 22, 10567–10579.
- Saviane, C., und Silver, R.A. (2006). Fast vesicle reloading and a large pool sustain high bandwidth transmission at a central synapse. *Nature* 439, 983–987.
- Scheuss, V., Schneggenburger, R., und Neher, E. (2002). Separation of presynaptic and postsynaptic contributions to depression by covariance analysis of successive EPSCs at the calyx of Held synapse. *J. Neurosci.* 22, 728–739.
- Schmidt-Hieber, C., und Häusser, M. (2013). Cellular mechanisms of spatial navigation in the medial entorhinal cortex. *Nat. Neurosci.* 16, 325–331.

- Schneggenburger, R., und Neher, E. (2000). Intracellular calcium dependence of transmitter release rates at a fast central synapse. *Nature* 406, 889–893.
- Schneggenburger, R., und Rosenmund, C. (2015). Molecular mechanisms governing  $\text{Ca}^{2+}$  regulation of evoked and spontaneous release. *Nat. Neurosci.* 18, 935–941.
- Schwaller, B. (2010). Cytosolic  $\text{Ca}^{2+}$  buffers. *Cold Spring Harb. Perspect. Biol.* 2, a004051.
- Silver, R.A., Traynelis, S.F., und Cull-Candy, S.G. (1992). Rapid-time-course miniature and evoked excitatory currents at cerebellar synapses in situ. *Nature* 355, 163–166.
- Südhof, T.C. (2004). The synaptic vesicle cycle. *Annu. Rev. Neurosci.* 27, 509–547.
- Taschenberger, H., Leão, R.M., Rowland, K.C., Spirou, G.A., und von Gersdorff, H. (2002). Optimizing synaptic architecture and efficiency for high-frequency transmission. *Neuron* 36, 1127–1143.
- Taschenberger, H., Scheuss, V., und Neher, E. (2005). Release kinetics, quantal parameters and their modulation during short-term depression at a developing synapse in the rat CNS. *J. Physiol.* 568, 513–537.
- Taschenberger, H., und von Gersdorff, H. (2000). Fine-tuning an auditory synapse for speed and fidelity: developmental changes in presynaptic waveform, EPSC kinetics, and synaptic plasticity. *J. Neurosci.* 20, 9162–9173.
- Tchumatchenko, T., Malyshev, A., Wolf, F., und Volgushev, M. (2011). Ultrafast population encoding by cortical neurons. *J. Neurosci.* 31, 12171–12179.
- Valera, A.M., Doussau, F., Poulain, B., Barbour, B., und Isope, P. (2012). Adaptation of granule cell to Purkinje cell synapses to high-frequency transmission. *J. Neurosci.* 32, 3267–3280.
- van Kan, P.L., Gibson, A.R., und Houk, J.C. (1993). Movement-related inputs to intermediate cerebellum of the monkey. *J. Neurophysiol.* 69, 74–94.
- von Gersdorff, H., und Matthews, G. (1994). Dynamics of synaptic vesicle fusion and membrane retrieval in synaptic terminals. *Nature* 367, 735–739.
- Wagner, H., Brill, S., Kempter, R., und Carr, C.E. (2005). Microsecond precision of phase delay in the auditory system of the barn owl. *J. Neurophysiol.* 94, 1655–1658.
- Wang, L.Y., Neher, E., und Taschenberger, H. (2008). Synaptic vesicles in mature calyx of Held synapses sense higher nanodomain calcium concentrations during action potential-evoked glutamate release. *J. Neurosci.* 28, 14450–14458.
- Watanabe, S., Rost, B.R., Camacho-Pérez, M., Davis, M.W., Söhl-Kielczynski, B., Rosenmund, C., und Jorgensen, E.M. (2013). Ultrafast endocytosis at mouse hippocampal synapses. *Nature* 504, 242–247.
- Williams, R.W., und Herrup, K. (1988). The control of neuron number. *Annu. Rev. Neurosci.* 11, 423–453.



- Wolfe, J., Houweling, A.R., und Brecht, M. (2010). Sparse and powerful cortical spikes. *Curr. Opin. Neurobiol.* 20, 306–312.
- Wu, L.G., Hamid, E., Shin, W., und Chiang, H.C. (2014). Exocytosis and endocytosis: modes, functions, and coupling mechanisms. *Annu. Rev. Physiol.* 76, 301–331.
- Xu-Friedman, M.A., und Regehr, W.G. (2003). Ultrastructural contributions to desensitization at cerebellar mossy fiber to granule cell synapses. *J. Neurosci.* 23, 2182–2192.

## 6 Erklärung

Unter Anerkennung der für die Medizinische Fakultät der Universität Leipzig geltenden Habilitationsordnung vom 16.01.2012 wird folgende Erklärungen abgegeben:

Diese Habilitationsschrift wurde in dieser oder ähnlicher Form an keiner anderen Stelle zum Zweck eines Graduierungsverfahrens vorgelegt.

Diese Arbeit wurde von mir selbständig verfasst, es wurden keine anderen als die angegebenen Quellen und Hilfsmittel verwendet und wörtlich oder inhaltlich übernommene Stellen wurden als solche kenntlich gemacht.

Die in der Habilitationsschrift enthaltenen Veröffentlichungen, deren Erstautor oder gleichberechtigter Erstautor ich bin, wurden von mir zu einem entscheidenden Teil geschrieben, geplant sowie experimentell durchgeführt.

Leipzig, den 08.07.2016

---

Dr. med. Igor Delvendahl

## **7 Lebenslauf**

## Schriftenverzeichnis

### 1. Originalarbeiten

- Delvendahl, I., Vyleta, N.P., von Gersdorff, H., Hallermann, S. (2016). Fast, temperature-sensitive and clathrin-independent endocytosis at central synapses. **Neuron** 90, 492–498.
- Delvendahl, I., Straub, I., Hallermann, S. (2015). Dendritic patch-clamp recordings from cerebellar granule cells demonstrate electrotonic compactness. **Front. Cell. Neurosci.** 9, 93.
- Delvendahl, I., Jablonski, L., Baade, C., Matveev, V., Neher, E., Hallermann, S. (2015). Reduced endogenous Ca<sup>2+</sup> buffering speeds active zone Ca<sup>2+</sup> signaling. **Proc. Natl. Acad. Sci. USA** 112, E3075–3084.
- Ritzau-Jost, A. \*, Delvendahl, I.\*, Rings, A.\*, Byczkowicz, N., Harada, H., Shigemoto, R., Hirrlinger, J., Eilers, J., Hallermann, S. (2014). Ultrafast action potentials mediate kilohertz signaling at a central synapse. **Neuron** 84, 152–163.
- Delvendahl, I., Lindemann, H., Jung, N.H., Pechmann, A., Siebner, H.R., Mall, V. (2014). Influence of waveform and current direction on short-interval intracortical facilitation: a paired-pulse TMS study. **Brain Stimul.** 7, 49–58.
- Delvendahl, I., Gattinger, N., Berger, T., Gleich, B., Siebner, H.R., Mall, V. (2014). The role of pulse shape in motor cortex transcranial magnetic stimulation using full-sine stimuli. **PLoS one** 9, e115247.
- Mainberger, F., Zenker, M., Jung, N.H., Delvendahl, I., Brandt, A., Freudenberg, L., Heinen, F., Mall, V. (2013). Impaired motor cortex plasticity in patients with Noonan syndrome. **Clin. Neurophysiol.** 124, 2439–2444.
- Jung, N.H., Janzarik, W.G., Delvendahl, I., Münchau, A., Biscaldi, M., Mainberger, F., Baumer, T., Rauh, R., Mall, V. (2013). Impaired induction of long-term potentiation-like plasticity in patients with high-functioning autism and Asperger syndrome. **Dev. Med. Child Neurol.** 55, 83–89.
- Juenger, H., Kuhnke, N., Braun, C., Ummenhofer, F., Wilke, M., Walther, M., Koerte, I., Delvendahl, I., Jung, N.H., Berweck, S., Staudt, M., Mall, V. (2013). Two types of exercise-induced neuroplasticity in congenital hemiparesis: a transcranial magnetic stimulation, functional MRI, and magnetoencephalography study. **Dev. Med. Child Neurol.** 55, 941–951.
- Delvendahl, I., Lindemann, H., Heidegger, T., Normann, C., Ziemann, U., Mall, V. (2013). Effects of lamotrigine on human motor cortex plasticity. **Clin. Neurophysiol.** 124, 148–153.

---

\* geteilte Erstautorenschaft

- Pechmann, A., Delvendahl, I., Bergmann, T.O., Ritter, C., Hartwigsen, G., Gleich, B., Gattinger, N., Mall, V., Siebner, H.R. (2012). The number of full-sine cycles per pulse influences the efficacy of multicycle transcranial magnetic stimulation. **Brain Stimul.** 5, 148–154.
- Jung, N.H., Delvendahl, I., Pechmann, A., Gleich, B., Gattinger, N., Siebner, H.R., Mall, V. (2012). Transcranial magnetic stimulation with a half-sine wave pulse elicits direction-specific effects in human motor cortex. **BMC Neurosci.** 13, 139.
- Delvendahl, I., Jung, N.H., Kuhnke, N.G., Ziemann, U., Mall, V. (2012). Plasticity of motor threshold and motor-evoked potential amplitude--a model of intrinsic and synaptic plasticity in human motor cortex? **Brain Stimul.** 5, 586–593.
- Delvendahl, I., Kuhnke, N.G., Jung, N.H., Mainberger, F., Cronjaeger, M., Unterrainer, J., Hauschke, D., Mall, V. (2011). The time course of motor cortex plasticity after spaced motor practice. **Brain Stimul.** 4, 156–164.
- Jung, N.H., Delvendahl, I., Kuhnke, N.G., Hauschke, D., Stolle, S., Mall, V. (2010). Navigated transcranial magnetic stimulation does not decrease the variability of motor-evoked potentials. **Brain Stimul.** 3, 87–94.
- Delvendahl, I., Jung, N.H., Mainberger, F., Kuhnke, N.G., Cronjaeger, M., Mall, V. (2010). Occlusion of bidirectional plasticity by preceding low-frequency stimulation in the human motor cortex. **Clin. Neurophysiol.** 121, 594–602.
- Walther, M., Kuhnke, N., Schessl, J., Delvendahl, I., Jung, N., Kreml, D., Ziemann, U., Mall, V. (2008). Deafferentation of neighbouring motor cortex areas does not further enhance saturated practice-dependent plasticity in healthy adults. **Clin. Neurophysiol.** 119, 886–891.

## 2. Übersichtsartikel

- Delvendahl, I., Weyhersmüller, A., Ritzau-Jost, A., Hallermann, S. (2013). Hippocampal and cerebellar mossy fibre boutons - same name, different function. **J. Physiol.** 591, 3179–3188.

## 3. Vorträge bei internationalen Kongressen

- Delvendahl, I., Jablonski, L., Hallermann, S. Presynaptic calcium dynamics at cerebellar mossy fibre boutons. **Society for Neuroscience 2013.** San Diego, CA, USA. Presentation Number: 304.05.



